2019-09-20

Polyaniline-coated Nanoporous Carbon Scaffold for Energy Storage and Water Deionization Applications

Ai, Chengying

UNIVERSITY OF CALGARY

Polyaniline-coated Nanoporous Carbon Scaffold for Energy Storage and Water Deionization

Applications

by

Chengying Ai

A THESIS

SUBMITTED TO THE FACULTY OF GRADUATE STUDIES

IN PARTIAL FULFILMENT OF THE REQUIREMENTS FOR THE

DEGREE OF MASTER OF SCIENCE

GRADUATE PROGRAM IN CHEMICAL ENGINEERING

CALGARY, ALBERTA

SEPTEMBER, 2019

Abstract

The world's rapidly growing population urgently calls for more clean water. However, current water treatment technologies, e.g., reverse osmosis and distillation, are very energy demanding. Capacitive deionization (CDI) has emerged as a promising new technology for the production of clean water from brackish or even seawater at a high efficiency and at low cost, also showing promise in storing energy while simultaneously achieving desalination.

In this work, a novel nanoporous carbon scaffold (NCS), a binder-free, free-standing, and 100% carbon film with a highly tunable nanoporous structure, has shown excellent promise as a CDI electrode. However, its surface area of 200-400 m^2/g for the 50 and 85 nm diameter pore-sized NCS materials, limits the obtainable double layer capacitance. To further increase the electrochemical capacitance of the NCS material, polyaniline (PANi), a conducting polymer with a very high electrochemical capacitance (~750 F/g), was deposited on the NCS using cyclic voltammetry (CV), resulting in a PANi/NCS composite. A range of conformal PANi layers of controllable thicknesses were obtained, without blocking the pores of the NCS, as observed by scanning electron microscopy (SEM). The conformal PANi coating is uniform throughout the thickness of the NCS, as seen from SEM and energy-dispersive X-ray spectroscopy element mapping.

Both CV and galvanostatic charge/discharge (GCD) methods were used to demonstrate the capacitive behavior of the PANi/NCS composite, with the capacitance increasing by 5 to 20 times of that obtained from the original NCS, thus possessing an excellent energy and power density. The PANi-coated NCS also demonstrates good cyclic stability, retaining ca. 85% of its original capacitance after 1000 GCD cycles. Electrochemical impedance spectroscopy (EIS) confirmed that the time constant of the PANi/NCS composites decreased with an increase in the PANi

thickness, from 3 to 20 nm. A flow-through CDI test was carried out using three different cell configurations, including a symmetric NCS cell, a symmetric PANi/NCS cell and an asymmetric cell containing a PANi/NCS anode and an NCS cathode. When using the asymmetric CDI configuration, the salt adsorption capacity was 2.6 mg/g (0.019 mg/m^2), while the salt adsorption can be completed very rapidly in only 2-10 seconds.

I also extend acknowledgements to John Vandersleen and Dr. Behzad Fuladpanjeh Hojaghan, from the Chemical Engineering Department, for helping me to use the 3D printer, making the cover of the cell used in Chapter 4. Thanks are also due to Ola Jabar, Max Anikovskiy, Linda Tong and George Huang for training me on various instruments, including the thermal gravimetric analyzer, scanning electron microscope, and BET surface area analyzer. Without their training, I would not have been able to conduct all of the characterization described in this thesis.

I would also like to thank my thesis examiners, Drs. Ted Roberts and Anne Benneker, for agreeing to serve on my committee.

My thesis could not have begun without Dr. Xiaoan Li, the co-inventor of the novel nanoporous carbon scaffold that was studied in this work. Xiaoan taught me how to prepare the scaffold when he was a postdoctoral fellow in Viola's group. He is an intelligent person and I am so grateful to him for teaching me and guiding me. Special thanks also to Dr. Robert Mayall, a former student in Viola's group for his encouragement and help on both my research and career development. I would not have tried many things without his suggestions. Thank to Robert also for answering my endless requests for help.

I also want to thank Dr. Scott Paulson, Dr. Erwan Bertin, Marwa Atwa (a PhD student), and Christine Li (a master student) from Viola's group, for their technical help in my lab work and suggestions on how to run my experiments. I really enjoyed talking and discussing many topics with them.

I would also like to thank the current members from both Viola's group and Sathish's group that have encouraged and inspired me throughout my program, Dr. Harris Ansari, Annie Hoang, Samantha Luong, Dr. Maggie Young, Jason Young, Dr. Linda Tong, Dr. Alex Hyla, Sharath

Shetty, Anindya Mitra, Atefeh Tarokh, Amir Alihosseinzadeh and Derrick Bakuska. Many thanks to them for their help, support and for all the happy times we spent together.

I must also acknowledge the financial assistance provided from the University of Calgary for this research program. Extended thanks to the Chemistry and the Chemical Engineering support staff for their support of graduate students.

I would especially like to thank my father, Rong Ai, for his unconditional support and for being the best dad ever. Although he does not have any idea about my thesis work and my career path, he blindly supports me. I also extended my thanks to my aunts, uncle-in-laws and my grandparents for their kind support during my last 25 years, to my uncle, Xuegong Ai, for his support and guidance, my cousin, Alvin Wang, for being a hardworking role model and other family members for their support and help.

I am also very thankful to my friends, Yuemeng Zhang, Qing Huang and Qinwan Chong, and all the other people who have encouraged, supported and inspired me throughout my Master's studies. Yuemeng especially has always been there, listening to me and cheering me up, even though we are 5,400 miles away (thanks to the internet). Her humor and incredible understanding have helped me to get through many difficult times.

Dedication

To

My father who is always supporting me.

Table of Contents

List of Tables

List of Figures and Illustrations

xiv

List of Symbols

Symbol	Unit	Definition
ϕ		Potential of the aqueous solution within the pores of the electrode
$\Delta\phi_{St}$		Potential of the Stern layer
$\Delta\phi_d$		Potential of the diffuse layer
ϕ_1		Potential of the electrode
C_{EDL}		Capacitance of the double layer
C_{Stern}		Capacitance of the Stern layer
$C_{Diffuse}$		Capacitance of the diffuse layer
Λ		Charge efficiency of CDI cell, dimensionless
Γ_{salt}	mol, mol/area, or mol/g	The amount of salt removed
Σ	mol, mol/area, or mol/g	Total charge transfer
Γ	mg/g	Salt adsorption capacity
M	g/mol	Molecular weight
k	$\mu S \cdot cm^{-1} \cdot mM^{-1}$	Calibration number
m	g	Weight of CDI electrodes
Φ	L/min	Flow rate
σ_0	$\mu S \cdot cm^{-1}$	Initial conductivity of the solution
σ	$\mu S \cdot cm^{-1}$	Conductivity
t	min	Time
V	L	Volume
C_m, C_{sp}	F/g	Gravimetric/specific capacitance
C_a	F/cm^2	Areal capacitance
C'	F/g	Real part of the complex capacitance
C''	F/g	Imaginary part of the complex capacitance
ω		Angular frequency
π		A mathematical constant, 3.14
f	Hz	Frequency
I	A	Current
v	mV/s, V/s	Scan rate
V, E	V	Potential
A	cm^2	Geometric area of the electrode
C	F/g	Complex capacitance
Z	Ω	Complex impedance
Z'	Ω	Real impedance
Z''	Ω	Imaginary impedance
R_s	Ω	Series resistance
f_m	Hz	Imaginary capacitance peak frequency
τ	s	Time constant
v		Bond stretching
δ		Bond bending

I_{peak}	mA	Peak current
U	Wh/kg	Energy density
P	W/kg	Power density
U_{con}	kWh/m^3	Energy consumption
t_{ad}	min	Salt adsorption time

List of Abbreviations

Abbreviations	Definition
AC	Activated carbon
ACC	Activated carbon cloth
ASAR	Average salt adsorption rate
B	Benzenoid ring
BET	Brunauer-Emmett-Teller
BJH	Barrett-Joyner and Halenda
CC	Constant current charging
CDI	Capacitive deionization
CIC	Colloidal-imprinted carbon
CNT	Carbon nanotube
CV	Cyclic voltammetry
CVC	Constant voltage charging
EB	Emeraldine base
EDL	Electrical double layer
EDX	Energy Dispersive X-ray spectroscopy
EIS	Electrochemical impedance spectroscopy
ES	Emeraldine salt
ESR	Equivalent series resistance
FCDI	Flow-electrode capacitive deionization
FE-SEM	Field Emission Scanning Electron Microscopy
GA	Graphene aerogel
GCD	Galvanostatic charge/discharge
GCS	Gouy-Chapman-Stern
GO	Graphene oxide
HCDI	Hybrid capacitive deionization
iCDI	Inverted capacitive deionization
LDPE	Low density polyethylene
MCDI	Membrane capacitive deionization
MOF	Metal organic framework
MP	Mesophase pitch
MWCNT	Multiwalled carbon nanotube
NCS	Nanoporous carbon scaffold
NF	Nanofiltration
NM	Nanomaterial
NMP	N-methyl-2-pyrrolidinone
o.p.	Out-of-plane
OCP	Open circuit potential
oCVD	Oxidative chemical vapor deposition
OHP	Outer Helmholtz plane
PANi	Polyaniline
PC	Porous carbon
PD	1,3-propanediol

PE	Pernigraniline
Phz	Phenazine-like segment
PPD	N-phenyl-p-phenylene
PVA	Polyvinyl alcohol
PVF	Poly(vinyl alcohol)-formaldehyde
Q	Quinonoid ring
RO	Reverse osmosis
SAC	Salt adsorption capacity
SA-CNT	Self-assembled carbon nanotub
SS	Stainless steel
TDS	Total dissolved solids
TGA	Thermal gravimetric analysis
UF	Ultrafiltration
VACNT	Vertically aligned carbon nanotube

Chapter 1 Introduction

1.1 Background

1.1.1 Current water scarcity and the urgency for clean water

Clean water is critical to both the environment and human health. Currently, over one-third of the global population is facing clean water stress and the number is predicted to climb to two-thirds by 2025 [1]. However, around 80% of wastewater is discharged into the ecosystem without proper treatment, leading to a loss of clean water for nearly 750 million residents [2], [3]. In Alberta alone, millions of litres of contaminated and undrinkable water are created by industrial processes every day. While the world population is increasing by 80 million a year [4], the demand for producing clean water has become more urgent now. Seawater (35,000 – 50,000 ppm TDS) and brackish water (500 – 35,000 ppm TDS) account for more than 97% of total earth's water, and they have become an indispensable and secure water source in areas such as the Middle East and North Africa [5]. However, current desalination technologies consume a large amount of energy and create significant greenhouse gases, and they need pre-treatment to remove solid particulates as well as post-treatment to stabilize the desalted water, which increases the process costs [6]. Many new technologies are developed to produce fresh water from seawater or brackish water at more economic and efficient way.

Herein, with a novel nanoporous carbon scaffold (NCS), saltwater could be treated by ultrafiltration (see Section 1.1.2) and capacitive deionization (introduced in Section 1.1.3) in one step, simplifying the desalination processes and the ability to produce clean water in a single step.

1.1.2 Challenges for current water desalination technologies

Desalination is a process of separating salt species and water to reduce the salinity to a level that meets the requirement for the applications [5]. Current water desalination technologies are mainly divided into two categories: thermal desalination and membrane separation. Thermal method, such as multi-stage flash distillation, is a conventional method for water desalination by boiling the feed water followed by condensing the steam and collecting clean water. However, distillation plants consume large amounts of energy for heating, which can release significant emissions of greenhouse gases if renewable energy sources are not available [7]. Beside thermal methods, membrane separation technologies such as reverse osmosis (RO), ultrafiltration and nanofiltration, have been widely studied and applied in water treatment and desalination. These technologies are defined by the pore sizes of the membrane. For example, RO membranes possess pores with sizes ranging from 0.1 to 2 nm, nanofiltration membranes have pores from 0.5 – 10 nm and ultrafiltration membranes contain pores from 10 – 200 nm. While such membrane technologies require less energy compared to thermal distillation (Section 1.1.3), the membranes undergo rapid fouling, which leads to rapid loss of productivity, requiring additional pre-treatment and extra energy consumption to clean the membrane [8].

Capacitive deionization (CDI) is an emerging desalination technology, which features low energy consumption and economic benefits for treating water that has low or moderate salinity (Table 1.1), as well as environmental-friendliness and easy regeneration [13]. This technology typically utilizes electrostatic force to attract and store charged species (i.e. Na^+, Cl^-) in the electrical double layers (EDLs). During the charging process, either a constant voltage or a constant current is applied to electrodes, which drives the salt ions in the feed water to migrate toward the electrode and accumulate in EDLs (Fig. 1.1). The electrodes are regenerated by

releasing the salt ions to the bulk solution at zero voltage or by reversing the polarity [10]. The storing of charged species in the EDLs is similar to the energy storage process in supercapacitors, which means energy can be stored in the CDI cell during desalination process and released during the salt desorption step [14], [15]. Detailed discussion on the mechanism behind CDI will be discussed in Section 1.2.

Table 1.1 Comparison of different desalination technologies [5], [9]–[12]**.**

	Advantages	Disadvantages
Reverse Osmosis	High removal of TDS	Rapid membrane clogging; High operation pressure (typically 7 - 100 bar)
Multistage Flash Distillation	Relatively low requirement for the feedwater	High operation cost; Corrosion and scaling due to high operating temperatures.
Capacitive deionization	Energy efficient and cost effective for brackish water or low concentrated seawater (< 10 g/L salinity); Energy can be stored in the desalination step.	Faradaic reactions; Limited salt removal capacity for high salinity water.
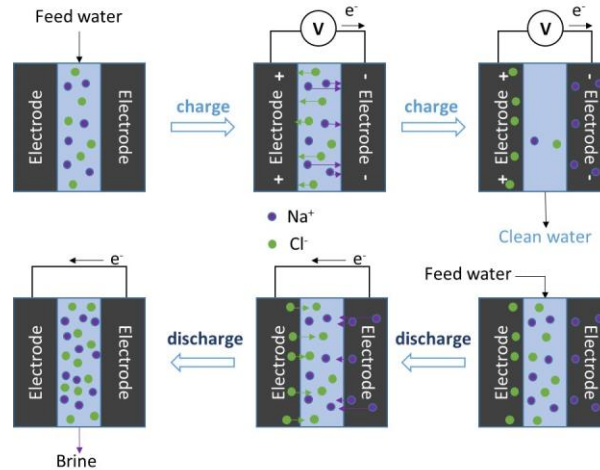
Figure 1.1 Schematic illustration of charge and discharge process in CDI.

1.1.3 Capacitive Deionization (CDI): a novel water desalination technology

CDI technology has been extensively studied since 1970 when the charge/discharge of electrical double layers (EDL) was found to be the mechanism for salt removal in CDI [16], because of its unique advantages:

(a) Compared to desalting by RO or multistage flash distillation, the operation of CDI can be conducted at low pressure and room temperature, saving significantly on operating cost [17]. RO is typically operated between 7 and 100 bar for brackish and seawater, leading to an energy consumption ranging from 2 to 4 kWh/m^3 [1], [18]. Multistage flash distillation, which is usually used for desalting seawater, requires adequate heat to reach a steam temperature in a range of 120 – 135 ˚C which results in 10 – 58 kWh energy consumption for producing one cubic meter of fresh water [7]. A lower energy consumption of 4 kWh/m^3 can be reached by multistage flash distillation if waste heat is used [19]. In contrast, CDI only consume 0.1 – 1 kWh/m^3 for brackish water treatment, but it can consume more energy than RO when treating seawater [5], [20]. It should also be noted that it may not be fair to compare the energy consumption of multistage flash distillation with CDI, as multistage flash distillation is usually used for treating seawater while CDI is more efficient when cleaning brackish water.

(b) CDI has high energy efficiency in dealing with brackish water because the few salt ions are removed from the bulk water.[10] Unlike RO and multistage flash distillation, which are removing the bulk solution (water) from the minor salts, CDI is removing salts from water, which theoretically causes less effort to complete [5], [10].

(c) CDI is one technology which can store energy while removing salts from water. Since CDI is similar to supercapacitors, the desalting process is the same with the charging process of

supercapacitors when energy is stored in the EDLs and the stored energy could power a successive CDI cell [21], or other electric devices.

However, CDI technology is facing two main challenges (Table 1.1) [12]. The first one is the unwanted occurrence of Faradaic reaction, e.g., oxygen evolution, which results in a decrease in the charge efficiency as the charge consumed in these reactions is not stored, but instead, is used to convert chemicals from one form to another. Secondly, the low salt removal capacity of most electrode materials restricts the use of CDI for the treatment of seawater. An additional issue involves the disposal of the brine formed in the salt releasing step, which is a common question related to desalination [5].

The electrode material is one of the key factors that determines the performance of a CDI cell. A good CDI electrode should have a large surface area and accessible pores, high conductivity and stable electrochemical properties. The carbon materials meet most of the above requirements and have been widely studied [22]. The porous carbon materials store salt ions via the formation of electrical double layers (Section 1.2), which is dependent on the accessible surface area and hence have an upper limit of salt adsorption capacity. The salt adsorption performance depends not only on the surface area but also the optimum pore structure [23]. In order to overcome the EDL-imposed capacity limit of carbon materials, an additional mechanism of "Faradaic CDI" can be enabled [24]. For example, if the porous carbon electrode is coated with a redox polymer, an improved salt removal performance and energy storage have been observed as compared to bare carbon (Section 1.2.2) [25], [26].

1.2 Mechanism of capacitive deionization

There are two main salt removal mechanisms in CDI: electrical double layer (EDL) charge and redox reactions. The former is a physical phenomenon where the salt ions migrate toward the charged electrode because of electrostatic force and there is no electrochemical transformation in the electrode materials [27], while the latter involves faradaic reactions where salt ions are intercalated into the electrode materials.

1.2.1 The formation of electrical double layer (EDLs)

For porous carbon electrodes, the dominant salt removal mechanism arises from the presence of an electrical double layer (EDL). An EDL automatically forms when an electrode is immersed into an electrolyte because of the natural charge on the electrode surface, leading to the accumulation of counter-ions on the solution-side of the interface. According to the Gouy-Chapman-Stern (GCS) model, in high ionic strength solutions, the counter ions reside in a compact layer only ca. 0.2 – 0.4 nm from the solid surface (Fig. 1.2a). However, in solutions of medium to low ionic strength, the excess ionic charge reside in the diffuse layer, as shown in Figure 1.2b, due to their thermal motion [13]. These ions are not directly in contact with the electrode surface, and the region between the electrode surface and the centre of the closest counter ion is called the Stern layer, which can contain contact adsorbed ions as well as surface adsorbed solvent molecules. Between the Stern layer and the diffuse layer is the Stern plane, beyond which the concentration of the counter ions decays with increased distance. During CDI operation, an additional (external) potential will be applied on the electrode surface, thus increasing its charge and attracting more ions from the feed water, thus decreasing the salinity of the feed. Depending on the concentration of the feed solution, EDL models could either be as shown in Fig. 1.2a (high salinity, where the diffuse layer is very narrow and can thus be neglected) or Fig. 1.2b (low salinity).
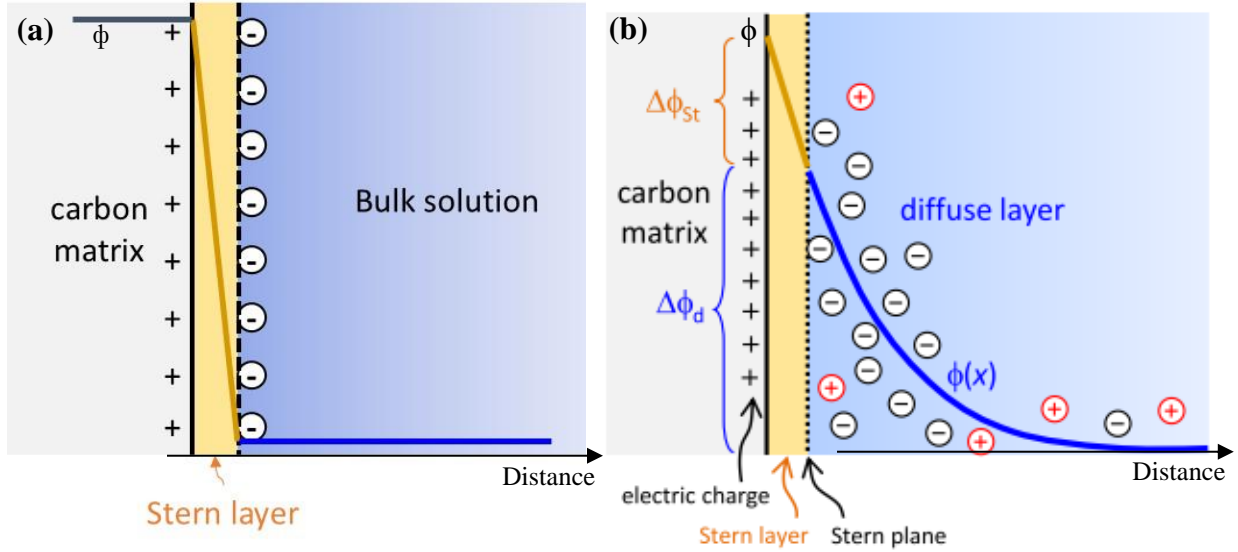
Figure 1.2 The EDL structure based on Gouy-Chapman-Stern model (a) when in sufficiently high electrolyte concentrations, and (b) when the solution is dilute, reported by Porada el al. [13] (Image cited under the Creative Commons Attribution-Non Commercial-No Derivatives License, Appendix A.3)

The voltage across the EDL is a summation of the voltage of the Stern layer ($\Delta\phi_{St}$) and the voltage of the diffuse layer ($\Delta\phi_d$), which is also the potential difference between the electrode (ϕ_1) and that of the aqueous solution within the pores of the electrode (ϕ). The EDL can be modelled using a capacitor model where the capacitance (C_{EDL}) of the interface equals to the sum of two serial capacitors: $1/C_{EDL} = 1/C_{Stern} + 1/C_{Diffuse}$ [22].

The electric charge on the conductive materials is compensated by adsorbing counter ions as well as repelling co-ions. The efficiency of desalination can be measured by calculating the charge efficiency, Λ, according to equation (1.1) [13]:

$$\Lambda = \frac{\Gamma_{salt}}{\Sigma} \qquad (1.1)$$

7

where Γ_{salt} is the amount of salt removed from the feed during the CDI charging step (mol), and Σ is the total charge passed by the electrode (mol).

Taking an open-ended nanopore in the nanoporous carbon scaffold (NCS) as an example, initially, ions accumulate on the surface of the carbon because of the natural formation of the EDL (Fig. 1.3i). As soon as two charges have built up on the electrode (Fig. 1.3ii), one co-ion (ion with the same polarity as the electrode) is repelled from the pore while one counterion (ion with opposite charge to the electrode) is attracted from the bulk solution outside the porous structure into the pore and stored in the EDL. At this point, the net salt removal is zero because, even though one counterion is removed from the bulk, one co-ion compensates and the total concentration of salt in the bulk will not change. Thus $\Lambda = 0$ because $\Gamma_{salt} = 0$. When two charges are applied to the electrode, as shown in Fig. 1.3iii, the same situation happens as in Fig. 1.3ii, where one co-ion is repelled from the pore while one counterion migrated into the pore. At this point, the total salt removal is still zero and so is the charge efficiency. With more charge on the electrode, co-ions will be completely repelled from the pores and any charge further added to the electrode will only be used to attract counterions and store them in the EDLs, resulting in a true salt removal from the bulk aqueous solution and greater than zero charge efficiency (Fig. 1.3iv) [10].
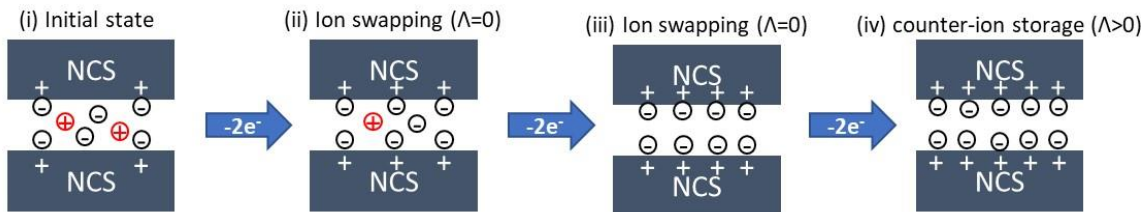
Figure 1.3 The evolution of electric charge building on an open-ended nanopore in NCS electrode. When the charge increases, the status changes from (i) the initial state where no extra charge is applied, to subsequent ion swapping (ii) and (iii), finally reaching counterion storage (iv) [10].

1.2.2 Redox-active capacitive materials

Taking advantage of electrode materials that are redox-active but have capacitive characteristics ('pseudo-capacitance') is another approach that can be used for salt removal when the CDI electrodes are coated with redox-active materials, such as transition metal oxides or conducting polymers, where salt ions are inserted/removed into/from the electrode through redox reactions (Fig. 1.4). The incorporation of redox species into CDI cells, ranging from pure organics to pure metal oxides, has attracted significant research interest, since the redox reactions could increase the salt adsorption capacity and add selective ion removal functionality to the CDI cells (Table 1.2) [28]. There are mainly two redox species of interest in CDI cells, transition metal oxides (i.e. MnO_2, TiO_2) and conducting polymers (i.e. polypyrrole, PEDOT) [23], [26], [29], [30].

For example, MnO_2 goes through the redox reactions below to remove salt cations from the feeding water [31]:

$$MnO_2 + M^+ + e^- \rightarrow ([MnOO]^-M^+)_{\text{(intercalation)}} \qquad (1.2)$$
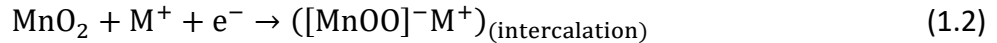
where M^+ is alkaline cations such as Na^+, Li^+ and K^+. In asymmetric cells, which are composed of a porous carbon electrode and a battery electrode (e.g., Na/Mn oxide, Na/Fe pyrophosphate), cations are also intercalated into the battery electrode through redox reactions [32], [33].

For conducting polymers, the salt adsorption capacity is enhanced by inserting/extracting salt ions in the polymer backbones [37]. When a potential is applied on the electrodes (charging process), conducting polymers are oxidized and become polycations (p-doping state), which attracts anions to intercalate into the polymer backbones (eq. 1.3). During the discharge process, conducting polymers are reduced into n-doping state, thereby intercalating with cations as shown in (eq. 1.4):

$$(P)_m + xA^- \rightarrow (P)_m^{x+}(A^-)_x + xe^- \tag{1.3}$$

$$(P)_m + yC^+ + ye^- \rightarrow (P)_m^{y-}(C^+)_y \tag{1.4}$$
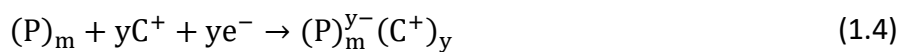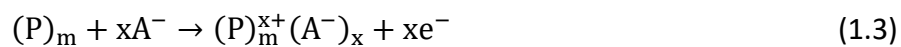
where $(P)_m$ is conducting polymer with conjugated double bonds, m is the polymerization degree,

A^- and C^+ are anions and cations respectively.
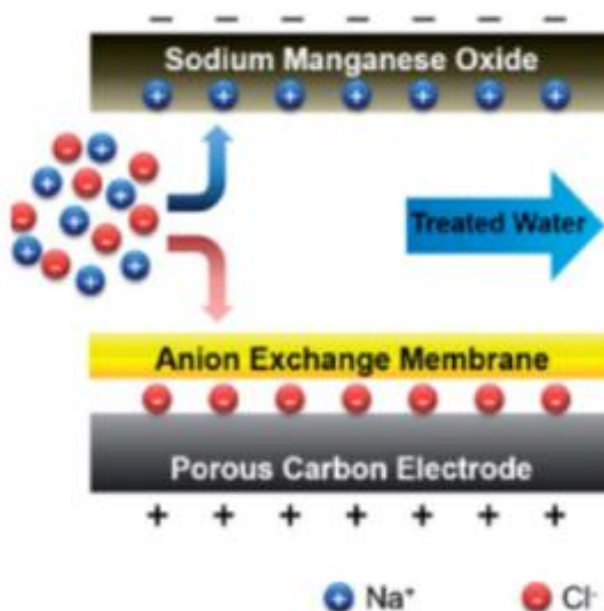
Figure 1.4 Hybrid CDI where the sodium manganese oxide electrode removes sodium ions through intercalation reported by Lee et al. [34] **(Picture cited with permission granted by Rightslink®, Appendix A.4).**

Table 1.2 The increased salt adsorption capacity due to the incorporation of redox species.

Electrode	Removed species	Electrosorption capacity	Ref
poly(vinylferrocene)-MWCNT anode poly- (anthraquinone)-VACNT cathode	carboxylate (acetate, formate, or benzoate)	122−157 mg /g	[25]
MWCNT//VACNT		15 mg/g	
Reduced graphene oxide	NaCl	1.9 – 4.8 mg/g	[26],
Reduced graphene oxide/TiO$_2$		9.1 – 16.4 mg/g	[35]
Reduced graphene oxide -polypyrrole-MnO$_2$	NaCl	18.4 mg/g	[26]
Activated carbon cloth	NaCl	5.9 mg/g	[36]
ZnO coated activated carbon cloth		7.7 mg/g	
Graphene aerogel	NaCl	9.9 – 15.4 mg/g	[29]
Graphene aerogel/TiO$_2$		15.1 – 24.2 mg/g	

1.3 Understanding and measuring CDI performance

1.3.1 Important metrics to evaluate CDI performance

The CDI system is estimated in the literature using salt removal efficiency, salt adsorption capacity, average salt adsorption rate and charge efficiency. Here, in order to better compare the performance with the literature, a standard set of metrics is required.

1.3.1.1 Salt adsorption capacity

Salt adsorption capacity (SAC) is a common metric widely employed in CDI literature, usually reported in mg/g or mmol/g. SAC describes the ability of the electrode materials in removing salt ions from the feed water, which can be calculated by dividing the salt removed by

11

the total weight of electrodes. The salt removed from the feed water can be obtained by integrating the conductivity difference of the influent and effluent water over time, multiplying the flow rate and calibration number (eq. 1.5) [38], or multiplying the total volume of the batch solution (eq. 1.7) [39] depending on the experimental modes (single-pass vs. batch, details in Section 1.3.2.1) which will be introduced in 1.3.2. In a single-pass experiment, the SAC is calculated by:

$$\Gamma = \frac{M}{km} \Phi \int_{t_1}^{t_2} (\sigma(t) - \sigma_0) \mathrm{d}t \tag{1.5}$$

where Γ is the salt adsorption capacity in mg/g, ϕ is the flow rate in L/min, σ_0 is the initial conductivity of the feed water in $\mu S \cdot cm^{-1}$, $\sigma(t)$ is the conductivity of the effluent water during the salt removal process in $\mu S \cdot cm^{-1}$, t_1 and t_2 are the start and end times of salt removal in s, M is the molecular weight of the salt in g/mol, k is calibration number obtained from plotting the conductivity vs. the concentration of model salt solutions in $\mu S \cdot cm^{-1} \cdot mM^{-1}$, m is the weight of electrodes in gram.

In a batch experiment, the SAC can be obtained from eq. 1.6.

$$\Gamma = \frac{M}{k} \frac{(\sigma - \sigma_0)V}{m} \tag{1.6}$$

where σ is the equilibrium conductivity in $\mu S \cdot cm^{-1}$, and V is the total volume of water in the batch (L).

1.3.1.2 Average salt adsorption rate

The average salt adsorption rate is a metric for the CDI cell kinetics. Compared to SAC, which gives information on the electrode materials, the salt adsorption capacity reveals more about the cell properties because the kinetics of the salt removed depends on charging time, feed salinity, cell architecture and electrode materials [10]. The average salt adsorption capacity can be simply

calculated by dividing the salt adsorption capacity with the charging time, and is usually reported in mg·g^{-1}·min^{-1}.

1.3.1.3 Charge efficiency (Λ)

Charge efficiency (Λ), as defined in the CDI literature, is the ratio of the amount of salt that was removed from the feed solution to the electric charge passed in the CDI cell during salt removal (eq. 1.1) [10], [13], [40]. It gives the amount of electric charge that is used for ion removal. If all the electric charge passed is used to adsorb counterions (ions with opposite charge to the electrode), $\Gamma_{salt} = \Sigma$, $\Lambda = 1$. However, during the charging process, the adsorption of counter ions and the desorption of co-ions is happening simultaneously, which leads to the incomplete use of electric charge and decrease of Λ (see Section 1.2: Fig. 1.3) [41]. The charge efficiency for monovalent ions (e.g. Na$^+$, Cl$^-$) is usually higher than that of divalent ions (e.g. Ca^{2+}, Mg^{2+}), because more charge is required to remove the same amount of divalent ions [40].

1.3.2 Operation modes in CDI under laboratory settings

1.3.2.1 Batch mode vs. single-pass mode

For lab scale research on CDI, there are two general operation modes: batch operation (Fig. 1.5a) and single-pass operation (Fig. 1.5b). The former one is more suitable for lab-scale research while the latter one can get more comparable data with real-life CDI application [13]. In batch operation, the water reservoir needs to be small or the salinity cannot be too high, so that the conductivity change can be precisely recorded by a probe. Also, the effluent water is cycled back to the reservoir, and the concentration of influent water is different at the beginning of every cycle. In contrast, the feed water concentration in a single-pass operation is the same in each cycle and the effluent water will be discarded. Under laboratory conditions, the effluent can be discharged

back to the reservoir if the feed reservoir is large enough so that the recycled water will not affect

the concentration of the water in the feed container, ensuring that the conductivity of the influent

remains the same in every cycle.
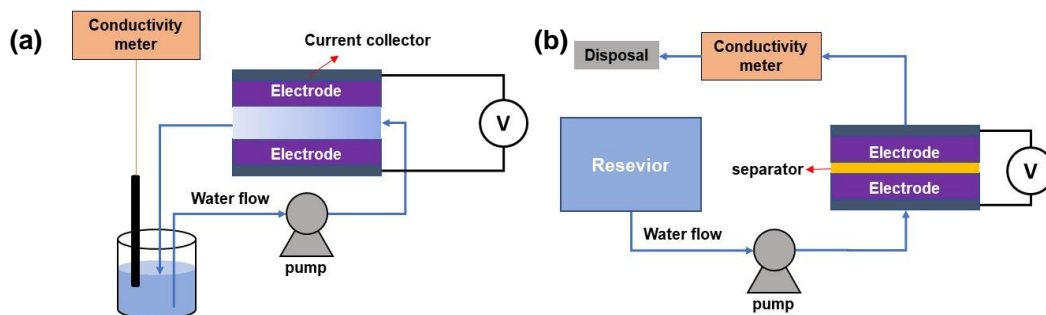
Figure 1.5 (a) Batch mode flow-by CDI operation and (b) Single-pass flow-through CDI operation.

The conductivity probe is usually placed in different locations in these two operations. In

batch experiments, the conductivity of a small water reservoir is measured as shown in Fig. 1.5(a)

while in single-pass experiments, the conductivity probe is placed at the outlet of the cell as shown

in Fig. 1.5(b). The recorded conductivity plots are different in these two modes as well. In batch

experiments, the measured conductivity of the solution in the container continuously decreases

and finally levels off when the maximum salt capacity of the electrodes is reached. In contrast, in

single-pass operation, water with the same concentration is fed into the electrode. At first, the

conductivity of the effluent water decreases because the salt ions are attracted and stored in the

EDL formed on the electrodes, but the conductivity will reach a minimum value where the

maximum salt storage of the electrodes are reached, before growing back to the initial conductivity

of the influent water. This is because the influent water in single-pass experiments always has the

same concentration. As soon as the electrode double layers are saturated with salt ions, the concentration (or conductivity) of the effluent will rise to the value of the initial concentration.

1.3.2.2 Flow-by vs. flow-through cells

While feeding water into a CDI cell, water can flow by in parallel between two electrodes (Fig. 1.6a), or pass through the electrodes (Fig. 1.6b). The former is called flow-by while the latter is called flow-through. Flow-by cells are widely used in the CDI literature and have advantages such as fast flow rate and low pressure drop [13]. Flow-through cells are also reported, which features a fast response. However, these cells need higher operational pressure to achieve the same flow rate as flow-by cell due to pressure drop across the cell.

According to a Remillard et al. study, flow-by cell tends to have higher salt adsorption capacity and charge efficiency compared to flow-through cells while the latter has faster salt adsorption rate [42]. The better performance of flow-by cell might be attributed to its lower contact resistance and less faradaic reactions [43].
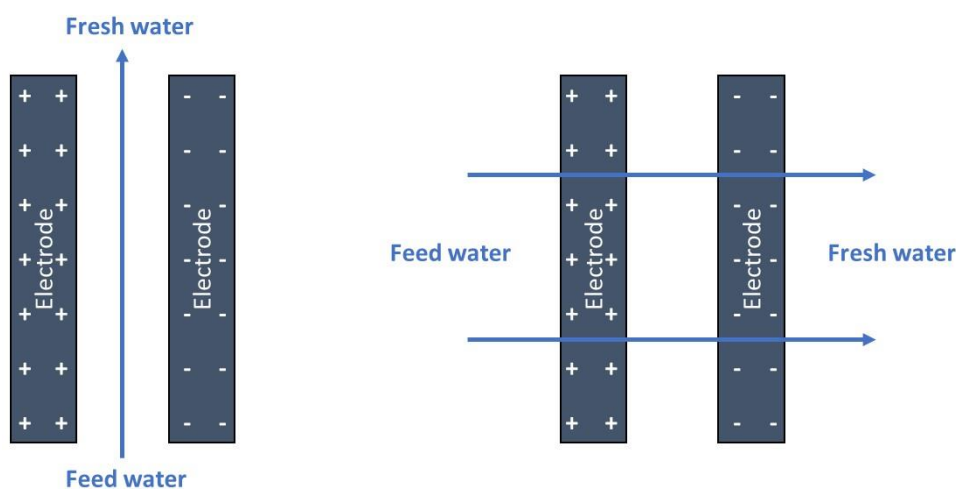
Figure 1.6 Most common CDI cell geometries: (a) Flow-by and (b) flow-through modes.

1.3.2.3 Constant voltage charging (CVC) vs. constant current charging (CC)

In CDI operation, a potential bias between two electrodes is required in order to adsorb ions or intercalate ions. There are two ways to create the potential difference: applying a constant voltage or a constant current.
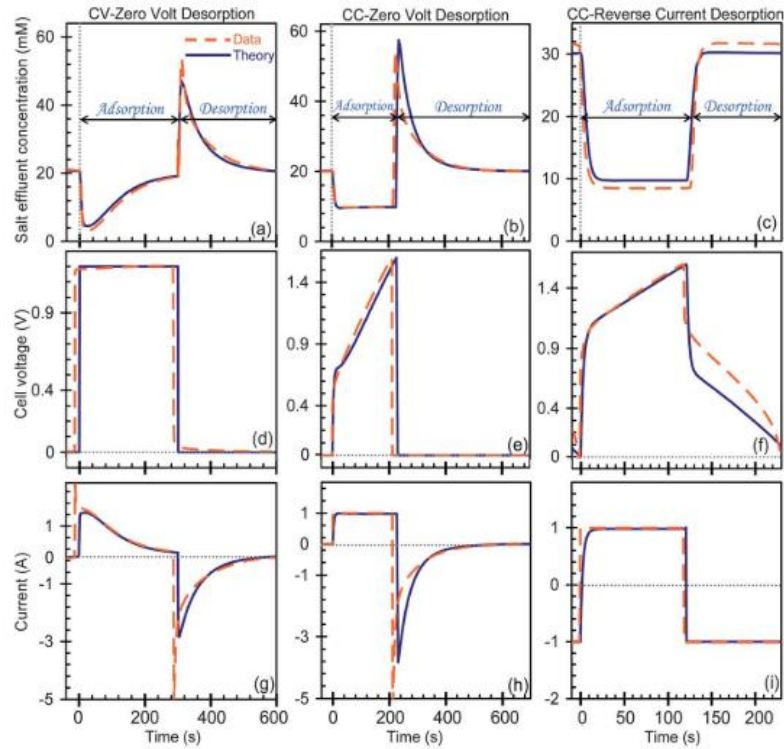
Figure 1.7 Comparison of three different charge/discharge mode in single-pass membrane CDI operation by Zhao et al [14] **(Image cited with permission granted by Rightslink®, Appendix A.5).**

When a constant voltage is applied, initially a large potential difference is created between two electrodes, and the difference gradually decreases when salt ions are adsorbed and stored in the EDLs. Once a maximum SAC is achieved, the concentration of effluent will not change in batch mode or will increase in single-pass mode (Fig. 1.7: left column). CVC is commonly used in CDI research.

16

CC is preferred in real world CDI operation when a constant current is applied to the electrode, because the effluent concentration is stable during CC operation and can be controlled by tuning the applied current (Fig. 1.7: middle and right columns) [14]. Reverse current is able to regenerate the electrodes more thoroughly and improve the salt adsorption capacity and charge efficiency in the following adsorption cycle [13], [14].

1.4 Development of CDI technology

The focus of technological development using a CDI approach can be mainly divided into two areas, the development of cell architecture and the development of electrode materials.

1.4.1 The architecture of CDI cells

The classical CDI cell is composed of the same two electrodes and is called a symmetric CDI cell. Symmetric cell is the most commonly reported CDI system in the literature, especially used for the development and testing of new materials as CDI electrodes [39].

Membrane CDI or MCDI is a type of cell set-up where ion-exchange membranes are included, for example, a cation exchange membrane is placed in front of a cathode where negative charge is applied. The inclusion of an ion-exchange membrane could keep the co-ions, which in this case will only be repelled from the EDLs to the macropores, and for the need to remain neutrality, more counter ions will be attracted and stored in the macropores [44]. This leads to the increase in the charge efficiency and SAC, and also decrease the energy consumption per salt removed [14].

Asymmetric CDI or hybrid CDI (HCDI) uses different electrodes, which can be (a) one EDL electrode, one redox electrode [45]; (b) two chemically-identical electrodes with different chemical charge; (c) two electrodes with different redox groups and different charge [46]. HCDI

17

is claimed to be able to suppress hydrogen evolution and pH excursions, and it also shows promise in selective ion separation [46].

Inverted CDI (iCDI) is also a novel type of CDI, which is able to largely decrease the undesirable Faradaic reactions and increase the long-term stability of CDI operation [38]. In iCDI, salt ions are removed from solution at zero-voltage. The salt ions are then released by applying a charge to the cell to drive the stored ions to leave the electrode.

While all the architectures above are utilizing solid electrodes which has limited SAC, flow-electrode CDI (FCDI), which employs suspended electrodes (suspended activated carbon), can increase the SAC limits. The flow electrode could be continuously fed into the CDI cell and adsorb salts from the feed water without regenerating.[47] FCDI could deal with high salinity such as sea water.

1.4.2 Electrodes development for CDI cells

1.4.2.1 Porous carbon materials

Porous carbon is extensively applied as CDI electrodes because of its wide availability, large specific surface area (400 m^2/g to 2000 m^2/g) [13], [22] and good conductivity. Common porous carbon materials studied as CDI electrodes include activated carbon (AC) [48], carbon aerogel [49], carbon nanotubes (CNTs) [50], graphene [51], and the carbon/carbon composites such as activated carbon/graphene and graphene/CNT [52], [53]. Zhang et al. synthesized N, P, S co-doped hollow carbon polyhedron as CDI electrodes, which has a SAC of 22.19 $mg \cdot g^{-1}$ [54].

These carbon materials are usually in the form of prepared powders and need to be mixed with polymer binders (i.e. polyvinylidene fluoride, polytetrafluoroethylene) while using them as CDI electrodes. This leads to poor wettability, unsuitable pore structures, decreased conductivity

and stability. Because the mechanism for carbon electrodes to desalt is the formation of EDLs during electric charging, the salt adsorption capacity depends largely on the accessible surface areas, which limits the further increase of desalination performance.

1.4.2.2 Carbon composites and battery electrodes

To achieve better salt removal performance, more interests in redox electrodes have emerged. Liu et al. fabricated MnO_2/AC through electrodeposition and the composite electrode has a SAC of 9.3 mg·g^{-1} which is 1.6-fold higher than that of pure activated carbon [55]. Gu et al. prepared a novel graphene-polypyrrole-Mn composites which has a SAC of 18.4 mg g^{-1} and good cyclic stability [26]. Su et al. studied the selective salt separation using poly(vinyl)ferrocene/CNT, cobaltocenium containing polymer/CNT and cobalt-based polymer/CNT electrodes which have shown high current efficiency (up to 96%) towards targeting organic micropollutants [46]. Choi et al. used an asymmetric CDI cell composed of a batter electrode which is a metal organic framework (MOF) electrode named $K_{0.03}Cu[Fe(CN)_6]_{0.65}\cdot0.43H_2O$ and a porous carbon electrode and reached a significantly improved SAC of 23.2 mg g^{-1} and charge efficiency of 75.8% [56].

1.5 Research progress of polyaniline/carbon composites

1.5.1 Properties of polyaniline

Polyaniline (PANi) is an inexpensive, environmentally-friendly and easy-to-synthesize conducting polymer which has attracted a large amount of attention as a supercapacitor electrode material due to its significant theoretical electrical capacitance (~740 F/g) [57]–[62]. In addition, PANi coated porous carbon has increased electrical conductivity, increased surface hydrophilicity, and improved stability under anodic conditions [63].

PANi generally exists as a mixture of three main redox forms: leucoemeraldine (fully reduced), emeraldine salt (half-oxidized), and pernigraniline (fully oxidized) (Scheme 1.1) [64], [65]. These forms can be protonated and, to retain electroneutrality, doped with solution anions. Among those forms, the protonated emeraldine salt is electrically conductive, while either leucoemeraldine or pernigraniline are insulators even after protonation. The high conductivity of the emeraldine salt is explained by the presence of polarons (radical cation units in which π electrons are delocalized) [66].
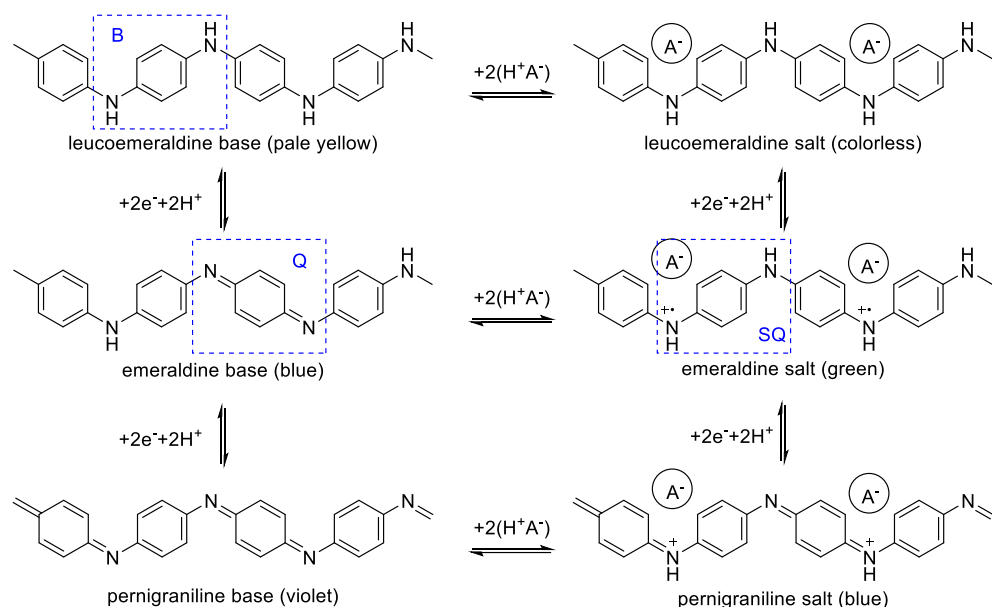
Scheme 1.1 Schemes of the main redox forms of PANi (marked benzenoid (B), quinonoide (Q), and semi-quinonoide (SQ) units). Included are the leucoemeraldine (LE) base, leucoemeraldine (LE) salt, emeraldine base (EB), polaronic form of emeraldine salt (ES), pernigraniline salt, and pernigraniline base.

1.5.2 Methods for polyaniline/carbon composite synthesis

PANi can be deposited on carbon materials through electrochemical polymerization, chemical oxidation, oxidative chemical vapor deposition (oCVD) and direct casting.[67] The first

three methods listed are in-situ polymerization techniques which start from aniline monomers, while the last one involves directly casting prepared polyaniline polymer onto carbon materials.

Electrochemical polymerization includes potentiodynamic and potentiostatic deposition. The potentiodynamic method includes scanning the working electrode (usually the carbon material to be coated) at a constant sweep rate within a potential range. In the potentiostatic method, a constant potential is applied to the working electrode and is held for a certain time (or until a certain charge is reached). Both methods are usually conducted in a typical three-electrode system containing a working electrode, a counter electrode and a reference electrode. Electrochemical methods are an easy-to-operate approach for depositing PANi on carbon materials [68]. Choi and Park studied the effects of polymerization methods on PANi and found that PANi formed from potentiodynamic method was smoother and more compact compared to that grown by a potentiostatic method [69].

Chemical oxidation is another common approach to polymerize aniline monomers on carbon materials. Usually aniline is mixed slowly with carbon and an oxidant such as ammonium persulphate [58]. Chemical oxidation is usually used for powdered carbon and the morphology or thickness of the coated PANi cannot be controlled.

The oCVD method was shown to add an ultrathin PANi coating with a thickness of 1-2 nm inside micro/mesopores by Smolin et al [70]. In this method, aniline monomers and antimony pentachloride vapors are mixed in a vessel containing porous carbon under N_2 atmosphere. Aniline vapor diffuses into the pores and is oxidized there. This method is more complex to conduct and consumes more energy when compared with other three methods.

Direct casting is simply mixing the carbon materials with polyaniline. Wu et al. prepared porous polyaniline/reduced graphene oxide composite through mixing graphene oxide (GO)

aqueous solution with PANi suspension in N-methyl-2-pyrrolidinone (NMP) and then reduce the GO [71]. In this way, PANi molecules with an average 25 nm diameter are distributed on the GO sheets.

1.5.3 Morphology control of polyaniline

Porous structures of electrodes in electric devices including supercapacitors and capacitive deionization electrodes have important influence on the electrochemical performance. Incorporating PANi inside porous carbon materials and maintaining a desirable porous structure at the same time is critical. However, since CDI electrodes usually contains nanopores ($\leq$100 nm), coating PANi inside the pores without destroying the porous structure at a nanoscale is a challenge.

Controlling the morphology of electropolymerized polyaniline has been widely studied [69], [72]–[74]. H.B. Zhang et al. reported that by chronoamperometric deposition, a compact 2-dimensional polyaniline formed on a stainless steel (SS) substrate over a polymerization time between 110 to 250 s, while nanofibrillar PANI layers started to grow after 250 s [72]. Mu et al. studied the effect of scan rate on the morphology of polyaniline on platinum substrate and found that when polymerizing at slow scan rate, the formed polyaniline nanofibers have the largest diameter and the longest length. This is because the already formed nuclei have more time to laterally connect with each other and grow vertically [73]. H. Wang et al. also mentioned the effect of scan rate on the morphology of polyaniline grown, in the presence of carbon black, meant that short nanorods formed at slow scan rate (10 mV/s), while entangled and merged nanofibers were obtained at a higher scan rate (50 mV/s) [75]. Choi and Park have studied the influence of the electrolyte and growth methods on the polyaniline morphology [69]. Their results show that a compact and smooth layer of PANi was obtained on a Au-coated quartz crystal in $HClO_4$ electrolyte while PANi fibers formed in H_2SO_4 and HNO_3 electrolytes. These results, could be

explain by the hydrophobic effects. Also, the electrodynamic method causes less degradation compared to electrostatic methods. H. Dinh studied PANi formed by potentiodynamic method with two different potential window (0-0.95 V vs RHE, 0-1.7 V vs. RHE), and found that more compact and uniform PANi films formed while in a narrow potential window [74].

1.6 Research goals and objectives of thesis

1.6.1 Development of multi-functional CDI

The ultimate goal of the present work is to develop a one-step removal technology for suspended particles and dissolved ions from brackish water. Such a one-step removal of various target contaminants (e.g., suspended particles, dissolved ions and organics) is an important technological direction for achieving a more simplified and efficient treatment of water. For example, G. Ye et al. recently reported a flow-through system combining CDI and photocatalysis, based on electrodes composed of a layer of graphitic carbon nitride, an interlayer of self-assembled carbon nanotubes (SA-CNTs) and a layer of poly(vinyl alcohol)-formaldehyde (PVF) foam, which is able to remove salt and organic contaminants (e.g. methylene blue, tetracycline) in a single step [76].

A Free-standing nanoporous carbon scaffold (NCS), prepared by the colloidal imprinting method, has tunable pores ranging from 5 nm to 100 nm (Fig. 1.8a) and has been proven to be able to perform as filters, removing suspended particles and some bio-contaminants (e.g. bacteria, viruses) from liquid (Fig. 1.8b) [77]. Thanks to the conducting nature of carbon, NCS is also a promising candidate as a CDI electrode. Combining the CDI functionality of the NCS with its nanofiltration/ultrafiltration capability to fulfill a single-step water treatment could provide a promising solution for the world's water problems.
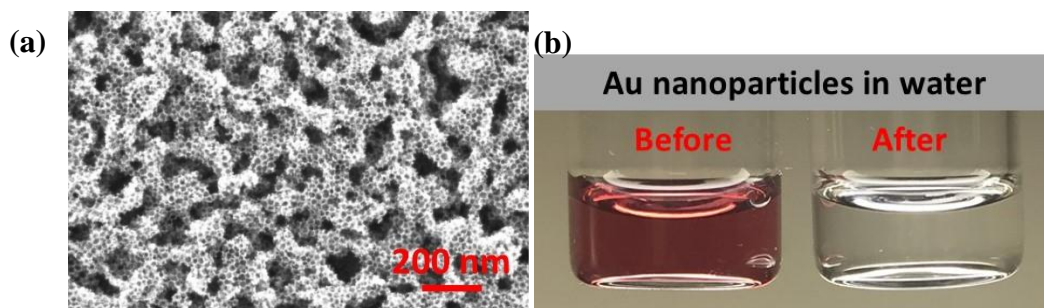
Figure 1.8 (a) The SEM image of NCS-22 (22 nm diameter pores). (b) The filtration of Au nanoparticles using NCS-22 [77]**.**

1.6.2 Research objectives of thesis

To test the CDI performance of a novel nanoporous carbon scaffold (NCS) material and PANi-coated NCS composite for the deionization of brackish water, while also developing a combined CDI and ultrafiltration (UF) system.

I   Conformal coating of polyaniline (PANi) into NCS structure,

    i   Develop a protocol for studying the physical and electrochemical properties of NCS.

    ii   In-situ polymerization of PANi inside NCS through the potentiodynamic approach.

        a   Study the effect of the potential window and scan rate on the morphology of formed PANi in the NCS structure.

    iii   Study the surface and physical properties of PANi-coated NCS and compare with NCS, including surface areas, pore size distribution and thermal stability.

    iv   Study the electrochemical properties of PANi-coated NCS as an electrode and compare with NCS.

II   CDI and UF using NCS and PANi-coated NCS.

i   Study the CDI performance of a NCS and/or PANi-coated NCS based CDI cell with different configurations.

ii   Optimize the operating conditions to achieve the best CDI performance.

iii   Determine if NCS and PANi-coated NCS could serve to simultaneously achieve CDI and UF.

1.7 Thesis organization

The present chapter gives a general introduction on current challenges of water treatment technologies, emerging CDI technologies and development on CDI architecture and electrode materials. Chapter 2 gives detailed information on the experimental methods used in this thesis research, including electrodeposition of polyaniline, Raman microscopy and electrochemical analysis. Chapters 3 and 4 present the results and discussion of this thesis work, written in the format of manuscripts (letters of permission seen in Appendix A.(1,2)).

Chapter 3 focuses on the electrodeposition of a thin PANi layer on a nanoporous carbon scaffold with either a 50 or 85 nm pore size, namely NCS-50 and NCS-85, respectively. In this chapter, the surface properties and electrochemical performance of PANi coated NCS-50 and NCS-85 were studied. The results confirm that a thin and conformal PANi coating was successfully deposited into the NCS structure. The specific capacitance significantly increases after PANi coating and the intrinsic resistance decreases, which holds high promise in applications such as supercapacitors and CDI.

Chapter 4 focuses on the use of NCS-85 and PANi coated NCS-85 as CDI electrodes, and combining CDI with ultrafiltration. In this work, the cyclic stability of NCS-85 and PANi coated NCS-85 was tested, and both materials were tested as CDI electrodes, either in a symmetric set-

up or asymmetric set-up. The results show that PANi coated NCS-85 has excellent electrochemical stability during 1000 charge/discharge cycles in a three-electrode system. The CDI performance of an asymmetric cell composed of a PANi coated NCS-85 anode and an NCS-85 cathode exhibited the best salt removal performance. The combined CDI and ultrafiltration performance was demonstrated by feeding Au-nanoparticle contaminated salt water through an asymmetric cell. The results show a complete removal of Au nanoparticles.

Chapter 5 summarizes this thesis research and provides potential future directions.

Note: In Chapters 3 and 4, I did all of the experimental work except for the elemental analysis, which was done by Jian Li at University of Calgary, and the Raman Spectroscopy, done by Dr. Irina Chernyshova at Colombia University. For both Chapters 3 and 4, I wrote the first draft and constructed all of the figures and tables, and then made the edits recommended by my supervisors and Dr. Erin Gawron.

Chapter 2: Experimental Methodologies

2.1 Material preparation

2.1.1 Preparation of nanoporous carbon scaffold (NCS)

The NCS film was prepared based on the method developed by Li et al [78]. The procedures used to prepare the NCS with an average pore size of 50 or 85 nm were as follows: mesophase pitch (0.6 g, MP, AR Grade, Mitsubishi Chemicals, Japan) and 2.4 g n-butanol were mixed in a 20 mL low density polyethylene (LDPE) bottle and then ball-milled (70 rpm, 2 hours) using 32 g of alumina balls (4 mm in diameter). 9.6 g of 15 wt.% Polyvinyl alcohol (PVA, Alfa Aesar, 86-89% hydrolyzed, low molecular weight) in water was added and the mixture was then ball-milled for another 3 h to produce a homogeneous MP/PVA ink. 9 g of 33.3wt.% SiO_2/water/1,3-propanediol (PD) solution (prepared from NanoSol-5080S, with an average colloid size of 50 nm or 85 nm, stabilized with Na cations) was added to the MP/PVA ink and was then ball-milled for 4 h to obtain the MP/PVA/PD/silica ink (or slurry). The ink was degassed under house vacuum for 30 min to remove any trapped gas bubbles.

The slurry was then cast on a glass substrate using a casting blade with a 0.003 inch (76 µm) gap between the doctor blade and the substrate. After drying, a pristine composite MP/PVA/PD/silica film was obtained. Six such films were then pressed together to form one 6-layer film. The film was placed between two carbon-coated alumina plates. This assembly was inserted into an alumina tubular furnace and carbonized at 900 °C for 2 h in a nitrogen atmosphere, heating at a ramp rate of 0.1-2 °C/min. Prior to reaching 900 °C, the temperature was held at 400 °C for 2 h. After cooling, the carbonized films were soaked in 3 M NaOH at 80 °C for 2 days to remove the silica template. Following this, the films were soaked in dilute HCl for one day to remove extra NaOH. After washing with deionized water several times, the films were air dried at

27

80 °C overnight. The resulting self-supported nanoporous films were stored in conductive containers, e.g., Al foil covered Petri dishes, to avoid electrostatic effects. These nanoporous carbon films were labelled as NCS-50 and NCS-85, with "50" and "85" corresponding to the template silica particle size of 50 nm and 85 nm, respectively. The as-prepared NCS film has a thickness of 60 – 80 µm.
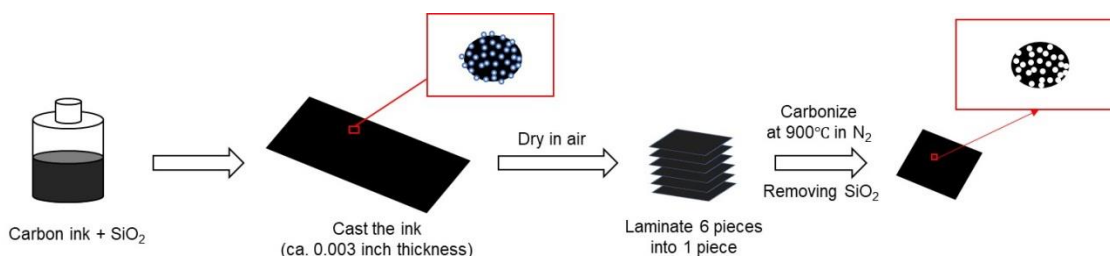
Scheme 2.1 Preparation of free-standing NCS films following the method developed by Li et al.[77]**.**

2.1.2 Electrochemical preparation of Polyaniline-coated NCS

Polyaniline was deposited on the NCS film using the cyclic voltammetry (CV) method [74], [79]. The NCS was used as the working electrode in a three-electrode cell (Fig. 2.1). A piece of NCS (1×1 cm) was sandwiched between a Au-coated glass slide (DRLI) and a perforated glass slide, with the edges sealed by Parafilm M (PM-996, Bemis NA) (Fig. 2.1a). A Pt gauze and an Ag/AgCl electrode (RE-5B, BASi) were used as the counter and reference electrodes, respectively.

An electrolyte containing 0.1 M aniline was prepared by adding 0.28 g aniline ($\geq$ 99.5%, ACS reagent, SIGMA-ALDRICH) to 30 mL 1.0 M H_2SO_4. The NCS-based working electrode was soaked in the as-prepared electrolyte for 30 min with N_2 gas bubbling in the electrolyte. Then the working electrode was scanned between -0.222 to 0.828 V vs. Ag/AgCl at a sweep rate of 5 mV/s. A potentiostat (Solartron Analytical 1480 MultiStat) was used to control the electrochemical polymerization and measurements. The as-prepared PANi-coated NCSs were named as PANi-

X/NCS, where X denotes the number of CV cycles used to deposit the PANi within the NCS nanostructure.
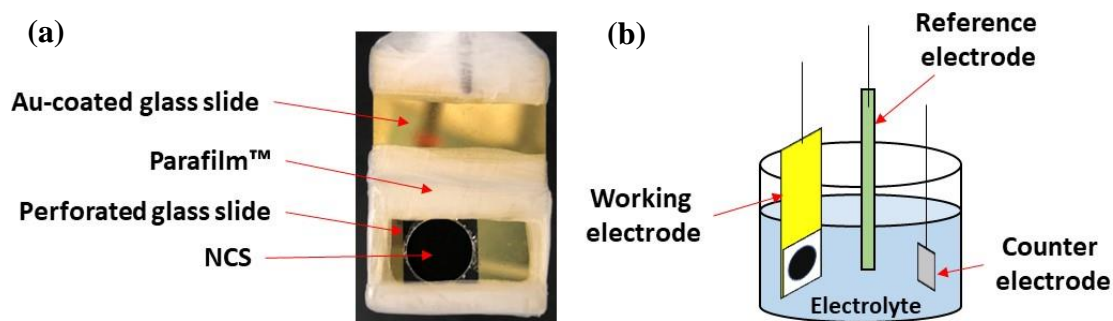
Figure 2.1 (a) Top-view of the working electrode. (b) Schematic of the three-electrode cell used for PANi coating and electrochemical testing.

2.2 Physical and chemical characterization of the NCS and PANi/NCS materials

2.2.1 Scanning electron microscope (SEM) characterization

SEM is a useful tool for the examination of the morphology and topography of material surfaces. Unlike optical microscopy, SEM applies an electron beam to the materials, where the electrons interact with the surface and induce the emission of secondary and back-scattered electrons, producing an image of the surface as well as elemental information.

In this work, all samples were characterized by Field Emission SEM (FE-SEM, Zeiss Sigma VP) at an accelerating voltage of 8 kV. The elemental composition of the samples was determined by Energy dispersive X-ray spectroscopy (Oxford) at an accelerating voltage of 15 kV. A small piece of the samples, typically with a size of 1×1 mm^2, was cut and fixed on top of a carbon tape (Agar Scientific) on an Al SEM stub and a small piece of sample was fixed on the side of the stub for imaging of the cross-section of the sample (Scheme 2.2).
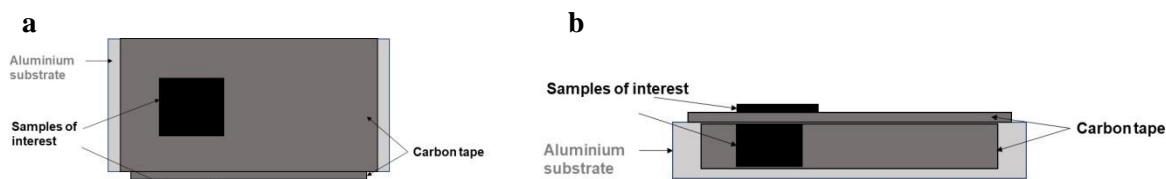
Scheme 2.2 Sample preparation for SEM characterization: (a) top view and (b) side view.

2.2.2 Thermogravimetric analysis

Thermogravimetric analysis (TGA) is a technique where the mass change of a sample is recorded with time at elevated temperature. The TGA result can provide material properties, such as thermal stability, phase changes, or oxidation/decomposition, etc. [80].

The thermal stability of NCS-85 and PANi-6/NCS-85 was determined by a Thermogravimetric Analyzer (TGA/DSC 3+, METTLER TOLEDO) by heating from 50 °C to 1000 °C at a ramp rate of 10 °C in nitrogen. All samples were dried in a vacuum oven at room temperature overnight to remove water before the TGA tests. During the TGA measurements, the samples was held for 15 min at 50° C before heating at 10°C/min to 1000 ° C, all in N_2.

2.2.3 Nitrogen physisorption

Physisorption of gases is an important experimental method that can provide useful information about the material surface area and pore size distribution. In this method, subcritical fluids, which are fluids compressed at their critical temperature (N_2 at 77 K), are fed into the sample tube at different relative pressures, and the amount of fluid adsorbed on the sample surface is recorded [81]. The amount of adsorbed gas is plotted vs. the relative pressure to achieve a physisorption isotherm. Different models can then be applied to the physisorption data to obtain the surface area and pore size distribution, and the most commonly used models used in the literature are the Brunauer-Emmett-Teller (BET) and the Barrett-Joyner-Halenda (BJH) methods [81].

The N$_2$ adsorption/desorption isotherms of NCS-85 and PANi-6/NCS-85 in this thesis work were obtained using a Gemni VII Surface Area Analyzer (Micromeritics) at 77 K. Before the measurements, NCS and PANi/NCS-85 were degassed at 200 ºC and 40 ºC for 4 hours, respectively. The specific surface area and the pore size distribution were calculated using the BET method and BJH method from the Gemni software.

2.2.4 Elemental Analysis

The chemical content (carbon, hydrogen and nitrogen) of NCS and PANi-6/NCS-85 samples was determined by combustion analysis (PerkinElmer 2400, Chemistry Instrumentation Facility, Department of Chemistry, University of Calgary). The samples were ground using a quartz mortar and pestle and then the carbon powder was dried in a vacuum oven at room temperature overnight before combustion analysis.

2.2.5 Raman microscopy

Raman microscopy is a powerful tool in chemical characterization as it can give a structural fingerprint of the tested substance, including the nature of the molecular bonds and the material identification.[82] The Raman spectra of the PANi-6/NCS-85 were determined in situ and in operando using a confocal Raman microscope (LABRAM-ARAMIS, 600 grooves/mm diffraction grating) with a UPlanApo/IR 60X (Olympus) water-immersion objective (0.2 mm working distance). A HeNe (633 nm) laser with a nominal power of 17 mW was used to excite the samples, with and without attenuation. All Raman spectra were acquired for samples immersed in 3 M NaCl.

The *in situ* spectra were collected without applying a potential. Operando spectra were collected in an Ar-saturated 3 M NaCl solution at pH of ca. 7 in an in-house, one-compartment, three-electrode spectroelectrochemical cell (Fig. 2.2a). The working electrode was prepared by sandwiching a PANi/NCS-85 flake (ca. 1×3 mm^2 in size) between the folds of a bent Pt foil (Fig.

2.2b). A Pt-Ir foil was used as the counter electrode and an Ag/AgCl electrode (RE-5B, BASi) was used as the reference electrode.

A Metrohm potentiostat (PGSTAT128N), controlled by NOVA 1.10.4 software, was used in the experiment. The spectroelectrochemical cell was made from high-density polyethylene and was placed under the UPlanApo/IR 60X objective. Each spectrum was collected at a 5 s exposure and 10 accumulations (50 s total) after the cell current had stabilized (after ca. 1-2 min). The spectra were processed and represented using OriginPro software. The processing involved subtraction of the spectrum of the NCS-85 support and background noise from the PANi-6/NCS-85 spectra.
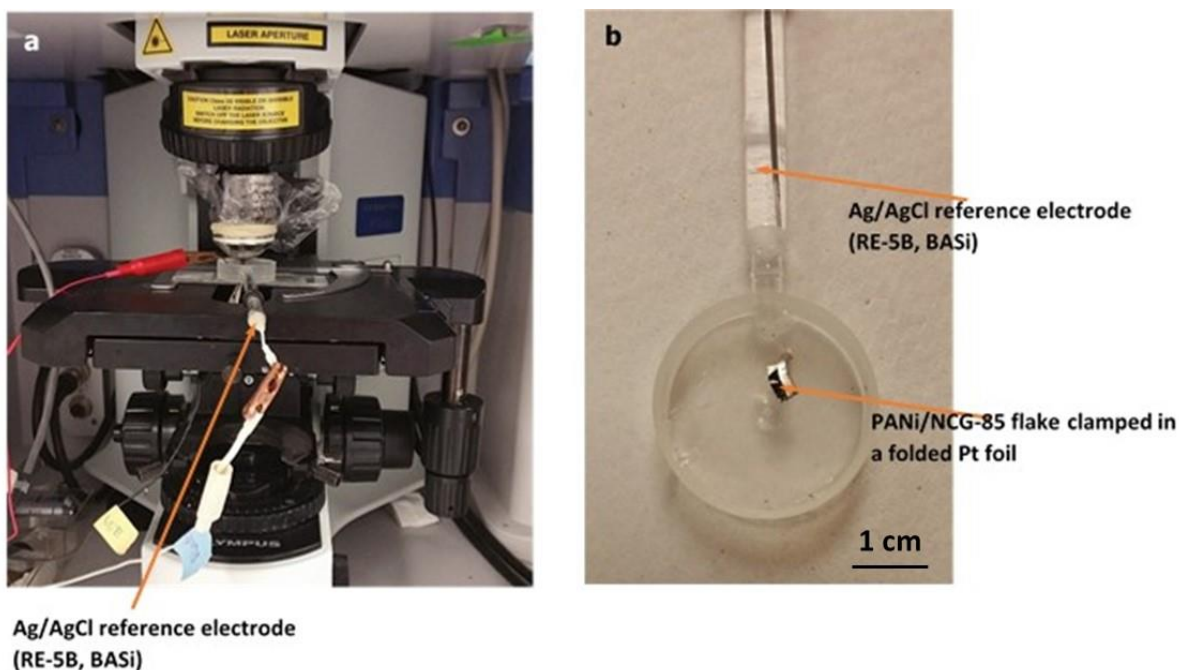
Figure 2.2 (a) Operando Raman spectroscopy setup, based on an ARAMIS (Horiba) Raman microscope and a HDPE one-compartment spectroelectrochemical cell attached to a microscope glass. (b) Top-view of the spectroelectrochemical cell (4 mL).

2.3 Electrochemical Characterization

All of the electrochemical characterization carried out in this thesis work was conducted in a three-electrode cell (Fig. 2.1b). N_2-saturated 3 M NaCl was selected as the electrolyte in order to understand the electrochemical behavior of the materials in neutral saline water. The working electrode was the same as shown in Fig. 2.1a, where a piece of NCS or PANi/NCS (1×1 cm^2) was placed between a Au-coated slide and a perforated glass slide, wrapped with Parafilm^{TM}. A Pt gauze and a Ag/AgCl electrode (3M NaCl, RE-5B, BASi) were used as the counter and reference electrodes, respectively.

2.3.1 Cyclic voltammetry (CV)

Cyclic voltammetry (CV) is a powerful tool used to understand the kinetics and mechanisms of electrochemical processes and phenomena, including the electrical double layer and redox reactions [83]. All CV experiments were carried out using a SP-150 potentiostat (Bio-Logic SAS) at room temperature. CVs were obtained at various scan rates of 1, 5, 10, and 20 mV s^{-1} over a potential range from -0.5 V to 0.5 V vs. Ag/AgCl.

The specific capacitance of the electrode materials studied here was calculated by integrating the CV over -0.5 to 0.5 V:[54]

$$C_m = \frac{\int I\mathrm{d}V}{v\Delta V \cdot m} \tag{2.1}$$

where C_m is the specific capacitance (F/g), I is the current (A), v is the scan rate (V/s), ΔV is the potential window of the integration (V), and m is the electrode mass (g).

2.3.2 Electrochemical impedance spectroscopy (EIS)

Electrochemical impedance spectroscopy (EIS) has proven to be a useful tool to understand the porous structure of porous materials [84]–[86]. In an EIS test, a sinusoidal voltage with a small amplitude is applied between the working and the reference electrode, while the response current is recorded over a wide range of frequencies. The complex impedance of the system can then be calculated by dividing the voltage by the current. The complex capacitance can then be calculated from the complex impedance (eq. 3), and the information can be analyzed accordingly.

The EIS data of NCS and PANi/NCS composites were collected at the open circuit potential (OCP) over a frequency range between 100 kHz to 10 mHz at an amplitude of 10 mV. All EIS data were collected using a SP-150 potentiostat (Bio-Logic SAS) at room temperature. The complex capacitance was calculated based on equation (2.2) using Excel software [84]–[86],

$$C'(\omega) = \frac{-Z''(\omega)}{\omega|Z(\omega)|^2}, \qquad C''(\omega) = \frac{Z'(\omega)}{\omega|Z(\omega)|^2} \qquad (2.2)$$

where $C'(\omega)$ is the real part of the complex capacitance, $C''(\omega)$ is the imaginary part of the complex capacitance, $Z'(\omega)$ and $Z''(\omega)$ are the real and the imaginary parts of the complex impedance $Z(\omega)$, $|Z(\omega)|^2 = |Z'(\omega)|^2 + |Z''(\omega)|^2$, and ω is the angular frequency, $\omega = 2\pi f$, where f is the frequency in Hz.

2.3.3 Galvanostatic charge/discharge (GCD)

Galvanostatic charge/discharge (GCD) is a common method for determining the capacitance, energy density and power density of capacitors.[87] A constant current is applied to the electrode to charge/discharge the electrode over a potential window, which is usually 1 V for aqueous solutions [87].

The GCD measurements were conducted at various currents, i.e., 1, 2, 5, 10, and 20 mA, in a voltage range between -0.5 V and 0.5 V vs. Ag/AgCl. A SP-150 potentiostat (Bio-Logic SAS) was used to control the current in the GCD experiments and measurements. The specific capacitance was calculated using the equation below [53]:

$$C_{sp} = \frac{I \Delta t}{\Delta V \cdot m} \tag{2.3}$$

where C_{sp} is the specific capacitance (F/g), I is the applied discharge current (A), Δt is the discharge time (s), and ΔV is the potential change during discharge (excluding potential drop) (V).

The energy density and power density of the studied materials (e.g., NCS and PANi/NCS) were calculated from the GCD data by using equations (5) and (6) [88]:

$$U = \frac{\frac{1}{2} C_{sp} \Delta V^2}{3.6} \tag{2.4}$$

$$P = \frac{3600 U}{\Delta t} \tag{2.5}$$

where U and P are the energy density (Wh/kg) and power density (W/kg) of the working electrode (e.g., NCS or PANi/NCS).

The stability testing of NCS-85 and PANi-6/NCS-85 was carried out at 2 mA between 0.5 V to -0.5 V vs. Ag/AgCl for 1000 cycles in a 3 M NaCl solution.

2.4 Capacitive deionization experiments

The CDI cell configuration is shown in Figure 2.3. The CDI cell consisted of polycarbonate covers, which were 3D printed using a 3D printer, gaskets (McMASTER-CARR), carbon fiber paper (Avcarb MGL280) as the current collector, and glass fiber paper as the separator. The NCS or PANi/NCS electrodes were 2 cm × 2.5 cm (80 μm thick) and were contacted to the carbon fiber paper using the Epoxy (Devcon). The CDI cell was operated in the single-pass flow-through mode.

The water reservoir contained 1 L of 10 mM NaCl solution as the feed water, which was pumped through the cell at a flow rate of 1.5 mL/min. The conductivity of the effluent water was measured with a conductivity meter (SevenCompact™ Duo S213, with an Inlab® 731-ISM probe, METTLER TOLEDO). The CDI cell was charged at a constant voltage and was then discharged at zero voltage.

The salt adsorption capacity (Γ, mg/g) was calculated by [88]:

$$\Gamma = K\phi \int (\sigma - \sigma_0)dt \tag{2.6}$$

where K is the calibration coefficient, $K = M/(km)$, M is the molecular weight of the salt (mg/mmol), k is the slope of the calibration curve (μS cm^{-1} mM^{-1}), m is the total weight of the CDI electrodes (g), Φ is the flow rate (L/min), σ is the conductivity of the effluent (μS cm^{-1}), σ_0 is the initial conductivity (μS cm^{-1}), and t is the charging time (min).

An average salt adsorption rate (SAR) was also calculated by dividing Γ (mg/g) by the adsorption time (t_{ad}, min) [13]:

$$SAR = \frac{\Gamma}{t_{ad}} \tag{2.7}$$

The energy consumption (U_{con}) was calculated as follows:

$$U_{con} = \frac{\int IVdt}{3.6Ft} \tag{2.8}$$

where I is the recorded current during the CDI charging process (A), t is the charging time (s), V is the CDI operation voltage (V), and F is the flow rate (m^3/s).

The combination of ultrafiltration (UF) and CDI was also carried out, using the same CDI cell. The feed solution in this experiment was 10 mM NaCl solution with suspended Au nanoparticles (~10 nm particle size) and the effluent water was collected in a vial.
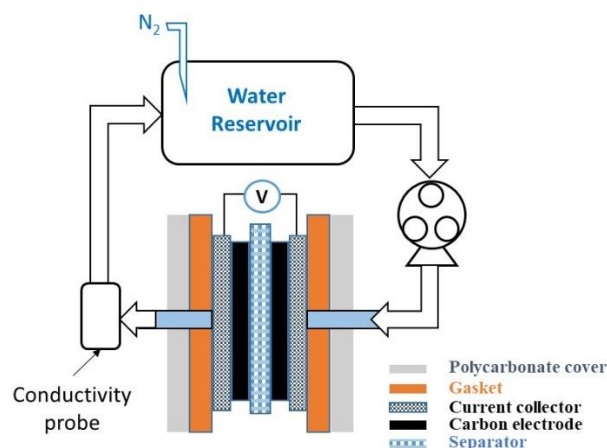
Figure 2.3 The CDI cell was composed of polycarbonate covers, gaskets, carbon fiber paper current collectors, NCS or PANi/NCS electrodes and a separator. The solution was pumped from a reservoir containing 1 L of 10 mM NaCl solution into the CDI cell. The solution was driven through the electrodes and the conductivity of the effluent water was measured at the outlet of the cell. The effluent was then flowed back to the solution reservoir.

2.5 Error Analysis

The NCS materials used for all experiments in this thesis work were made from the same batch, with a minor variance in properties. The PANi coated NCS samples were prepared using the same potentiostat and using the same electrochemical conditions, giving a reproducibility of its CV charge of +/- 5%.

The major errors of the TGA data arose from the temperature and weight specifications of TGA/DSC 3+ instrument (METTLER TOLEDO). Specifically, the error of the measured temperature is $\pm$ 0.25 K, and that of the measured weight is 0.005%.

The error in the N_2 adsorption/desorption measurements was reported in the manual of the Gemni VII Surface Area Analyzer, where the pressure measurement has an error $\leq$ 0.5%. The weight of the tested NCS-85 and PANi-6/NCS-85 samples was measured using a balance (Sartorius MSA224S100DI Cubis Analytical Balance) with an error of $\pm$ 0.1 mg.

The content of C, O and N determined by elemental analysis was determined only once with an estimated error < 6%.

The error in the current and potential measured in CV testing is ± 0.2%, according to the user manual of the potentiostat (Metrohm potentiostat). The CV experiments for all tested samples were repeated at least twice. The plotted CV curves in this thesis work were the average of at least two CVs collected from the experiments and the reproducibility was found to be ± 1.7%. The calculated C_m from the CVs has an error smaller than 4%.

The error in the current and potential when using the SP-150 potentiostat for EIS and GCD testing was estimated at < 0.1% and the error in frequency was ± 1%. The GCD experiments for all samples were repeated at least twice and the plotted GCD data was the average of at least two sets. The error of the calculated C_{sp} was estimated to be <1.5%.

The capacitive deionization experiments were each repeated twice, giving a reproducibility of ± 12%. The error of the measured conductivities is reported from the manual of the SevenCompact^{TM} Duo S213 conductivity meter, which is ± 0.5%

Chapter 3

Electrochemical Formation of Highly Ordered, Self-Supported Polyaniline/Carbon Composite Scaffolds with Fully Controlled Nanopore Sizes

Chengying Ai[a], Irina V. Chernyshova[c], Erin L. Gawron[a], Sathish Ponnurangam[a], and Viola I. Birss*[b].

[a] Department of Chemical and Petroleum Engineering, Schulich School of Engineering, University of Calgary. 2500 University Drive NW, T2N 1N4, Calgary, AB, Canada. E-mail: sathish.ponnurangam@ucalgary.ca

[b] Department of Chemistry, University of Calgary. 2500 University Drive NW, T2N 1N4, Calgary, AB, Canada. E-mail: birss@ucalgary.ca

[c] Department of Earth and Environmental Engineering, Columbia University, New York, NY, USA. E-mail: ic2228@columbia.edu

Highlights

- A conformal polyaniline (PANi) coating with a thickness of a few nanometers has been electrochemically deposited into a nanoporous carbon scaffold (NCS) at ambient temperature.
- The porous structure of the original NCS is fully retained after coating it with the polymer.
- The thickness of the PANi film can also be fully controlled, while retaining the monodisperse porosity.
- A significantly enhanced electrochemical capacitance due to the PANi coating is obtained.

Abstract

The use of composite materials, including conducting polymer-coated carbons and transition metal oxide-coated carbons, has been shown to be a promising approach to increase the electrochemical capacitance compared to carbons alone in supercapacitors and capacitive deionization (CDI) applications. Coating of polymers onto nanoporous carbon materials without clogging the pores is a challenge. In this work, a thin, conformal polyaniline (PANi) film was coated on the internal surface of a novel nanoporous carbon scaffold (NCS, 50-100 nm pore size)

by the *in-situ* potentiodynamic method. Nitrogen sorption analysis demonstrated that the PANi/NCS composite has a 5% lower surface area and 1% - 50% smaller pore size as compared to NCS itself, which is due to the deposition of PANi into the porous structure. *In situ* Raman spectroscopy revealed that PANi is in the conducting state at the open circuit potential (OCP) in neutral solutions. Electrochemical analysis, including cyclic voltammetry and electrochemical impedance spectroscopy, has been conducted, and the results show that PANi/NCS composites have an electrical capacitance that is 5 - 20 times that obtained from the original NCS. The increased capacitance of PANi-coated NCS indicates a better electrosorption capacity than NCS alone. These findings provide insight into the enhanced electrochemical performance of PANi/NCS composites and their promising future applications in CDI and supercapacitors.

3.1 Introduction

There has been rapid growth in the synthesis and application of nanomaterials (NMs) due to their unique physical, chemical and biological properties and enhanced performance [8], [89]. Due to the low specific gravity, good electrical conductivity, high surface area and readiness for scale-up, carbonaceous/graphitic materials with nanoscopic structures have been extensively studied and widely applied in many fields [90], [91], e.g., in electrochemical devices, sensors, adsorbents and more.

Colloidal imprinting is one of the approaches to synthesize carbon materials with a nanoengineered porous structure [92], [93]. Colloidal-imprinted carbons (CICs) contain fully tunable and ordered monodisperse pores (10-100 nm in diameter), which are being considered as catalytic supports in proton-exchange membrane fuel cells [94], solid contacts in ion-selective electrodes [95], and so forth [96], [97]. While most CICs are powders, which raise health concerns

and application limitations [98]–[100], a self-supported nanoporous carbon scaffold (NCS) has shown promise in overcoming the problems of powdered carbons [77]. The NCS, with controllable, interconnected nanopores (5 to 100 nm in diameter) and an adjustable thickness (0.5 to 100 µm), has also been tested as a filtration membrane. It has been shown to completely remove particulates, bacteria, as well as most viruses from filtered samples [77]. Its high conductivity, good electrical capacitance and low tortuosity make it very suitable for broad applications, such as electrodes, adsorbents, catalysts, separators and sensors [100]–[102].

While the NCS has a very good gravimetric capacitance, ranging from 45 to 95 F/g in acidic solutions (0.5 M H_2SO_4) at a scan rate of 10 mV/s, as well as low tortuosity [77], further improvements are desired for better and broader applications. For example, applications such as combining membrane filtration with capacitive deionization, could be explored. The incorporation of conducting polymers, such as polyaniline into carbon, has been carried out to produce composites with enhanced performance [63], [103].

Polyaniline (PANi) is a widely studied conducting polymer that is environmentally friendly and easy-to-synthesize. PANi has three forms: leucoemeraldine (fully reduced), emeraldine (half-oxidized), and pernigraniline (fully oxidized) (Scheme 3.1), where the emeraldine salt (ES) form has the highest conductivity and both leucoemeraldine and pernigraniline are insulators, even after protonation [65]. The high conductivity of the ES is explained by the presence of polarons (radical cation units in which the π electrons are delocalized) [64]. Because of its significant theoretical electrical capacitance (~740 F/g) [62], PANi is commonly combined with carbon materials to increase their electrochemical performance. In addition, PANi coatings can increase the electrical conductivity of carbon by nearly one order of magnitude, increase the surface hydrophilicity, and improve the stability of porous carbon under anodic conditions [63].

PANi/carbon composites have been prepared by various methods, including chemical oxidation, electrochemical polymerization and direct casting, resulting in a diverse set of morphologies including nanowires, nanowhiskers, nanoparticles and nanofibers [37], [67], [104]. A conformal PANi coating into the NCS pores would be preferred in order to enhance the NCS electrochemical performance without losing the unique porous structure of NCS (Scheme 3.2). Thin PANi layers have been synthesized by chemical oxidation, electro-polymerization or plasma polymerization. Tan et al. claimed the formation of a conformal PANi film inside carbon with hierarchical porosity, including micrometer scale pores (mainly 20 µm and 2 µm) as well as nanopores (10 – 100 nm) , using in-situ chemical oxidation [105]. Smolin et al. reported the formation of a conformal PANi coating in micro/mesoporous carbide-derived carbon powders (with pore sizes of 0.8- 3.4 nm) through oxidative chemical vapor deposition [70]. Goktas et al. also reported the coating of an ultrathin conformal PANi film into the micro/mesopores of carbon powders by plasma polymerization [106].

Dinh et al. prepared a smooth, uniform and thin PANi film on a Au substrate by cyclic voltammetric scanning, which was also reported by Yoon et al. [107], [108], with the Dinh method used in this thesis work. Thin layers of PANi were also shown to be electrochemically coated into three-dimensionally ordered macroporous carbons while maintaining the pore structures, as reported by Zhang et al [68].
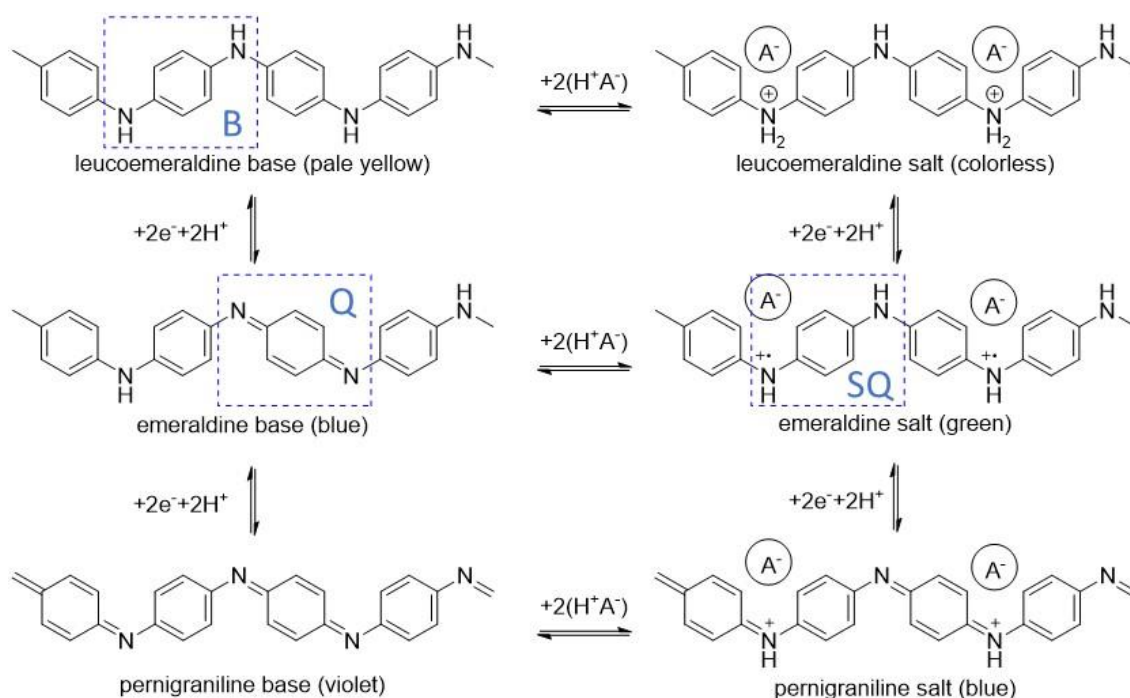
Scheme 3.1: Main forms of PANi (benzenoid (B), quinonoid (Q), and semi-quinone (SQ) units).
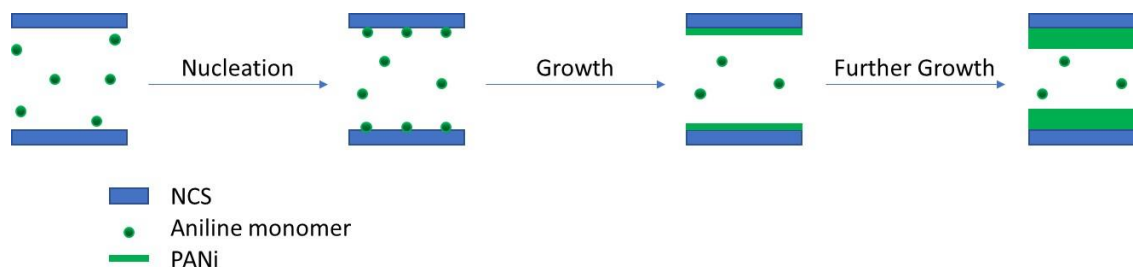
Scheme 3.2: Preparation method used to obtain a conformal PANi coating inside the pores of NCS (a cross-sectional view).

In this paper, thin PANi films with a controlled thickness, varying from 1 to 20 nm, were coated conformally on the full inner surface of the NCS material (50 nm or 85 nm pore diameter) using a potentiodynamic method. Characterization of the PANi film was accomplished using several techniques, including field emission scanning electron microscopy (FESEM), thermal

gravimetric analysis (TGA) and operando Raman spectroscopy. The PANi/NCS composites were found to retain the nanostructure of the NCS, but with smaller pores, as expected. Cyclic voltammetry analysis showed that the electrochemical capacitance of the as-prepared PANi-6/NCS-85 material is as high as 390 F/g, which is more than 20 times that of the NCS-85 alone (18 F/g). The quasi-reversible behavior of PANi/NCS composites observed from the IR-corrected CVs indicates rapid PANi redox chemistry throughout the NCS thickness, although the time constant decreases a little after PANi deposition. The enhancement in electrochemical performance while maintaining a tunable porous structure makes the PANi/NCS composite very promising in supercapacitor and capacitive deionization applications.

3.2 Experimental methods

3.2.1 Preparation of NCS

The NCS film was prepared, based on a method developed by Li et al [77]. The procedure used to prepare NCS with a nominal pore size of 50 nm or 85 nm are given here. Mesophase pitch (0.6 g, MP, AR Grade, Mitsubishi Chemicals, Japan) and 2.4 g n-butanol were mixed in a 20 mL low density polyethylene (LDPE) bottle and then ball-milled (70 rpm, 2 hours) using 32 g of alumina balls (4 mm in diameter). Polyvinyl alcohol (9.6 g of 15 wt% PVA, Alfa Aesar, 86-89% hydrolyzed) in water was then added and the mixture was then ball-milled for another 3 h to produce a homogeneous MP/PVA ink. A colloidal silica suspension (NanoSol-5080S, in this case with an average colloid size of either 50 nm or 85 nm), containing 3 g of silica, was added to 6 g of 1,3-propanediol (PD) and water (mass ratio: 1:1) to produce a silica suspension. (Note: All of the colloids were stabilized with Na cations). The silica suspension of selected silica nanoparticle size was added to the MP/PVA ink and the mixture was ball-milled for 4 h to obtain the

MP/PVA/PD/silica ink (or slurry). The ink was degassed under house vacuum for 30 min to remove any trapped gas bubbles before use.

The slurry was then cast on a glass substrate using a casting blade with a 0.003 inch (0.076 mm) gap between the doctor blade and the substrate. After drying, a pristine composite MP/PVA/PD/silica film was obtained. Six such films were then pressed together to form one 6-layer film. The film was placed between two carbon-coated alumina plates, inserted into an alumina tube in a 1500 °C furnace (Thermo Scientific) and carbonized at 900 °C for 2 h in a nitrogen atmosphere, heating at a ramp rate of 0.1-2 °C/min. Prior to reaching 900 °C, the temperature was held at 400 °C for 2 h.

After cooling, the carbonized films were soaked in 3 M NaOH at 80 °C for 2 days to remove the silica template. Following this, the films were soaked in dilute HCl for one day to remove any retained NaOH. After washing with deionized water several times, the films were air dried at 80 °C overnight. The resulting self-supporting nanoporous films were stored in a conductive environment, e.g., Al foil covered Petri dishes, to avoid electrostatic effects. These nanoporous carbon films were labelled as NCS-xx, with "xx" corresponding to the template silica particle size used, for example, NCS-50 and NCS-85, which are NCS materials with 50 nm and 85 nm pore sizes, respectively. The typical thickness of the as-prepared NCS is 60 - 80 µm.

3.2.2 Preparation of PANi/NCS composites.

PANi was deposited on NCS using a potentiodynamic method [74]. NCS was used as the working electrode in a three-electrode system (Fig. S3.1 (b)). A 1 cm^2 piece of NCS was sandwiched between a gold-coated glass slide (DRLI) and a perforated glass slide as the working electrode, wrapping the edges with Parafilm M (PM-996, Bemis NA) (Fig. S3.1 (a)). A Pt gauze

and a Ag/AgCl electrode (RE-5B, BASi) were used as the counter and reference electrodes, respectively. PANi was deposited into NCS using cyclic voltammetry (CV), where the working electrode was immersed in an electrolyte containing 0.1 mol L^{-1} aniline (ACS reagent, SIGMA-ALDRICH) and 1 mol L^{-1} H_2SO_4 and was scanned between -0.222 to 0.828 V at a sweep rate of 5 mV/s. Aniline was used as purchased. The CV experiments were conducted using a potentiostat (Solartron Analytical 1480 MultiStat). PANi/NCS composites, prepared by X CV cycles, are named as PANi-X/NCS. For example, PANi-6/NCS-85 was prepared by conducting 6 CV cycles on NCS-85 in the aniline solution.

3.2.3 Physical Characterization

The morphology of the as-prepared samples was determined by FE-SEM (Zeiss Sigma VP) at an accelerating voltage of 8 kV. The elemental composition of these samples was determined by Energy Dispersive X-ray spectroscopy (EDX) using a Philips/FEI instrument at an accelerating voltage of 15 kV. The thermal stability was determined with a thermogravimetric analyzer (TGA/DSC 3+, METTLER TOLEDO), heating from 50 ˚C to 1000 ˚C at a ramp rate of 10 ˚C/min in nitrogen. N_2 adsorption/desorption isotherms were obtained using a Surface Area Analyzer (Gemni VII, Micromeritics) at 77 K. Before the measurement, NCS and PANi/NCS were degassed at 200 ºC and 40 ºC for 4 hours, respectively. The specific surface area and the pore size distribution were calculated by using the Brunauer-Emmett-Teller (BET) and Barrett-Joyner and Halenda (BJH) methods.

The structural and redox properties of the PANi films were characterized *in situ* using Raman spectroscopy. The spectra were recorded using a LABRAM-ARAMIS confocal Raman microscope with a 600 grooves/mm diffraction grating and a UPlanApo/IR 60X (Olympus) water-

immersion objective with a working distance of 0.2 mm. As the excitation source, a HeNe (633-nm) laser with a nominal power of 17 mW was used, with and without attenuation. All Raman spectra were acquired for the samples while immersed in 3 M NaCl. The *in-situ* spectra were collected at the OCP without applying a potential. The spectra were processed and represented using OriginPro software. The processing involved subtracting the spectrum of the NCS and blank background from the spectra of the PANi/NCS composites.

3.2.4 Electrochemical characterization

The NCS and PANi/NCS composites are free-standing carbon films and were used as the working electrodes without adding any binder. The same working electrode configuration as used in PANi/NCS preparation was used here (Fig. S3.1). Cyclic voltammetry (CV), galvanostatic charge/discharge (GCD) experiments, and electrochemical impedance spectroscopy (EIS) were carried out in a three-electrode cell containing 3 mol L^{-1} N_2-saturated NaCl solution, a Pt gauze as the counter electrode, and a Ag/AgCl (3M NaCl) electrode (RE-5B, BASi) as the reference electrode. All electrochemical tests were carried out using a SP-150 potentiostat (Bio-Logic SAS) at room temperature and in neutral solutions in order to demonstrate the behaviour of the NCS and PANi/NCS materials in neutral salt solutions for possible application in CDI. The CVs were obtained at various scan rates of 1, 5, 10 and 20 mV s^{-1} over a potential range from -0.5 V to 0.5 V vs. Ag/AgCl. The gravimetric (C_m) and areal specific capacitance (C_a) were calculated using equation (1) [54],

$$C_m = \frac{\int I \mathrm{d}V}{v \Delta V \cdot m}, C_a = \frac{\int I \mathrm{d}V}{v \Delta V \cdot A} \tag{1}$$

where C_m is the gravimetric specific capacitance (F/g) of either the NCS or the PANi/NCS composites, C_a is the areal specific capacitance (F/cm^2), I is the current (A), v is the scan rate (V/s), ΔV is the potential change (V), m is the electrode mass (g), and A is the geometric area of the working electrode, which in this work, was 1 cm^2.

The EIS data were collected at the OCP with an amplitude of 10 mV over a frequency range from 100 kHz to 10 mHz. The real and imaginary parts of the complex capacitance were calculated, based on equation (2) [84]–[86].

$$C'(\omega) = \frac{-Z''(\omega)}{\omega|Z(\omega)|^2}, \qquad C''(\omega) = \frac{Z'(\omega)}{\omega|Z(\omega)|^2} \tag{2}$$

where $C'(\omega)$ is the real part of the complex capacitance $C(\omega)$, $C''(\omega)$ is the imaginary part of the complex capacitance, $Z'(\omega)$ and $Z''(\omega)$ are the real and the imaginary parts of the impedance $Z(\omega)$, $|Z(\omega)|^2 = |Z'(\omega)|^2 + |Z''(\omega)|^2$, ω is the angular frequency, and $\omega = 2\pi f$, where f is the frequency in Hz.

3.3 Results and Discussion

3.3.1 Properties of NCS

The NCS is a free-standing carbon film with a nano-engineered porous structure. The as-prepared NCS-85 film has a three-dimensional interconnected structure with nanopores with a diameter of 85 nm (Fig. 3.1a). The thickness of the NCS-85 used here was roughly 80 µm. Pore necks of 11 nm can be found in NCS-85, which is a result of the contacting faces of the templating silica colloids [77]. NCS-50 was prepared using the same approach, but using a 50 nm silica template, as shown in Figure 3.1b. Both NCS-85 and NCS-50 possess a monodisperse pore structure.
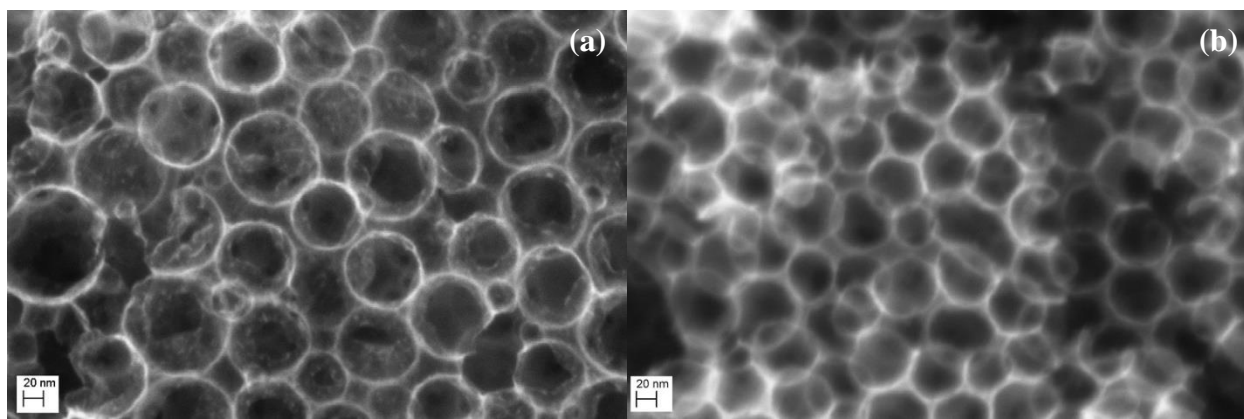
Figure 3.1 FESEM images of (a) NCS-85 with an average pore diameter of 85 nm and (b) NCS-50 with an average pore diameter of 50 nm.

The electrochemical behavior of the NCS materials was analyzed by cyclic voltammetry (CV). NCS-85 and NCS-50 were scanned between -0.5 to 0.5 V at various sweep rates from 1 mV/s to 20 mV/s (Figs. 3.2a and S3.2 (a)). The CV profiles of NCSs are quasi-rectangular, suggesting their close to ideal electrical double layer (EDL) capacitive behavior. The current switched from anodic to cathodic almost immediately after the reversal of the scan, suggesting fast ion transport. The anodic current at 0.0 V for both NCS electrodes is proportional to the scan rates, as seen in Figs. 3.2b and S3.2(b), indicating that the electrical capacitance remains the same over the tested scan rate range. C_m, calculated from the CV for NCS-85 and NCS-50 using eq. 1, is ca. 20 F/g and ca. 25 F/g, respectively.

(a)

(b)
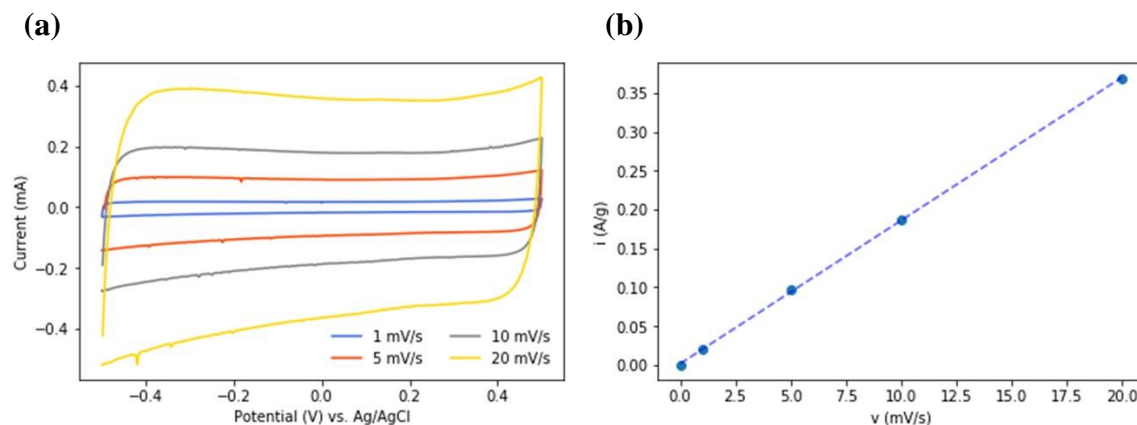
Figure 3.2 (a) Cyclic voltammograms of NCS-85 in N₂-saturated 3 M NaCl solution at various scan rates (1, 5, 10, 20 mV/s). (b) The relationship of anodic current density at 0.0 V vs. the scan rate.

3.3.2 PANi/NCS composite formation and characterization

The PANi/NCS composites were obtained by electropolymerizing aniline in sulfuric acid at a scan rate of 5 mV/s during potential scanning from -0.222 V to +0.828 V vs. Ag/AgCl (Fig. 3.3a shows the result for NCS-85). Peaks A and A' are related to the redox reactions of PANi, converting it from the leucoemeraldine (neutral) to emeraldine (radical cation) forms, while peak B' is associated with the reduction of the head-to-tail dimer, N-phenyl-p-phenylene (PPD) [109]. Peak B, which is associated with the further oxidation of emeraldine to pernigraniline (bication), was intentionally not fully reached in the PANi growth CV, as the conditions developed by Dinh et al were followed closely [110].

The as-prepared PANi/NCS-85 composites were named PANi-3/NCS-85, PANi-6/NCS-85 and PANi-12/NCS-85, based on the number of CV cycles used to deposit the PANi film. Conformal PANi coatings were observed from the FESEM images (Fig. 3.4) and the PANi coating thickness for these three samples was roughly 3 nm, 8 nm and 15 nm, respectively (Fig. 3.4a-c). The charge used to polymerize aniline was integrated from the PANi growth CV (Fig. 3.3a) and

50

plotted against the PANi thickness measured from the FESEM images. As can be seen in Fig. 3.3b, the thickness does not change linearly with the CV charge, perhaps because the very early stages of PANi growth involves the formation of nano-clusters. The density of the conformal PANi coating was calculated to be 0.27 ($\pm$0.06) g/cm^3.
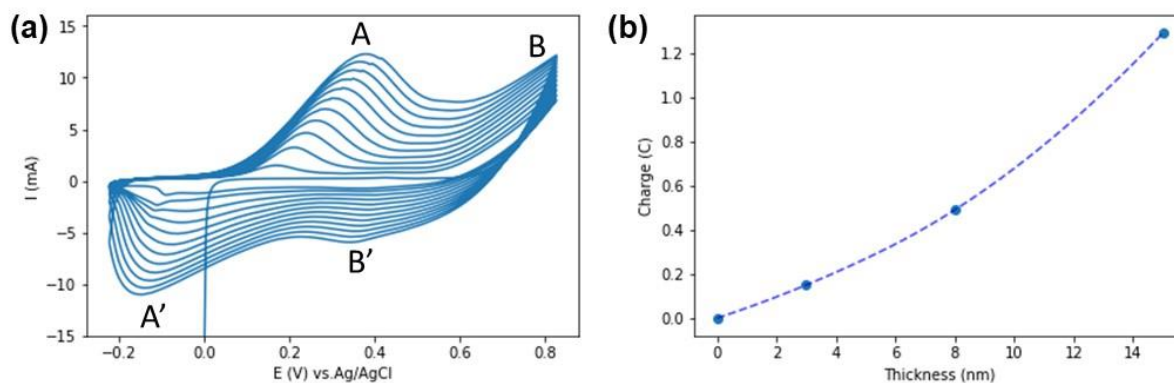
Figure 3.3 (a) Electrochemical polymerization of aniline at the NCS-85. The NCS-85 working electrode was scanned between -0.222 to +0.828 V vs. Ag/AgCl in 1 M H$_2$SO$_4$ containing 0.1 M aniline. (b) The charge from the growth CV vs. the PANi thickness of PANi-3/NCS-85, PANi-6/NCS-85, PANi-12/NCS-85, obtained from the FESEM images in Fig. 3.4.

Nitrogen mapping via Energy Dispersive X-ray spectroscopy (EDX) shows that nitrogen, contained in the PANi structure, was evenly distributed throughout the NCS film (Fig. S3.3 (a, c)), with the PANi coating having the same thickness in the center as seen on the outer surface of the PANi/NCS structure. The presence of Al in the EDX spectrum (Fig. S3.3 (c)) is due to the Al stub, and the presence of S and O can be attributed to the sulphate ion doped inside the PANi film from polymerization in sulfuric acid. To the authors' knowledge, this is first time that a conformal coating of PANi with a controllable thickness of < 25 nm has been formed uniformly throughout a nanoporous carbon scaffold, using an electrochemical method for PANi deposition. Similarly, a

51

conformal PANi film can also be coated into smaller pores, such as those in NCS-50 (Figs. 3.4d

and S3.3 (d,e)).
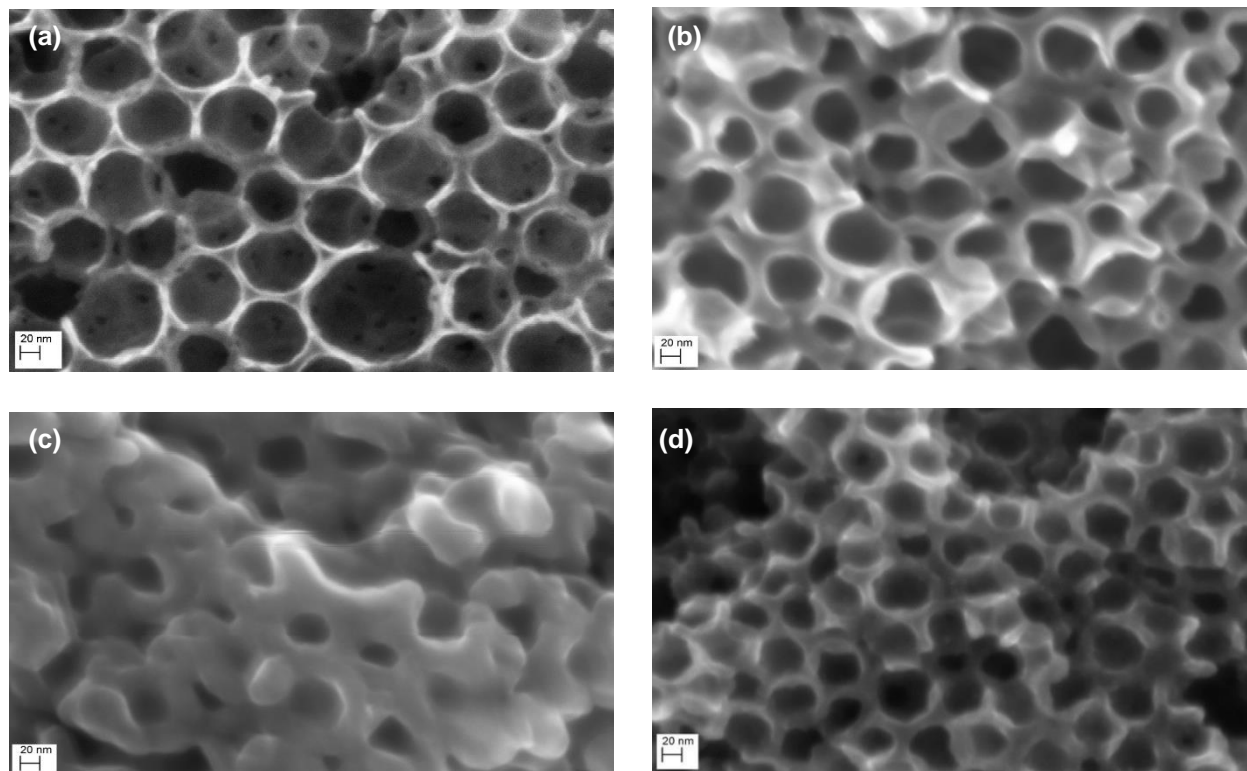
Figure 3.4 FESEM images of (a) PANi-3/NCS-85, (b) PANi-6/NCS-85, (c) PANi-12/NCS-85 and (d) PANi-6/NCS-50.

The formation of a PANi film with a conformal morphology inside the NCS nanopores

rather than a layer of nanospheres, nanorods or nanofibers, could be due to multiple reasons. When

polymerizing aniline at a faster scan rate of 50 mV/s between -0.222 to 0.828 V, the PANi film

was seen mainly on the outer surface of the NCS-85, as shown in Fig. S3.4a. Under these

conditions, it is seen that PANi formed aggregates and therefore blocked the nanopores of the

NCS-85. The use of an extended potential window (-0.222 to 1.4 V vs. Ag/AgCl) at 5 mV/s also

gave a compact PANi film primarily on the outer surface of NCS-85, instead of uniformly deposited inside the nanopores (Fig. S3.4 (b)).

In our case, a visibly smooth and conformal PANi layer was formed throughout the NCS pores at slow scan rates (e.g. 5 mV/s), while larger PANi particles were formed on the external surface of the NCS-85 at higher scan rates (50 mV/s). This is most likely due to the following processes that occur during the cycles of deposition. Small oligomers likely form first as nuclei, most of which would dissolve in H_2SO_4 and diffuse either into the porous structure or into the bulk solution [69]. During slow CV scans (e.g. 5 mV/s), the oligomers have enough time to penetrate through the full NCS-85 film. Thus, in the subsequent CV cycles when autocatalysis dominates, uniform films can be produced on the pore walls throughout the entire NCS structure. In contrast, with fast cycling (e.g. 50 mV/s), the oligomers would not have enough time to enter the pores and adhere to the surface of the NCS structure, and instead, they agglomerate on the outer surface of NCS. In addition, while sweeping at 50 mV/s, the IR drop inside the NCS pores is likely larger due to the higher currents passed, contributing to the growth of PANi only at the outer surface of the NCS.

Also, the limited potential window used in this work may help to generate a conformal PANi coating. During the growth period, oxidation peak B in Fig. 3.3a is related to the formation of the dication, which triggers the autocatalytic mechanism of PANi growth [109]. If growth stops before the dication-formation process is complete, a limited amount of dications form and the extended growth and branching mechanism of PANi formation is slowed, which would help to form a conformal PANi layer inside the nanoporous structure. The exact mechanism of PANi conformal growth inside the NCS material will require further studies, however.

Raman spectroscopy is a well-established method used to characterize the molecular structure and redox properties of PANi [111]–[113]. The Raman spectra in this work were collected in 3 M NaCl at the open circuit potential. Raman spectra of the PANi/NCS-85 composites synthesized in our work are very similar to the Raman spectra reported earlier for other PANi systems [75], [114]. As seen from Figure S3.5, the two broad peaks in the Raman spectrum of the NCS-85 at ca. 1330 and 1600 cm^{-1} correspond to the D and G peaks, which are related to the breathing modes of the carbon rings in NCS, due to defects, such as the edges of the graphite sheets and ordered graphite sheets, respectively [57]. The Raman spectra of PANi-3/NCS-85 are dominated by the relatively narrow PANi peaks. The peak at 1160 cm^{-1} is related to C-H bending in emeraldine and the peaks at 1330 and 1370 cm^{-1} correspond to the stretching of polarons (C~N$^{+\cdot}$), which indicate that PANi in the composite is in the conductive emeraldine form in neutral solutions at the open circuit potential.

The thermal stability of the NCS-85, PANi-6/NCS-85 and emeraldine salt (ES) has been determined by thermogravimetric analysis (TGA) over a temperature range between 50 to 1000 °C (Fig. 3.5a). The TGA data for the commercial ES powder (grey) show a sharp decrease from 240 to 360 °C, declining steadily afterwards. The NCS-85 material (blue) was very stable up to 1000 °C and retains 86% of its weight. PANi-6/NCS-85 (orange) is more thermally stable compared to the ES, due to the presence of NCS. The weight of PANi-6/NCS-85 gradually decreased and eventually remained at 74% of its original weight. The drop in the weight of the ES at 240 °C is due to the loss of dopants, following a steady weight loss afterwards, which is caused by the loss of PANi [115], [116]. The NCS membrane is much more stable because it was prepared by carbonizing at 900 °C in N$_2$. The PANi-6/NCS-85 material retained 74% of its weight, which

indicates a PANi content of 26 wt.%, assuming that it has been completely burned, consistent with

the elemental analysis results (28 wt% PANi, (Table S3.1)).
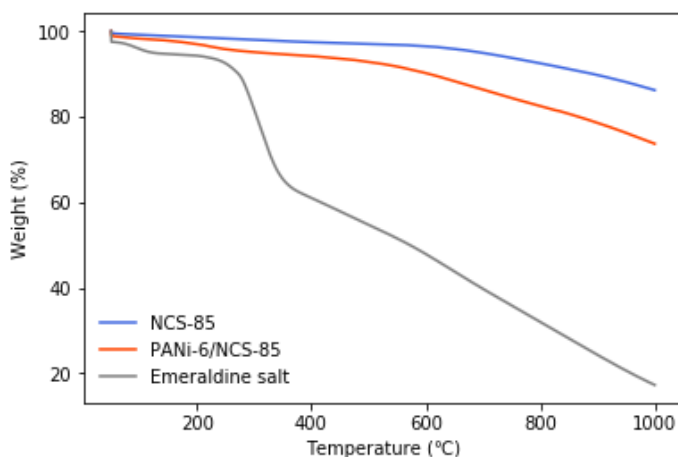
Figure 3.5 Thermogravimetric analysis (TGA) of the NCS-85, the PANi-6/NCS-85 composite and the commercial emeraldine salt (ES) while heating from 50 ˚C to 1000 ˚C in nitrogen at a ramp rate of 10 ˚C/min.

The gas physisorption isotherms of NCS-85 and PANi-6/NCS-85 show similar shapes

(Figure 3.6a). The BET surface area of NCS-85 is 145 ± 0.14 m^2/g, while the area of PANi-6/NCS-

85 decreased to 138 ± 11 m^2/g (Table 3.1). Based on the pore size distribution (Fig. 3.6b), the pore

neck diameters of NCS-85 and PANi-6/NCS-85 are 13 ± 2.0 nm and 11 ± 1.7 nm, respectively.

The original NCS-85 has nanopores with a diameter of 79 ± 12 nm. After PANi coating, the PANi-

6/NCS-85 composite shows nanopores with a diameter of 78 ± 12 nm. The N$_2$ isotherms indicate

that the pore structure of NCS-85 remains almost the same after PANi coating. The 5% decrease

in the specific surface area, as well as the increase in the sample weight (26% - 28% increase), are

attributed to the coating of the PANi film inside the nanopores of NCS-85. The slight decrease in

pore size also indicates the successful deposition of a conformal PANi layer, while maintaining

the porous structure of NCS material. The pore size difference obtained from the N$_2$ sorption did

55

not distinguish for PANi-6/NCS-85 and NCS-85, likely because of the relatively large error shown in the pore size distribution ($\leq 15\%$).
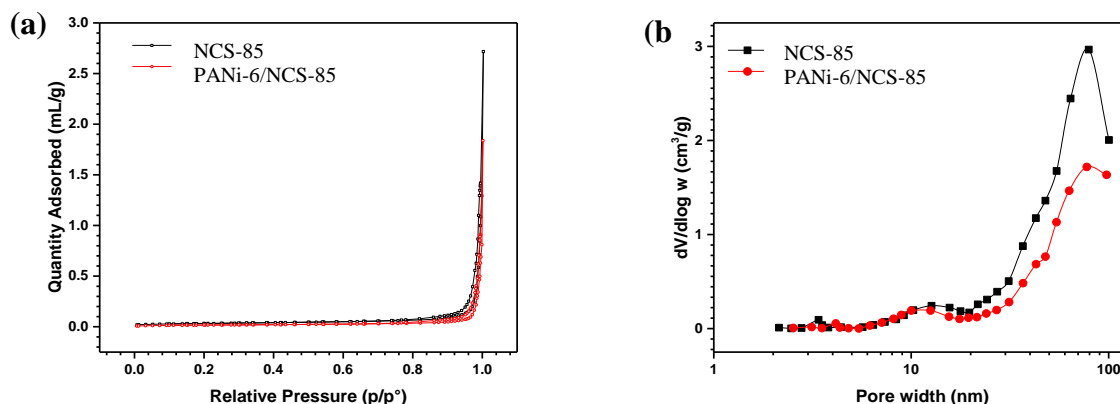
Figure 3.6 N$_2$ adsorption/desorption isotherm of (a) the NCS-85 and the PANi-6/NCS-85, while (b) gives the pore size distribution of NCS-85 and PANi-6/NCS-85.

Table 3.1 Specific surface area, pore volume and pore sizes of PANi-6/NCS-85

Sample	Pore size (nm)[a]	Pore neck width (nm)[a]	S_{BET} (m^2/g)[b]	$S_{external}$ (m^2/g)[c]	Volume (mL/g)[d]
NCS-85	79 ± 12	13 ± 2.0	145 ± 0.14	129 ± 0.9	1.9 ± 0.29
PANi-6/NCS-85	78 ± 12	11 ± 1.7	138 ± 11	130 ± 16	1.2 ± 0.18

[a] The pore size and pore neck values were obtained from the peaks in Figure 3.6b.
[b]: S_{BET} = Total surface area, obtained using the Brunauer-Emmett-Teller (BET) method using the Gemini VII 2390 software.
[c] $S_{external}$ = External surface area, obtained using the t-plot method using the Gemini VII 2390 software.
[d] Volume = Pore volume, obtained from N$_2$ adsorption isotherms at $P/P_0 = 0.998$ using the Gemini VII 2390 software.

3.3.3 Electrochemical performance of PANi/NCS-85 composites

As a powerful and popular electrochemical technique, cyclic voltammetry (CV) is commonly employed to analyze the electrochemical performance of carbon electrodes. The CVs

of PANi/NCS-85 composites were obtained in 3 M NaCl by scanning from -0.5 V to 0.5 V vs.

Ag/AgCl at a scan rate of 1 mV/s, as shown in Figure 3.7a. Unlike NCS-85, which has a rectangular

CV shape, the CV profile of PANi/NCS-85 composites shows oxidation and reduction peaks at

around 0.15 V and -0.06 V, respectively. The pair of broad peaks in the PANi/NCS-85 CVs has

been reported in the literature as being due to the overlap of the two typical PANi peaks commonly

seen in acidic solutions, which are related to the doping/de-doping processes (redox reaction

between leucoemeraldine and emeraldine) and a deprotonation/protonation process (redox

reaction between emeraldine and pernigraniline) [117], [118]. These redox reactions contribute a

pseudo-capacitance to the overall capacitance of the PANi/NCS composite and thus the

gravimetric capacitance (C_m) of the PANi/NCS composites is 4 – 20 times that of NCS-85 itself

and the areal capacitance (C_a) of PANi/NCS becomes 7-25 times that of the uncoated NCS (Table

3). The C_m and C_a of PANi-6/NCS-50 are 214 F/g and 0.4 F/cm^2, respectively, which is ca. 10

times that of NCS-50.

Figures 3.7b and S3.6 (a) show the CVs of PANi-6/NCS-85 and PANi-6/NCS-50, collected

at sweep rates from 1 to 20 mV/s. The peak potential shifts towards higher potentials as the scan

rate is increased from 1 mV/s to 20 mV/s. This peak shift may be due to the presence of a series

resistance (R_s), which can be measured by electrochemical impedance spectroscopy (EIS). R_s for

the PANi-6/NCS-85 experiment was thus found to be 13 Ω (Fig. S3.7) and the IR-corrected CVs

then shows much less peak separation (Fig. 3.7c). After IRs-correction, the peak currents (I_{peak})

for the PANi-6/NCS-85 and PANi-6/NCS-50 materials are linearly correlated with the square root

of the scan rate ($v^{1/2}$) at a scan rate > 5 mV/s, as shown in Figs. 3.5e and S3.6c, likely indicating a

diffusion-controlled electrochemical reaction at higher scan rate ($\geq$ 5 mV/s) [83]. The IRs-

corrected peak potential now varies only weakly with the logarithm of scan rate (log v), as shown in Figure 3.7d, likely due to some irreversibility of the PANi redox reactions. As the peak potential remains almost constant (Fig. 3.7d), the PANi redox reaction can be considered to be kinetically quite rapid, even at a fast scan rate of 20 mV/s.
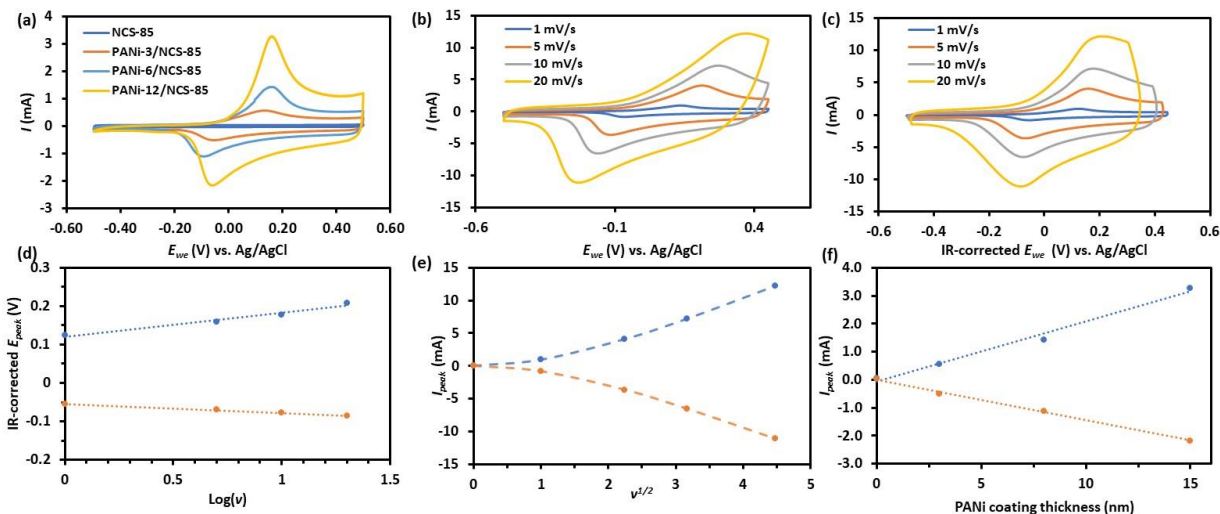
Figure 3.7 CVs of (a) NCS-85, PANi-3/NCS-85, PANi-6/NCS-85 and PANi-12/NCS-85 at a scan rate of 1 mV/s, (b) CVs of PANi-6/NCS-85 at various scan rates, and (c) IR-corrected CVs of PANi-6/NCS-85, all between -0.5 and 0.5 V vs. Ag/AgCl in 3 M NaCl solution. The relationship between (d) the IR-corrected peak potentials and the logarithm of the scan rate of PANi-6/NCS-85, (e) the peak current vs. the square root of the sweep rate of PANi-6/NCS-85, and (f) the peak currents collected from the CVs at 1 mV/s vs. the PANi coating thickness (determined by SEM analysis).

The CV peak current for the PANi/NCS-85 composite in 3 M NaCl at a scan rate of 1 mV/s increases proportionally with the PANi coating thickness (Fig. 3.7f). At a constant scan rate, a larger peak current seen in the CVs generally represents a higher specific capacitance at that potential. The linearity between the peak current and the PANi coating thickness shows that, at this very slow scan rate (1 mV/s), when diffusion limitations are likely to be small, the PANi redox reaction is likely fully reversible such that the capacitance increases linearly with the PANi film

thickness. From this figure, PANi-6/NCS-85 is found to have an electrochemical capacitance of 151 F/g in 3 M NaCl at 1 mV/s, which is 7 times higher than that of NCS-85 alone (17 F/g). The increase in capacitance can be fully attributed to the pseudo-capacitance contributed by PANi. This makes the PANi/NCS-85 composites a very good candidate for applications in capacitive deionization (CDI) and supercapacitors.

Table 3.2 The gravimetric capacitance (C_m, F/g) and areal capacitance (C_a, F/cm^2) of NCS and PANi/NCS composites, calculated from eq. (1).

Sweep rate (mV/s)	NCS-85		PANi-3/NCS-85		PANi-6/NCS-85		PANi-12/NCS-85		NCS-50		PANi-6/NCS-50	
	C_m	C_a	C_m	C_a	C_m	C_a	C_m	C_a	C_m	C_a	C_m	C_a
1	17	0.033	100	0.22	151	0.40	389	0.83	22	0.033	214	0.40
5	18	0.036	95	0.21	143	0.29	332	0.71	23	0.034	212	0.40
10	18	0.036	92	0.20	135	0.26	303	0.64	22	0.033	210	0.39
20	17	0.036	86	0.19	113	0.24	248	0.53	22	0.033	198	0.37

Electrochemical impedance spectroscopy (EIS) is regarded as a very useful tool for the evaluation of the pore structure of porous carbon electrodes. The Nyquist plot of all tested samples gives a semicircle at high frequencies and a straight line with an angle of around 85˚ at low frequencies (Fig. S3.7). The diameter of the semicircle at high frequencies likely arises from the carbon redox reaction (which has a resistance) and charging currents at the outer surface of the electrode, as the frequency is too high for ions to have enough time to enter/leave the pores. The differences seen in the high frequency intercept (R_s) for the different films could be due to a change in the relative position of the working and reference electrodes in each experiment.
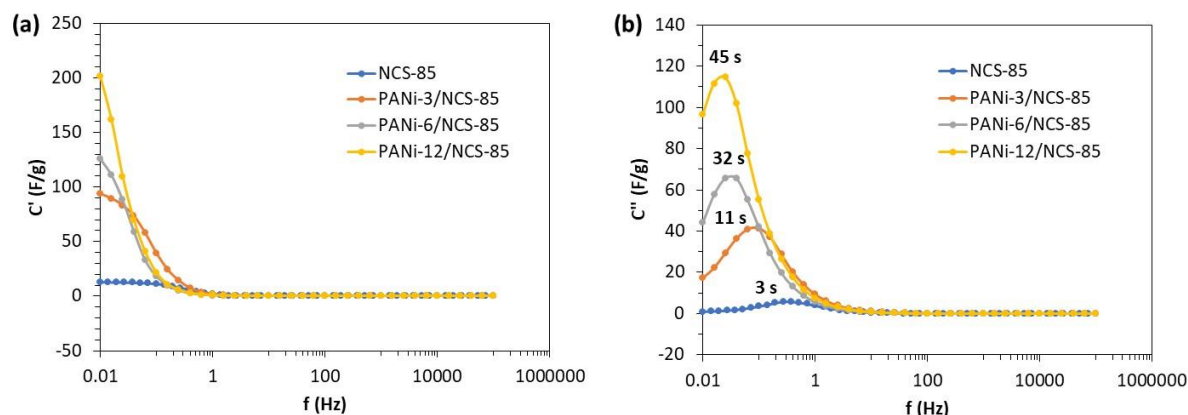
Figure 3.8 (a) The real part of the complex capacitance, (b) the imaginary part of the complex capacitance of NCS-85 and the PANi/NCS-85 composites, calculated from the EIS data collected at the open circuit potential in 3 M NaCl over a frequency range from 100 kHz to 10 mHz.

The real (C') and the imaginary (C'') parts of the complex capacitance were calculated according to eq. (2) [84] and plotted against the frequency in Fig. 3.8. The C' of the PANi/NCS-85 composites is larger than that for NCS-85 at low frequencies (10 – 100 mHz), indicating the increased capacitance after deposition of the PANi coating. The imaginary capacitance profile goes through a maximum at a particular frequency (f_m), from which a time constant (τ) could be calculated: $\tau = 1/f_m$. The time constant is a good indicator of the rate capability, i.e., the rate at which the full capacitance of the NCS or PANi/NCS material can be fully reached [86].

The time constant increased with the PANi coating thickness, which means the time for the electrode to be charged to its highest capacitance is longer, leading to a decreased rate performance for ions to move into or out of the pores of the thicker NCS or PANi/NCS. This indicates an increase in the barrier for mass transport of Na$^+$ or Cl$^-$ ions in the porous NCS structure, which could be attributed to the narrowed pore diameter after PANi coating, as seen in Fig. 3.4. Therefore, the as-synthesized NCS-85, which has the largest pore diameter, has the smallest time

constant (3 s). With more PANi coated inside the porous structure, solution ions need more time to enter/leave the pores. Thus, the full capacitance is best obtained at a lower frequency and for thinner NCS membranes, as the time constant for ion transport during PANi oxidation/reduction is at its lowest.

3.4 Conclusions

Conformal PANi coatings with a controllable thickness have been successfully coated on the nanoporous carbon scaffold materials (NCS), which had pore diameters of either 50 or 85 nm and a typical thickness of 60 - 80 µm. The morphology of the electrodeposited PANi changes with the CV scan rate and the potential window used during its formation, with the optimal conditions being sweep rates of 5 mV/s or lower and a potential window of -0.222 to +0.828 V vs. Ag/AgCl in 3 M NaCl. The as-prepared polyaniline/NCS composites present superior electrochemical properties compared to bare NCS-85, as demonstrated by the much-increased specific capacitance, from 18 F/g for NCS-85 to 389 F/g for PANi-12/NCS-85. The time constant increases from 3 s for NCS-85 to 45 s for PANi-12/NCS-85 after PANi coating, because of the increased barrier for ion transport due to the smaller pores in the modified NCS materials. The capacitance also increases significantly for the PANi-6/NCS-50 compared to the NCS-50 alone (from 22 F/g to 214 F/g). These findings indicate that the presence of a thin, conformal PANi coating on the internal surfaces of the NCS-85 and NCS-50 materials makes them very promising as candidates for supercapacitor and capacitive deionization applications.

3.5 Supplementary Information
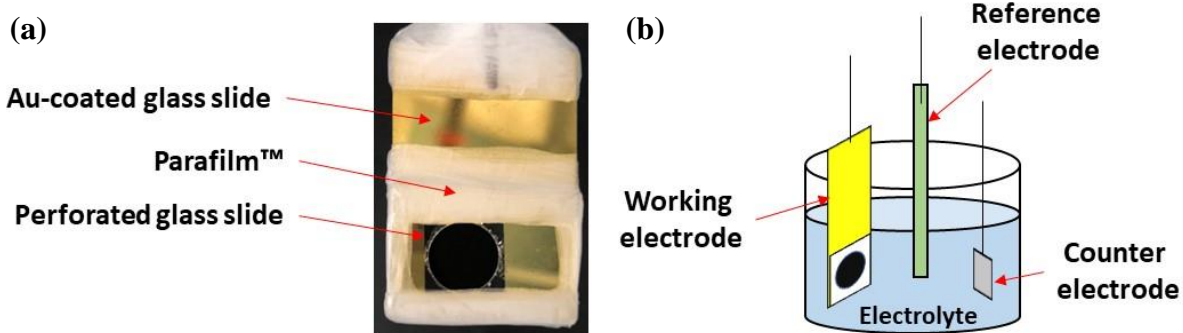
Figure S3.1 (a) Top-view of the working electrode, and (b) the cell configuration used in PANi deposition and electrochemical testing.
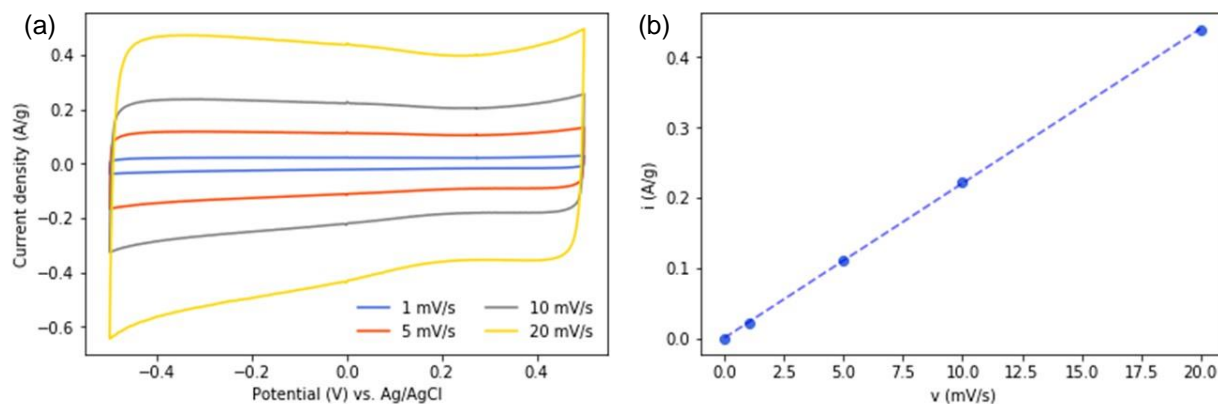
Figure S3.2 (a) Cyclic voltammograms of NCS-50 in N_2-saturated 3 M NaCl solution at various scan rates (1, 5, 10, and 20 mV/s). (b) The relationship of anodic current density at 0 V vs. the scan rate for NCS-50.
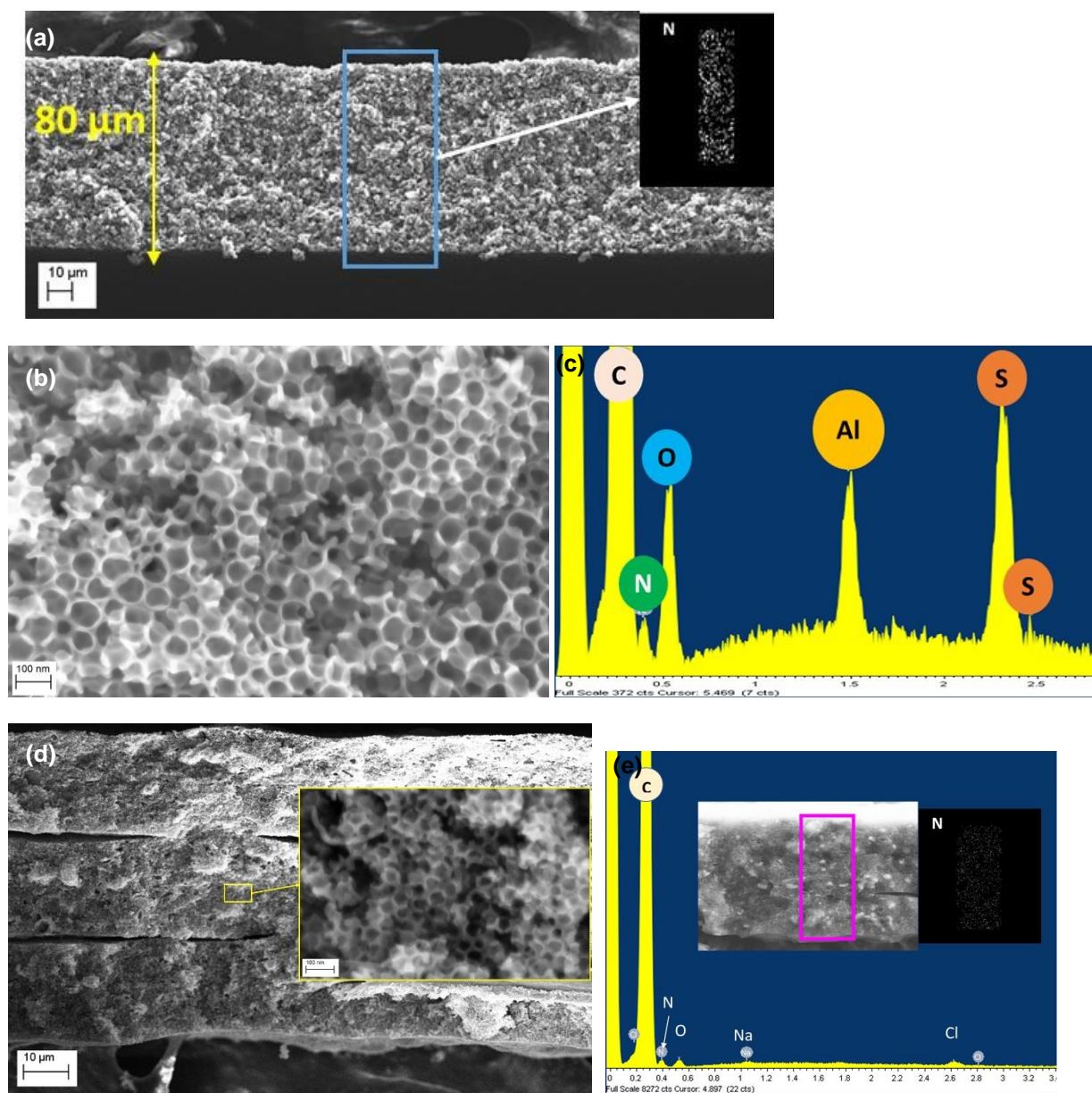
Figure S3.3 (a) Cross-sectional SEM image of PANi-6/NCS-85, where the thickness of the PANi-6/NCS-85 film is roughly 80 μm. The inset image shows an EDX map of the blue rectangular area in the cross-section in (a), showing a uniform distribution of nitrogen across the film. (b) Zoomed-in FESEM image in the middle of the cross-section of the PANi-6/NCS-85 film, while (c) shows the EDX spectrum of the blue rectangular area in the cross-sectional image in (a), verifying the presence of nitrogen throughout the PANi/NCS films. (d) FESEM of the cross-section of PANi-6/NCS-50. The inserted image is a zoomed-in image of the middle of the cross-section of PANi-6/NCS-50. (e) EDX map of the cross-section of PANi-6/NCS-50, where N is again evenly-distributed throughout the film.
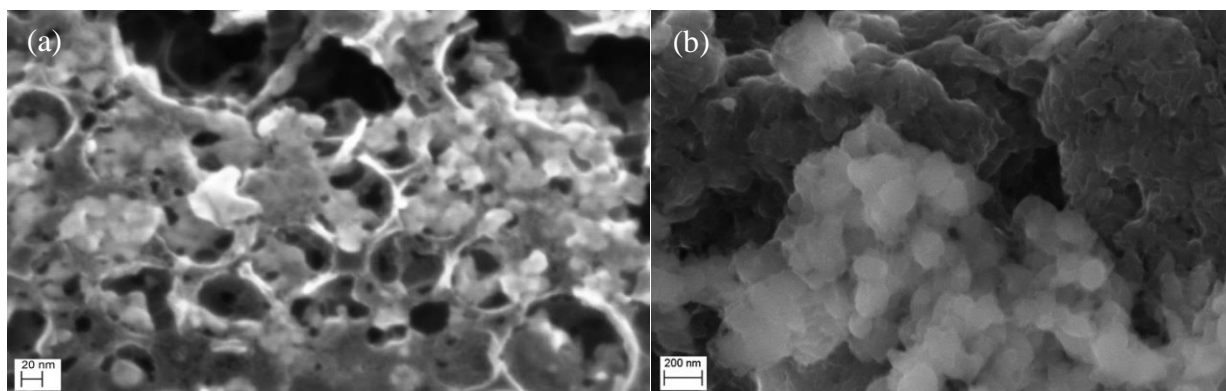
Figure S3.4 FESEM images of the PANi-coated NCS prepared by (a) scanning between -0.222 to 0.828 V at a rate of 50 mV/s for 60 cycles, and (b) scanning between -0.222 to 1.4 V at a rate of 5 mV/s for 1 cycle.
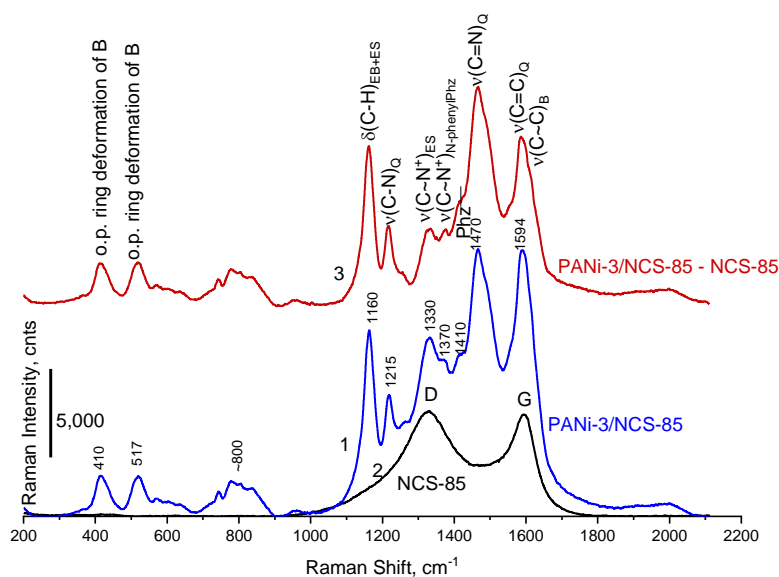
Figure S3.5 Raman spectra of (1) PANi-3/NCS-85, (2) NCS-85 alone, and (3) PANi-3/NCS-85 after subtraction of the spectrum of NCS-85, where ES = emeraldine salt, EB = emeraldine base, B = benzenoid ring, Q = quinonoid ring, Phz = phenazine-like segment, o.p. = out-of-plane, *ν* = the bond stretching, *δ* = the bond bending, and C~N$^{+\cdot}$ = polaron structure. Peak assignment made on the basis of the work of Malinauskas et al and Trchová et al. [111], [113]**.**

The assignment of the PANi peaks in the Raman spectrum was based on Refs [111], [113]. In particular, peaks at 410 and 517 cm^{-1} are assigned to the out-of-plane deformation of the benzenoid (B) ring. The broad structured peak at ca. 810 cm^{-1} is due to the out-of-plane bending of the C-H groups of different rings in PANi. The strong sharp peak at ca. 1160 cm^{-1} is attributed to the in-plane bending vibrations, δ(C-H), of the C-H groups of the emeraldine. An important peak at ca. 1330 cm^{-1} is associated with the C~N$^{\bullet+}$ stretching vibrations of the ES, which is related to the conductivity of PANi. Peaks at 1460-1470 cm^{-1} and ca. 1590 cm^{-1} are assigned to the ν(C=N) and ν(C=C) stretching vibrations of the Q units of emeraldine base (EB), respectively. A shoulder at 1620 cm^{-1} is due to the ν(C-C) stretching vibrations of the benzenoid (reduced) units.

Table S3.1. Elemental Analysis of PANi-6/NCS-85

	Weight %
C	86.3
H	1.8
N	4.2
PANi *	28

*Calculated theoretically based on the nitrogen content. Elemental analysis of PANi-6/NCS-85 gives the content of nitrogen in the composites, which is 4.2 wt.% (Table 1). By assuming all of the nitrogen comes from polyaniline, the theoretical polyaniline content in PANi-6/NCS-85 is calculated to be 28 wt.%.
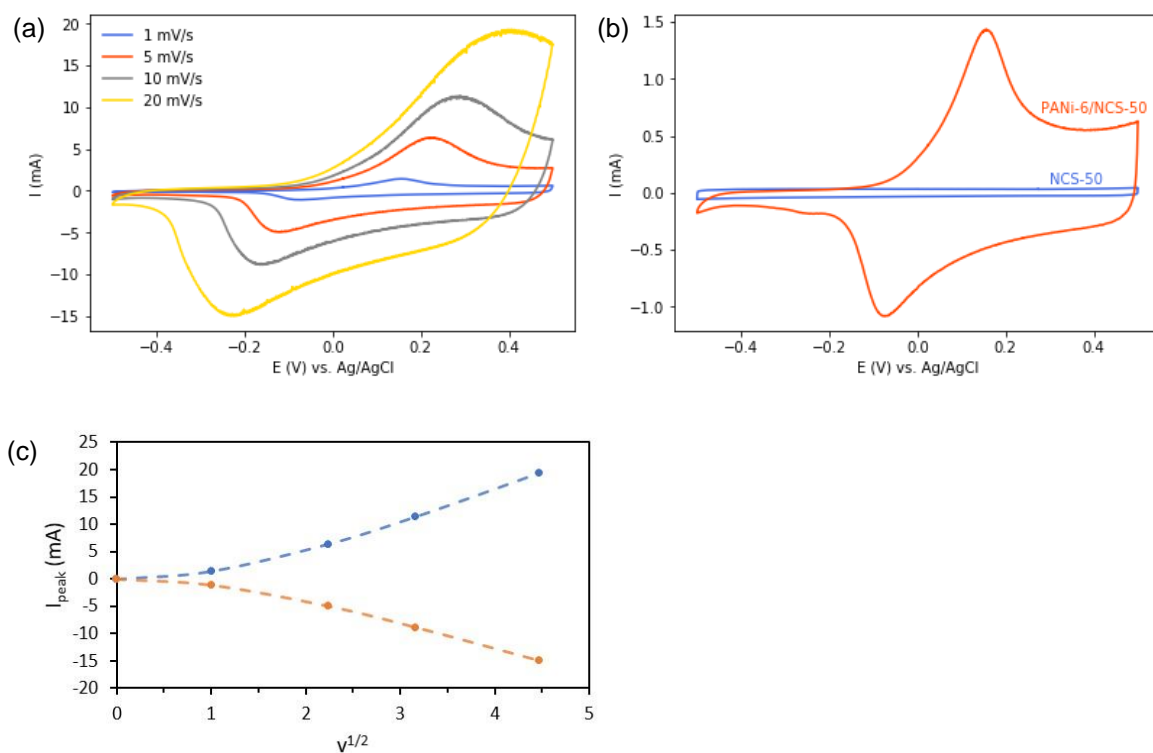
Figure S3.6 CVs of (a) PANi-6/NCS-50 at various sweep rates: 1, 5, 10 and 20 mV/s. The electrolyte was 3 M NaCl, and the potential was scanned between -0.5 and 0.5 V and (b) NCS-50 and PANi-6/NCS-50 at a scan rate of 1 mV/s in the same solution. (c) The relationship between the peak current (I_{peak}) and the square root of the sweep rate ($v^{1/2}$) of PANi-6/NCS-50.
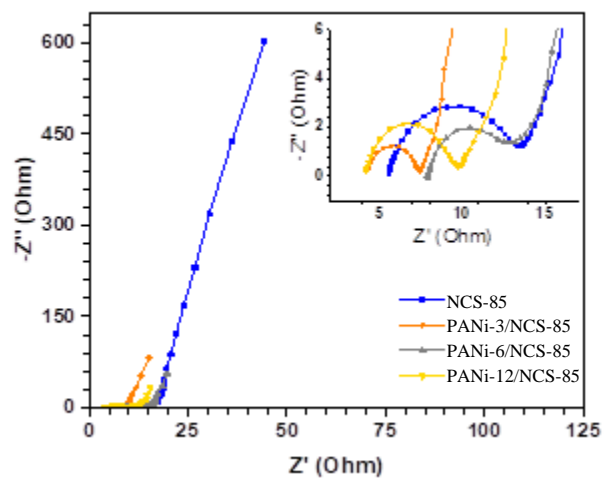
Figure S3.7 EIS response of NCS-85 and PANi/NCS-85 composites, measured at the open circuit potential from 100 kHz to 10 mHz, with an ac amplitude of 10 mV.

<div align="center">

Chapter 4

Highly Ordered PANi/Carbon Composite Membranes for Energy Storage and Combined

Filtration and CDI Applications

</div>

<div align="center">

Chengying Ai[a], Irina V. Chernyshova[c], Erin L. Gawron[a], Viola I. Birss[b], and

Sathish Ponnurangam*[a]

</div>

[a] Department of Chemical and Petroleum Engineering, Schulich School of Engineering, University of Calgary. 2500 University Drive NW, T2N 1N4, Calgary, AB, Canada. E-mail: sathish.ponnurangam@calgary.ca

[b] Department of Chemistry, University of Calgary. 2500 University Drive NW, T2N 1N4, Calgary, AB, Canada. E-mail: birss@ucalgary.ca

[c] Department of Earth and Environmental Engineering, Columbia University, New York, NY, USA. E-mail: ic2228@columbia.edu

Highlights:

- First time use of a self-supported nanoporous carbon scaffold (NCS) as a CDI electrode, without the use of any binders.

- First time that a conformal polyaniline-coated NCS material was used as a CDI electrode.

- Super fast salt adsorption (2 – 10 seconds) of the NCS and the polyaniline-coated NCS, which is 1 to 2 orders of magnitude faster as compared to typical CDI systems reported in the literature.

- First report of CDI cells being used simultaneously for water ultrafiltration.

Abstract

The growing population has significantly boosted the need for sustainable energy and clean water. Electrochemical capacitors have shown promise in both energy storage (supercapacitors) and water treatment (capacitive deionization, CDI). Thus, in this work, a free-standing carbon material, a nanoporous carbon scaffold (NCS), was studied as a capacitive electrode and its energy storage and desalination performances were improved further with a thin, conformal polyaniline (PANi) coating (PANi/NCS). The PANi/NCS materials show a high capacitance (335 F/g) at 1

mA and also exhibit excellent stability, energy density and power density. An asymmetric CDI cell, containing one PANi/NCS composite electrode and one NCS-only electrode, shows a salt adsorption capacity of 2.6 mg/g (0.019 mg/m^2) at an operating voltage of 2 V. The salt removal occurs very quickly (2 – 10 s), which is 1 to 2 orders of magnitude faster compared to other electrode materials reported in literature, due to the low tortuosity of the NCS structure. In addition, due to the unique porous structure of the NCS and PANi/NCS composite, the electrodes could also perform simultaneously as ultrafiltration membranes, as demonstrated by the removal of Au nanoparticles (10 nm in diameter), thus creating a one-step water treatment process.

4.1 Introduction

Producing clean water from a range of sources, such as seawater and brackish water, has become an approach for relieving the world's current water burden [119]. While technologies such as reverse osmosis (RO) and distillation have been able to separate salts from water, high energy consumption and other engineering issues, such as membrane fouling in RO processes, limit their applications and increase their cost [19]. The need for removing solid particles and microorganisms also requires pre-treatment (e.g., filtration, coagulation and membrane separation) and post-treatment (e.g., remineralization, boron/chloride removal and disinfection) to be supplemented with the desalination process, leading to increased process costs for desalination [1]. Therefore, the development of more cost-efficient and effective desalination technologies have attracted significant research interest recently.

Capacitive deionization (CDI) is an emerging technology that has shown promise towards desalination. It features low energy consumption, low cost, environmental-friendliness and easy regeneration compared to established methods, including RO and distillation [51], [53].

Traditional methods are energy-demanding and expensive to set up [4], [11]. In a CDI process, a potential bias is applied between two porous electrodes, forcing oppositely charged salt ions in the feed water to migrate toward each electrode and then storing them at the outer Helmholtz plane (OHP) of the electrical double layers (EDLs) formed at the interface of the electrode and electrolyte [13]. These ions are released by switching to zero-voltage or by reversing the polarity of the cell [120]. The salt ions are stored in the EDLs, which is equivalent to the energy storage process in supercapacitors[14], [15], [121]. Therefore, a CDI cell can store energy while also removing salts, and release the energy to power an electric device during salt desorption [15]. The electrode material and its morphology are key factors that determine the performance of a CDI cell. A good CDI electrode should have a large surface area, sufficiently accessible pores, high conductivity, and stable electrochemical properties [22].

The CDI properties of porous carbon (PC) have been extensively explored, including activated carbon (AC) [48], carbon aerogels [49], carbon nanotubes [50], graphene [122], and their composites [52], [53]. However, PC can exhibit critical limitations, such as low capacitance and an unfavorable porous structure for ion transport that increases the timescale of salt removal [23], [123], [124]. To increase the salt removal performance, electrodes containing redox-active species have become popular in CDI research because of their extended salt adsorption capacity and the possibility of selectively removing ions [28]. The studied redox-active species have included conducting polymers (e.g., polyaniline) and metal oxides (e.g., MnO_2) [31], [125]–[128].

Brackish or sea water not only contains a large amount of dissolved salts, but also solid particles and microorganisms, which cannot be removed by CDI alone. Thus, pre-treatment and post-treatment need to supplement the desalination unit for producing potable or irrigation water, which then increases cost and energy consumption for a water desalination plant [1]. Simplifying

the water treatment processes into fewer steps is desirable because this could cut operation costs and make water production more efficient and cost-effective. As one example, Ye et al. reported the integration of CDI and photocatalysis for brine wastewater treatment, which can remove salt and organic contaminants in one step [76].

Membrane separation, including ultrafiltration (UF) and nanofiltration (NF), is able to remove particulates and biological contaminants (e.g., bacteria, viruses) and proteins from water [129], [130]. Most membranes are made from non-conductive polymers and ceramics, and no one has as yet reported a system that can accomplish UF/NF and CDI simultaneously. Li et al. reported a nanoporous carbon scaffold (NCS) with a tunable porous structure, which has been demonstrated as a NF membrane [77], [131]. Since the NCS is a conductive material, it is promising for use in a concurrent filtration and desalination process.

In our previous work, a conformal polyaniline (PANi) film has been coated on the internal surfaces of the NCS with 50 and 85 nm pores (NCS-50 and NCS-85) [132]. The PANi/NCS composite showed a significantly larger capacitance (by up to 20 times) than the NCS alone, while retaining its fully 3D interconnected nanoporous structure for combined CDI and ultrafiltration [132]. In this work, NCS and the PANi coated NCS (PANi/NCS), reported in our previous work [132], have been studied as CDI electrodes, along with ultrafiltration. The NCS-85, with an 85 nm pore size, was chosen for the present study as its pores allow for a more rapid flow of ions during flow-through CDI and ultrafiltration, compared to NCS-50. The NCS-85 and PANi/NCS-85 materials show good stability, with 100% and 83% capacitance retention after 1000 galvanostatic charge/discharge cycles in 3 M NaCl, respectively [132]. The salt adsorption capacity for an asymmetric CDI cell composed of a PANi-NCS anode and an NCS cathode is 2.6 mg/g, which is higher than for both the symmetric NCS cell (1.4 mg/g) and symmetric PANi-6/NCS-85 cell (0.81

mg/g) at 2 V charging in 10 mM NaCl (580 ppt, brackish water). Moreover, due to the unique nanoporous structure of NCS-85 (85 nm pore size, ~10 nm pore neck) [132], solid particles (~10 nm in size) could be removed by ultrafiltration at the same time using a flow-through CDI cell. This is the first time that CDI cells have been used simultaneously as a filtration membrane, while also deionizing the aqueous solution passed through the membranes.

4.2 Experimental Methods

4.2.1 Preparation of NCS

The NCS film was prepared, based on the method developed by X. Li et al.[77] and a simplified procedure is described here. A carbon ink was made by mixing 0.6 g of mesophase pitch (AR Grade, Mitsubishi Chemicals, Japan), 2.4 grams n-butanol, 9.6 g 15wt% polyvinyl alcohol in water (PVA, Alfa Aesar, 86 – 89 % hydrolyzed, low molecular weight), and 9 g of a colloidal silica suspension (NanoSol-5080S, in this case with an average colloid size of 85 nm). The silica suspension was added to the carbon ink and was ball-milled for 4 h to obtain a slurry. The carbon slurry was held under vacuum for 30 min to remove bubbles and then was cast on a glass substrate using a casting blade with a 0.003-inch (0.0762 mm) gap between the doctor blade and the substrate. After drying, a carbon/silica film was obtained and six such films were then pressed together to form one 6-layer NCS film. The film was then treated by heating at 400 °C for 2 h and then at 900 °C for 2 h in a nitrogen atmosphere. After cooling, the carbonized films were soaked in 3 M NaOH at 80 °C for 2 days to remove the silica template. Following this, the films were rinsed with dilute HCl and deionized water several times. After drying, the NCS-85 film was used as prepared.

4.2.2 Preparation of PANi/NCS-85 composites

Polyaniline (PANi) was deposited on the inner surfaces of NCS by using a potentiodynamic method [74], [132]. Employing a three-electrode cell, the NCS-based working electrode was immersed in a solution containing 0.1 mol·L^{-1} aniline (ACS reagent, SIGMA-ALDRICH) and 1 mol·L^{-1} H$_2$SO$_4$ for 30 min and then scanned between -0.222 to 0.828 V at a sweep rate of 5 mV/s. A Pt gauze was used as the counter electrode and an Ag/AgCl reference electrode (RE-5B, BASi) was used as the reference electrode. All potentials given in this paper are referenced to Ag/AgCl. A potentiostat (Solartron Analytical 1480 MultiStat) was used to control the electrochemical polymerization and measurements. PANi/NCS-85 composites, prepared by using 3, 6, and 12 cyclic voltammetry (CV) cycles, were named as PANi-3/NCS-85, PANi-6/NCS-85 and PANi-12/NCS-85, respectively.

4.2.3 Electrochemical characterization

All electrochemical tests were carried out in a three-electrode cell containing 3 M NaCl. The galvanostatic charge/discharge (GCD) measurements were conducted at several currents: 1, 2, 5, 10, and 20 mA, in a voltage range between -0.5 V and 0.5 V vs. Ag/AgCl where no oxygen or hydrogen evolution reactions occur. The specific capacitance (C_{sp}) was calculated using the equation below [53]:

$$C_{sp} = \frac{I\Delta t}{\Delta V \cdot m} \tag{1}$$

where C_{sp} is the specific capacitance (F/g), I is the applied discharge current (A), Δt is the discharge time (s), ΔV is the potential change during discharge (V) and m is the total electrode weight in grams.

The energy density and power density of the studied materials (e.g. NCS-85 and PANi/NCS-85) were calculated from the GCD data by eq. (2) and (3) [133]:

$$U = \frac{\frac{1}{2}C_{sp}\Delta V^2}{3.6} \qquad (2)$$

$$P = \frac{3600U}{\Delta t} \qquad (3)$$

where U and P are the specific energy density (Wh/kg) and the specific power density (W/kg), respectively.

4.2.4 Physical characterization

Operando Raman spectra were collected in an Ar-saturated 3 M NaCl solution (pH of ca. 7) in an in-house, one-compartment, 3-electrode spectroelectrochemical cell (Figure S1a). The working electrode was prepared by sandwiching a flake of the PANi/NCS-85 (ca. 1 x 3 mm^2 in size) between the folds of a folded Pt foil (Figure S4.1 (b)). A Pt-Ir foil was used as a counter electrode and an Ag/AgCl electrode (RE-5B, BASi) was used as the reference electrode. A Metrohm potentiostat (PGSTAT128N), controlled by NOVA 1.10.4 software, was used in this experiment. The spectroelectrochemical cell was made from high-density polyethylene and was placed under an UPlanApo/IR 60X objective. Each spectrum was collected at a 5 s exposure and 10 accumulations (50 s total) after the cell current had stabilized (after ca. 1-2 min).

4.2.5 Capacitive deionization testing

The CDI cell schematic is shown in Fig. S4.2. The CDI cell consisted of polycarbonate covers, which were 3D printed, gaskets (McMASTER-CARR), carbon fiber paper (Avcarb 280)

as the current collector, glass paper as the separator, and the porous carbon electrodes, including NCS-85 and PANi/NCS-85. The electrodes were 2 cm $\times$ 2.5 cm (80 μm thick). CDI operation was single-pass flow-through. A water reservoir, containing 1 L of 10 mM NaCl as the feed, was pumped into the cell at a rate of 1.5 mL/min. The conductivity of the effluent was measured by using a conductivity meter (SevenCompact^{TM} Duo S213, with an InLab® 731-ISM probe, METTLER TOLEDO). The CDI cell was charged at a constant voltage and was then discharged at zero voltage.

The salt adsorption capacity (Γ, mg/g) was calculated by [134]:

$$\Gamma = K\phi \int (\sigma(t) - \sigma_0)dt , K = M/(km) \tag{4}$$

where K is the calibration coefficient collected from measuring the conductivity of a set of NaCl solutions with known concentrations, M is the molecular weight of the salt (mg/mmol), k is the slope of the calibration curve (μS cm^{-1} mM^{-1}), and m is the total weight of the electrodes (g). Φ is the flow rate (L/min), σ is the conductivity of the effluent (μS cm^{-1}), σ_0 is the initial conductivity of the solution (μS cm^{-1}), and t is the charging time (min).

An average salt adsorption rate (SAR) can be calculated by simply dividing Γ (mg/g) by the adsorption time (t_{ad}, min) [13],

$$SAR = \frac{\Gamma}{t_{ad}} \tag{5}$$

The charge efficiency (Λ) [13] is calculated by

$$\Lambda = \frac{\Gamma/M}{\Sigma/F} \tag{6}$$

where M is the molecular weight of the salt in g/mol, Σ is the electric charge passed through the cell during the adsorption process (mC/g electrodes), and F is the Faraday constant, which is 96485 C/mol.

The combined CDI and ultrafiltration (UF) experiments were carried out using the same cell. The feed water in this experiment was 10 mM NaCl containing suspended Au nanoparticles (~ 10 nm in size) and the effluent was collected in a vial.

4.3 Results and Discussion

In our previous work, it was shown that ultrathin and conformal PANi layers can be deposited on the full inner surface of the NCS and characterized [132]. The PANi coatings have a thickness ranging from 3 to 20 nm and the as-prepared PANi/NCS composites retain their interconnected nanoporous structure (Fig. 4.1b-d). The electrochemical performances of the NCS-85 and the PANi/NCS-85 composite were also demonstrated by cyclic voltammetry (CV) and electrochemical impedance spectrometry (EIS) (Fig. 4.1) [132]. The gravimetric capacitance calculated from the CVs increased significantly after PANi coating, from 17 F/g for NCS-85 to 390 F/g for PANi-12/NCS-85, which was attributed to the pseudo-capacitance arising from PANi redox reactions (Fig. 4.1a) [132].

NCS-85 shows favorable electrical double layer (EDL) behavior as its CV has a rectangular shape (Fig. 4.1a: blue line). In contrast, two broad peaks are present in the CVs of the PANi/NCS composites. When using PANi-12/NCS-85 as an example (Fig. 4.1a: yellow line), the peak at 0.15 V vs. Ag/AgCl is related to the oxidation of the PANi film, from leucoemeraldine (LE) to emeraldine salt (ES), and finally to pernigraniline (PE), while the peak at ca. -0.1 V vs. Ag/AgCl is related to the reduction of PANi, from PE to ES and ES to LE [117], [132].
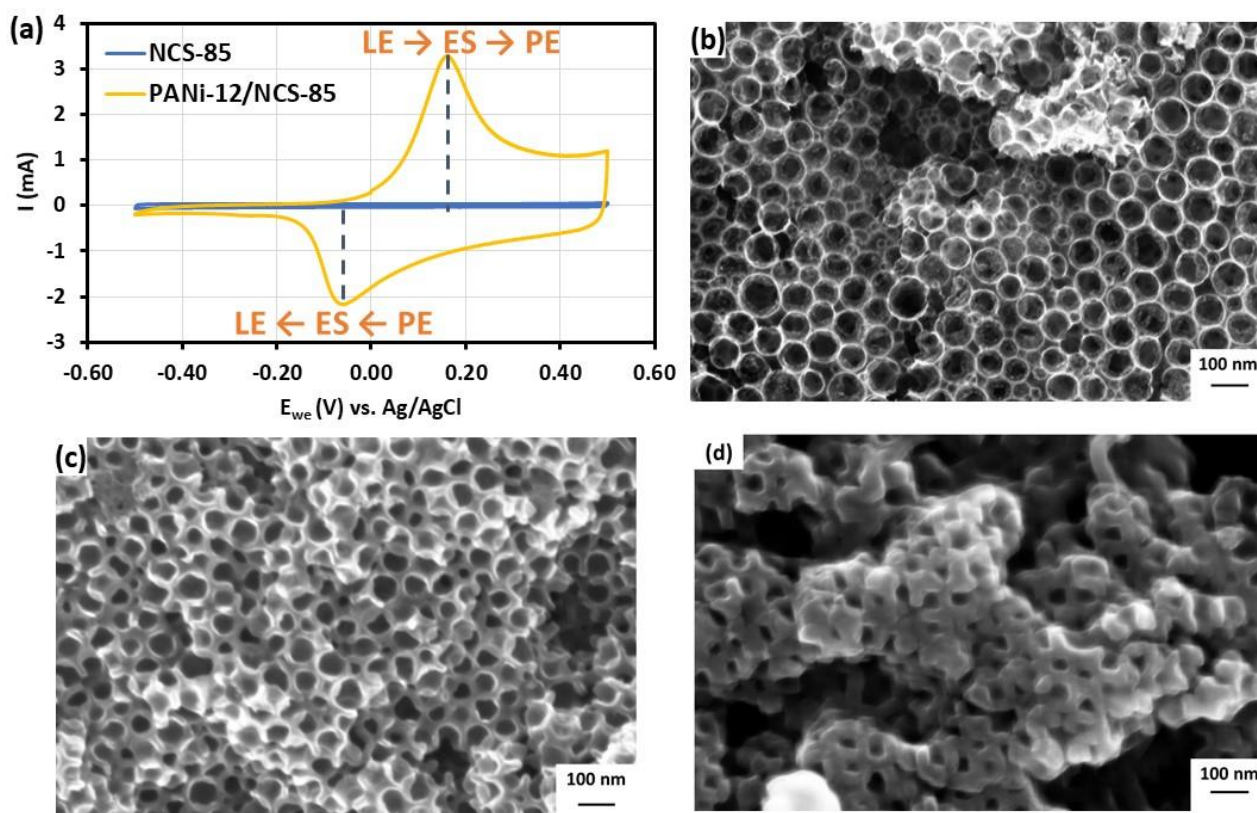
Figure 4.1 (a) CVs of NCS-85 and the PANi-6/NCS-85 at 1 mV/s in 3 M NaCl, and the SEM images of (b) the NCS-85 material, (c) the PANi-6/NCS-85, and the PANi-12/NCS-85 composite (scale bar 100 nm).

4.3.1 Energy storage by NCS-85 and PANi/NCS-85 materials

Further studies of the energy storage capabilities of NCS and PANi/NCS were conducted with galvanostatic charge/discharge (GCD) over a potential range between -0.5 and 0.5 V vs. Ag/AgCl in 3 M NaCl (Figs. 4.2a and S4.3 (a-d)). NCS-85 shows a triangular GCD result at different applied currents (Fig. S4.3 (a)), indicating its good EDL behavior. In contrast, the GCD curves of the PANi/NCS-85 composites show a shoulder at around 0.1 V, as shown in Fig. 4.2a and Fig. S4.3 (b-d), which is due to the presence of the redox reactions of PANi [132].

The specific capacitance (C_{sp}), calculated from the GCD data using eq. (1), is summarized in Table S4.1. At a discharge current of 1 mA, PANi-3/NCS-85, PANi-6/NCS-85 and PANi-12/NCS-85 give C_{sp} values of 94 F/g, 144 F/g and 337 F/g, respectively, which are more than 5 times the C_{sp} values of NCS-85 alone (19 F/g). The increase in C_{sp} corresponds to the additional pseudo-capacitance contributed by the PANi film. An increased C_{sp} is generally associated with improved capacitive behavior [135].

The C_{sp} decreases with higher charging currents (Fig. S4.3 (e)), which can be attributed to some limitations in the diffusion of ions into the porous structure of NCS-85 at high charging currents. However, even at 20 mA, the C_{sp} of the PANi/NCS-85 composites (49 – 229 F/g) is still much higher than the bare NCS-85 (6 F/g), indicating good capacitor performance over the range of currents tested (Table S4.1).

Figure 4.2a shows the GCD profile of NCS-85, PANi-3/NCS-85, PANi-6/NCS-85 and PANi-12 /NCS-85 at a current of 1 mA. As can be seen, curves broaden as the PANi coating thickens, which is related to the increased C_{sp} (Fig. 4.2b, Table S4.1) and the associated longer discharge times (eq. (1)). A sudden potential drop at the start of discharge can be observed for the tested samples (Fig. S4.4), which is due to the IR drop. This is caused by the internal resistance (ESR) of the cell, including the solution resistance and possibly some material resistance [54], [135], [136]. The ESR value can be found by plotting the IR drop vs. the applied current. As seen in Fig. 4.2c, the IR drop is linearly correlated with the applied current and the slope is equal to the ESR (Table S4.2) [87]. The ESR is an indicator of the power performance of a compact supercapacitor [87], [136], but in this work, since the GCD tests were conducted in a three-electrode system, the change in position between the working and reference electrodes could also contribute to the differences seen in the ESR values.
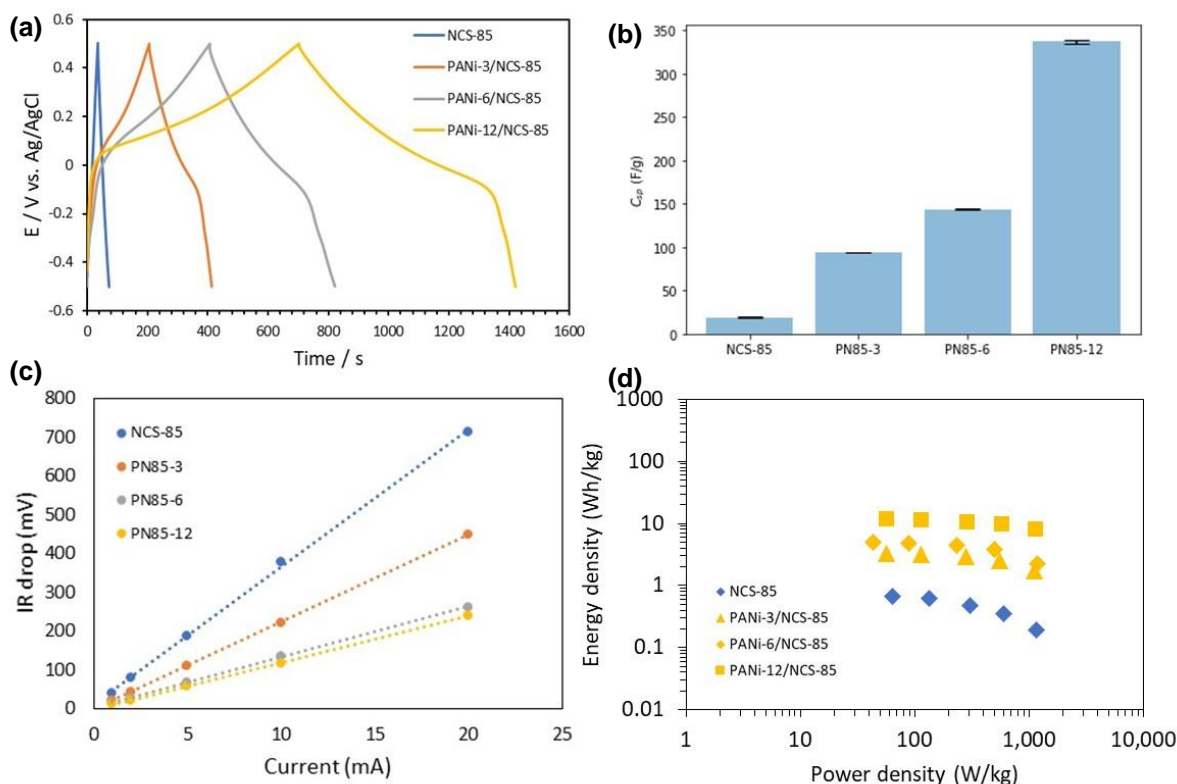
Figure 4.2 (a) GCD profile of NCS-85, PANi-3/NCS-85, PANi-6/NCS-85 and PANi-12/NCS-85 at a current density of 1 mA over a potential range from -0.5 V to 0.5 V vs. Ag/AgCl in 3 M NaCl. (b) Specific capacitance at 1 mA for all samples including error bars. (c) The relationship between the IR drop and the applied current for NCS-85 and the PANi/NCS-85 composites. (d) Ragone plots of energy density vs. power density for NCS-85 and PANi/NCS-85.

The power density (P) and energy density (U) were also calculated from the GCD data using eq. (2, 3) and are listed in Table S4.2. The U value for NCS-85 (1 - 3 Wh/kg) is slightly lower than commercial activated carbon (4 - 5 Wh/kg) [88]. This may be because activated carbon has a higher specific surface area (1000 – 3500 m^2/g) compared to NCS-85 (~145 m^2/g), although the NCS-85 has much larger pores and an organized porous structure, allowing more of the internal surfaces to be involved in the capacitive process [13], [132]. The PANi/NCS-85 shows a significant increase in U, up to 47 Wh/kg, as compared to the bare NCS-85. An increase in U

usually leads to a loss in P in the same material (Fig. 4.2d), which means slower electron transport and ion transport. However, the PANi/NCS-85 composites have shown a comparable power density compared to the NCS-85 alone (Fig. 4.2d), which can be attributed to their excellent interconnected three-dimensional porous structure [77].

4.3.2 Cyclic stabilities of NCS and PANi/NCS

The cyclic stabilities of PANi-6/NCS-85 and NCS-85 were tested using GCD at 2 mA for 1000 cycles in 3 M NaCl (Fig. S4.5). NCS-85 retained its triangular GCD shape after 1000 cycles, while in the last three cycles for PANi-6/NCS-85, it is noteworthy that the shoulder at 0.2 V and - 0.1 V disappeared. The capacitance of NCS-85 remained at 100 % after 1000 GCD cycles, while the capacitance of PANi-6/NCS-85 was 83 % of its original value after 1000 cycles. The C_{sp} of PANi-6/NCS-85 dropped sharply in the first 100 cycles and steadily decreased afterwards, as shown in Fig. 4.3a. Although PANi-6/NCS-85 lost around 20 % of its original C_{sp}, its specific capacitance of 128 F/g is still significantly higher than seen for NCS-85 (18 F/g).

CV measurements were conducted with PANi-6/NCS-85 after 1000 GCD cycles, as shown in Fig. 4.3b. A decrease in the redox peaks of PANi are seen at around 0.15 V and -0.1 V vs. Ag/AgCl, which may suggest that irreversible oxidation or hydrolysis of PANi occurred during GCD cycling. The disappearance of the shoulder at around 0.1 V vs. Ag/AgCl in the last three GCD cycles (Fig. S4.5 (a)) also indicates the loss of some of the PANi redox activity. Wang et al. has reported a 74 % C_{sp} retention of a PANi-coated carbon black material after 300 cycles and stated that PANi hydrolysis and associated structural changes likely caused the capacitance to decrease [137].
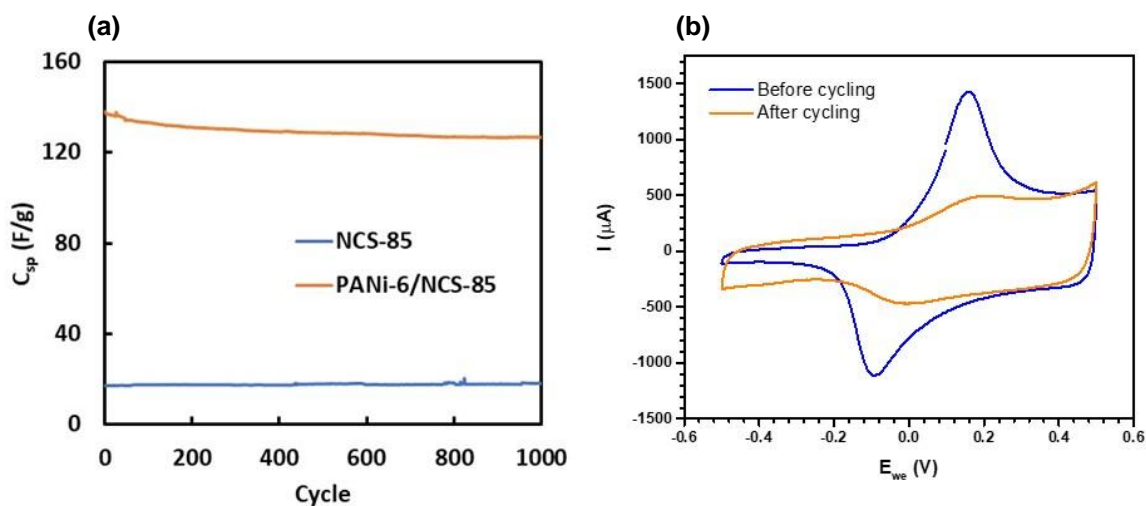
Figure 4.3 (a) Specific capacitance of PANi-6/NCS-85 and NCS-85 after 1000 GCD cycles. (b) CVs of PANi-6/NCS-85 before and after 1000 cycles.

The morphology of the PANi-6/NCS-85 sample after 1000 GCD cycles was characterized using SEM (Fig. S4.6), showing no obvious changes or loss of thickness in the PANi film as compared with the sample before GCD cycling (Fig. 4.1c). Since there was no loss of the PANi coating, some change in the PANi morphology or composition, associated with a change in the PANi redox chemistry, is a more likely cause for the decrease of C_{sp}.

4.3.3 Structural analysis of PANi-6/NCS-85 composites using operando Raman spectroscopy

The proposed structural changes of PANi during electrical charge/discharge of the PANi/NCS composites were studied by operando Raman spectroscopy in Ar-saturated 3M NaCl (Fig. 4.4a). The thorough assignment of the Raman features of PANi-containing materials can be found in the literature and in our previous work [111], [113], [132], [138]–[140]. When the electrode potential was scanned from +0.5 V (Ag/AgCl) in the cathodic direction, the intensity of

82

the peak at 1490 cm^{-1} decreased and shifted to 1468 cm^{-1}, indicating the weakening and decrease

of the C=N double bonds due to the reduction of PANi. The peaks at 1595 cm^{-1} and 1221 cm^{-1}

decreased in intensity, which could be attributed to a transformation from the quinonoid dominated

structure to a structure containing more benzenoid units [113]. The red shift of the 1160 cm^{-1} peak

to ~1175 cm^{-1} and the loss in peak intensity also suggest that the quinonoid or semi-quinonoid

units in the PANi film were reduced to benzenoid units [140]. These transformations seem to have

occurred most markedly between +0.1 and -0.3 V, which is in agreement with the reduction peak

seen in the CVs and the GCD profile of PANi-6/NCS-85 (Figs. 4.1a and 4.2b). The presence of

the phenazine (Phz) related peaks at 1406 cm^{-1} suggests oxidative damage to the PANi film after

GCD cycling, which may have been caused by long times (3 min) in an oxidized state at +0.5 V

[139].

The redox/structural stability of the PANi-6/NCS-85 electrode was also examined, using

potential scan data and the Raman spectra discussed above. The Raman spectra of the composite

electrodes were recorded after holding at potentials from +0.5 V to -0.5 V (0.2 V intervals held for

3 min each). As seen from Figure 4.4b, the Raman spectrum of the PANi film, recorded at +0.5 V

after the potential stepping, indicates that some degradation occurred as compared to what is seen

in the initial spectrum at +0.5 V. The increase of the δ(C-H)$_Q$, ν(C-N)$_Q$, and ν(C=N)$_Q$ peaks

indicates a redox state closer to that of pernigraniline (PE) for the PANi films after potential

stepping. The peaks at ~1400 cm^{-1} were assigned to phenazine-like structures due to PANi

degradation [138], [141]. This finding implies that the PANi film became more resistive due to a

loss of conjugation, which also affects the protonation of the polymer. The loss of conjugation and

protonation explains the decrease of the polaron related peak at ~1330 cm^{-1}. This is also consistent

with the loss in electrical capacitance from the PANi/NCS composite after 1000 GCD cycles.
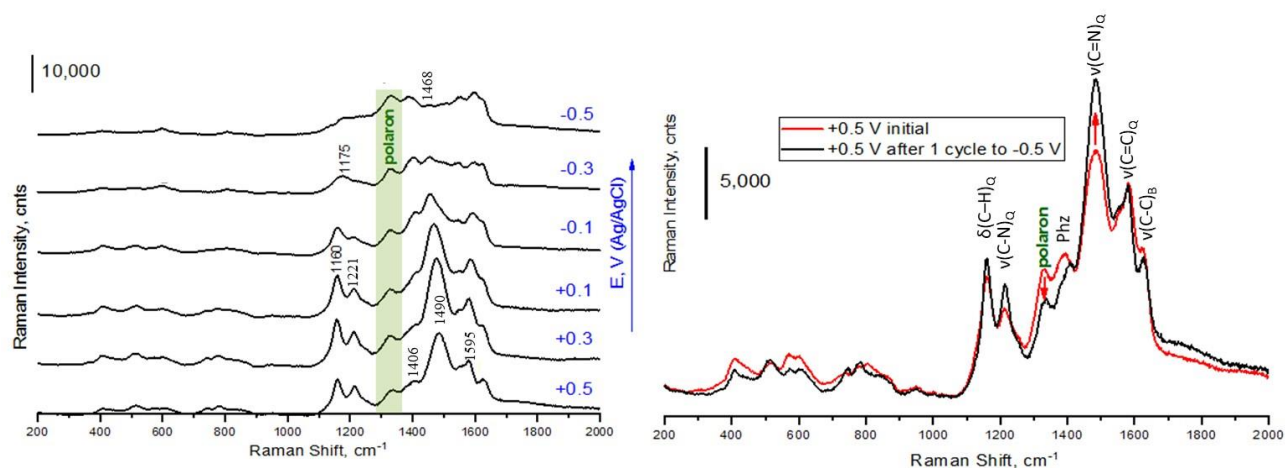
Figure 4.4 Operando Raman spectra of PANi-6/NCS-85, measured in Ar-saturated 3M NaCl (a) at potentials from +0.5 to −0.5 V (Ag/AgCl) and (b) at +0.5 V (red) equilibrated for 30 min and (black) measured after a step-wise increase of potential in the reverse direction (from −0.5 to +0.5 V). Arrows in (b) show that the polaron peak at 1330 cm^{-1} decreases and the $v(C=N)_Q$ peak at 1490 cm^{-1} increases after a chronoamperometry cycle. All of the spectra are presented after subtraction of the spectrum of the NCS-85 material alone.

4.3.4 CDI performance of NCS-85 and PANi-6/NCS-85 composite

The evaluation of the CDI performance was carried out in a flow-through cell (Fig. S4.2) using both symmetric and asymmetric cell configurations. Figure 4.5a shows the typical current response during CDI operation at constant voltage charging (1 V) and zero-voltage discharge. As soon as 1 V was applied between the two NCS-85 electrodes in the symmetric CDI cell, the current increased rapidly, seen as a spike in Fig. 4.5a, and then dropped to almost zero. During this process, salt ions migrate to the two electrode/solution interfaces and are stored in the EDLs. When the potential is switched to zero, salt ions are released into the bulk solution and a reverse current passes (Fig. 4.5a). The electric charge passed in the 5-minute salt releasing step (negative current in Fig. 4.5a) is 7% of that passed in the 5-minute salt adsorption step (positive current in Fig. 4.5a). The charge in the 5-min salt adsorption process is much larger as compared to the desorption process because the charging step was carried out for too long a time (the NCS-85 electrodes had

been completely charged in only 10 seconds, and thus the remaining charge was taken up by Faradaic reactions (e.g., oxygen evolution). This is consistent with the fact that the charging current had dropped by 90% in the first 10 seconds of constant voltage operation, as seen in Fig 4.5a, indicating that the EDL was fully charged in only 10 seconds. The electric charge passed in the first 10 second of salt adsorption process is ~1.5-fold of that in the desorption step, which should be related almost exclusively to double layer discharge, also demonstrating that the EDL of the NCS-85 electrode was fully charged in the first 10 seconds.

The conductivity of the effluent in the single-pass CDI experiment decreased as soon as the potential was applied to the electrodes (Figs. 4.5b and S4.7) Later on, the effluent conductivity increased back to its initial value (Figs 4.4b and S4.7). This is because the concentration of the feed water was kept constant (10 mM) and, when the maximum salt storage of the cell was reached, the concentration of the solution should increase back to the initial feed solution concentration.

The current response indicates that salt removal occurs in the first 2-10 seconds (Fig. 4.5a), while the corresponding conductivity response lasted for 30 – 50 seconds, which could be due to the residence time of the system. This charging time is much faster compared to what has been reported for most of the CDI systems in the literature, which is usually 20 – 60 minutes [142]–[144]. The excellent charge/discharge kinetics in the present work may be attributed to the organized (low tortuosity) porous structure of NCS-85, which greatly facilitates ion transport in and out of the pores. The fast charging can also be attributed to the relatively low surface area of the NCS-85 and the PANi-coated NCS-85 (138 – 145 m^2/g), as compared to other carbon materials (400 – 2000 m^2/g) typically used in CDI [26], [35]. However, these high surface area electrodes, which contain very small pores and significant tortuosity (between carbon particles), will also be

much slower charge/discharge, thus making the CDI process much slower than what is observed

in our work with the NCS-based electrodes, with their larger and ordered pore structure.
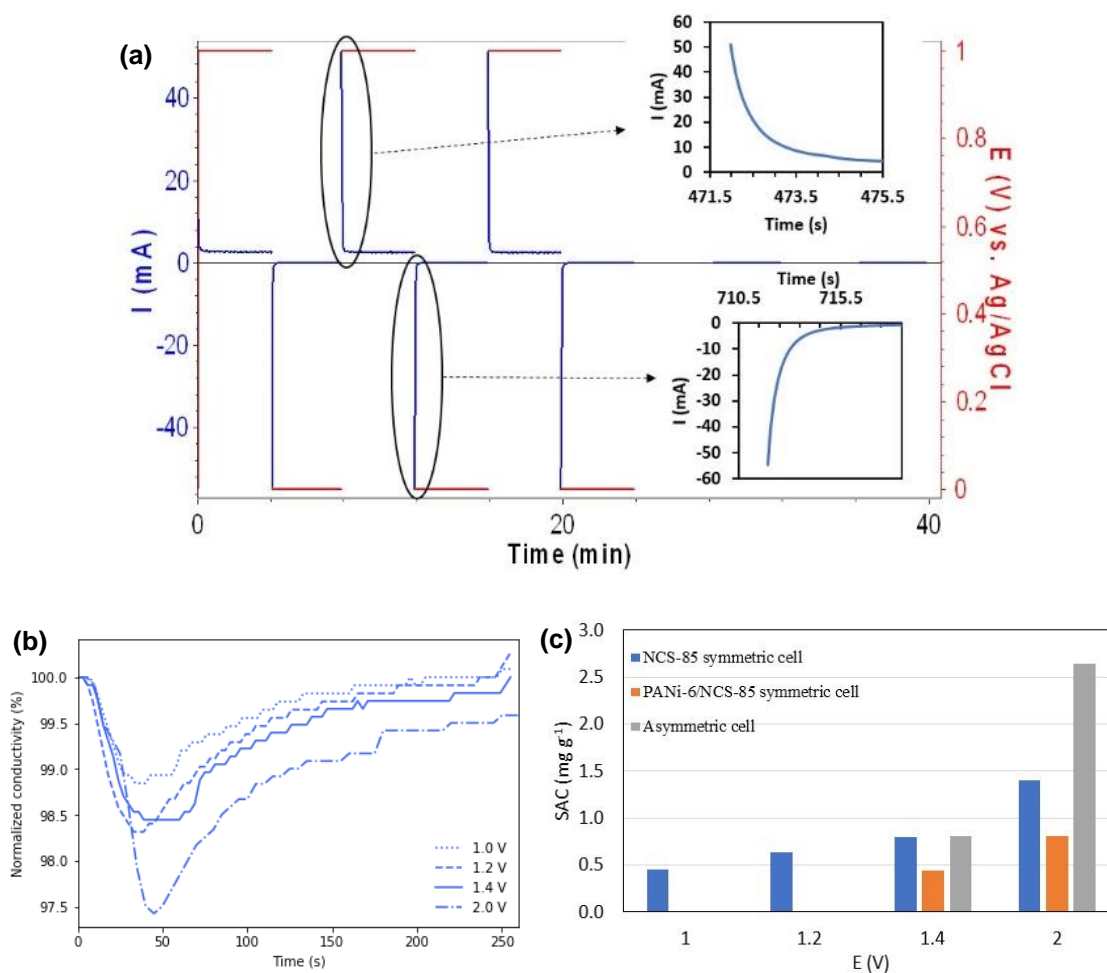
Figure 4.5 (a) Current change (blue) measured during 1 V charge and zero-voltage discharge in 10 mM NaCl using a symmetric NCS-85 based CDI cell. (b) Normalized conductivity of the same symmetric NCS-85 CDI cell at various operating voltages from 1.0 V to 2.0 V. (c) salt adsorption capacity of three cell configurations: NCS-85 symmetric cell with NCS-85 on each side (blue), PANi-6/NCS-85 symmetric cell (PANi-6/NCS-85 at both electrodes, orange), and an asymmetric cell composed of a PANi-6/NCS-85 anode and an NCS-85 cathode (gray), under various operation voltages.

4.3.4.1 Salt removal performance of CDI cells

The salt removal capacity, or salt adsorption capacity (Γ), was calculated from the conductivity results in Fig. 4.5b, using eq. (4) and is plotted in Fig. 4.5c, noting that the use of the word "adsorption" is based on common usage in this field, even though the ions are not adsorbed at the electrode, but rather make up the solution side of the electrical double layer (EDL). Γ is found to increase with increasing applied potential for the same cell. For the NCS-85 electrodes, the salt adsorption capacity is linearly proportional to the operating cell potential. At 2 V charge, the NCS-85 based CDI cell has a salt adsorption capacity of 1.4 mg/g (0.010 mg/m^2).

Surprisingly, even though the PANi-6/NCS-85 material has a much larger capacitance compared to NCS-85, Γ of the PANi-6/NCS-85 symmetric cell is lower than for the NCS-85 symmetric cell, which is only 0.81 mg/g at 2 V (Fig. 4.5c). An asymmetric set up, using PANi-6/NCS-85 as the anode and NCS-85 as the cathode, exhibited the highest Γ among all of the cells tested in this work, at 2.6 mg/g (0.019 mg/m^2). Although PANi-6/NCS-85 has a much higher electrochemical capacitance (145 F/g) compared to the NCS-85 (19 F/g), the PANi-6/NCS-85 symmetric cell shows a smaller salt removal capacity than the NCS-85 symmetric cell. This may be caused by the redox reactions of the PANi-6/NCS-85 anode and cathode. To be specific, while PANi at the anode is taking in anions (Cl$^-$), PANi at the cathode is releasing anions at the same time, leading to less net salt removal. These peculiar results may be due to the uncontrolled potential of each electrode, thus possibly driving the electrodes into a potential range where their full capacitance cannot be accessed. This is discussed in more detail in Section 4.3.4.2 below.

Yan et al. reported a PANi-modified activated carbon for CDI which exhibited a salt adsorption capacity that increased from 1.98 mg/g (0.0014 mg/m^2) for activated carbon to 3.15 mg/g (0.0051 mg/m^2) for the PANi/activated carbon composite, when treating a 250 mg/L NaCl

at a 1.2 V operating voltage [143]. The specific surface area of activated carbon reported by Yan et al was around 10 times that for the NCS-85 in this work, while its salt adsorption capacity is only 3 times the NCS-85 CDI cell. This is likely due to the more accessible porous structure of the NCS-85.

4.3.4.2 Kinetics, efficiency and energy consumption of the CDI cells

The salt adsorption rate (SAR) and charge efficiency (Λ) of the three tested cells from Fig. 4.5 were calculated from eqs. (5) and (6), respectively, and are summarized in Table 4.1. Since the charging step was very fast, as shown in Fig. 4.5a, we use 10 s as the charging time for the calculation of SAR and Λ. As can be seen in Table 4.1, the SAR increases with the applied voltage. The asymmetric cell has the largest SAR, as well as the highest charge efficiency, which is 16 mg g^{-1} min^{-1} (0.27 mg g^{-1} s^{-1}) and ~90% at 2 V. The charge efficiency of the NCS-85 symmetric cell increases from a cell voltage of 1 V to 1.4 V and decreases after that, likely due to the increasingly dominant Faradaic reactions at a cell voltage higher than 1.4 V. Similarly, the PANi-6/NCS-85 symmetric cell and the asymmetric cell exhibit a lower charge efficiency at 2 V (Table 4.1), which may also be due to the increase of Faradaic reactions.

The smaller average salt adsorption rate for the NCS-85 symmetric cell and the PANi-6/NCS-85 symmetric cell is due to their relatively lower salt removal capacity (Section 4.3.4.1). The charge efficiency of the PANi-6/NCS-85 symmetric cell is lower than the asymmetric cell, which can also be attributed to the relatively smaller salt removal capacity of the PANi-6/NCS-85 symmetric cell, according to eq. (6). The total electric charge passed by the NCS-85 and PANi-6/NCS-85 electrodes, integrated in the GCD plots ($Q = I \times t$, Fig. 4.2a), is 36 mC/cm^2 and 407 mC/cm^2, respectively. The first 10-second charge in the salt adsorption step for the NCS-85

electrode in the NCS-85 symmetric cell is 40 mC/cm^2 at 2 V. This indicates that some Faradaic reactions have occurred immediately after the 2 V was applied to the NCS-85 symmetric cell.

In terms of the PANi-6/NCS-85 electrode, the first 10-second charge at 2 V is 15 mC/cm^2 for the symmetric cell and 23 mC/cm^2 for the asymmetric cell, which only accounts for 4% and 5% of the full capacitance charge of the PANi-6/NCS-85 electrode obtained from the GCD plot. This can probably be explained by the uncontrolled potential distribution of the applied potential, where the entire capacitance for the PANi-6/NCS-85 was not accessed during CDI process as the anode potential did not extend sufficiently positive into the PANi electrochemistry (Fig. 3.7a).

Table 4.1 The salt adsorption rate (SAR), and charge efficiency (Λ) values of three CDI cell configurations: NCS-85 symmetric cell, PANi-6/NCS-85 symmetric cell, and asymmetric cell composed of a PANi-6/NCS-85 anode and an NCS-85 cathode.

E	SAR (mg g^{-1} min^{-1})[i]			Λ (%)[i]		
(V)	NCS-85	PANi-6/NCS-85	Asymmetric cell	NCS-85	PANi-6/NCS-85	Asymmetric cell
1	2.7	N/C*	N/C*	23.6	N/C*	N/C*
1.2	3.8	N/C*	N/C*	24.5	N/C*	N/C*
1.4	4.8	2.6	4.9	24.5	59.1	90.5
2	8.4	4.9	16	22.9	46.4	89.0

*Undetectable conductivity changes under these conditions.
[i]The charging time is 10 s.

The energy consumed to reduce the salinity by 1% in 10 mM NaCl for the three different cell configurations is given in Table S4.3. The estimated energy consumption for the asymmetric CDI cell in this work to produce fresh water from brackish water is 0.15 – 1.5 kWh/m^3, which is lower compared to reverse osmosis (0.7~7.7 kWh/m^3) [20] and electrodialysis (~2.03 kWh/m^3)

[145]. The minimum energy required (thermodynamic minimum) for separating ions from brackish water is reported to be 0.12 kWh/m^3 [146]. The minimum energy consumption for the asymmetric CDI cell in this work (0.15 kWh/m^3) is thus very close to the thermodynamic minimum, indicating the very high energy efficiency of the NCS and PANi/NCS based CDI cell. The energy consumption of the CDI cells containing PANi-6/NCS-85, either symmetric or asymmetric, is lower than for cells composed of NCS-85 electrodes alone, which indicates a better energy efficiency of the PANi-6/NCS-85 based cells.

4.3.5 Combination of CDI and ultrafiltration (CDI-UF) using PANi-NCS electrodes

The CDI-UF experiment was carried out in the asymmetric CDI cell, using a PANi-6/NCS-85 anode and an NCS-85 cathode. A salt solution (10 mM NaCl) containing Au nanoparticles (~10 nm, Fig. 6a) was fed into the cell at 1.5 mL/min, and the cell was charged at 2 V for 5 min and then discharged at zero voltage for 5 min. The reason for choosing the asymmetric cell is that this cell was shown above to exhibit the best 2 V CDI performance of all of the cell configurations tested. The other reason is that PANi-coated NCS has a smaller pore neck (11 ± 1.7 nm) [132], which should be able to remove the 10 nm Au nanoparticles.

As shown in Fig. 4.6b, the feed solution has a reddish tint color, which is due to the presence of the Au nanoparticles, while the effluent is transparent, indicating the removal of the Au nanoparticles from the initial liquid feed. The particle size distribution was evaluated using a zeta/nano particle analyzer (NanoPlus HD). As shown in Fig. 4.6c, while there is a peak at around 2 nm for the feed solution, no peak was seen from 1 to 100 nm for the filtered water. The particle size of the Au nanoparticles in the feed water, obtained from the particle analyzer is ≤ 10 nm, which could be due to instrumental error. The NCS-85 material has a pore neck of 13 ± 2 nm,

90

which was reported previously [77], [132]. For NCS-85 alone, the Au nanoparticles could go straight through as the particle size is smaller than the pore neck. However, after PANi coating, the neck would be narrowed or even partially blocked by the PANi, which would help in filtering out the Au nanoparticles.
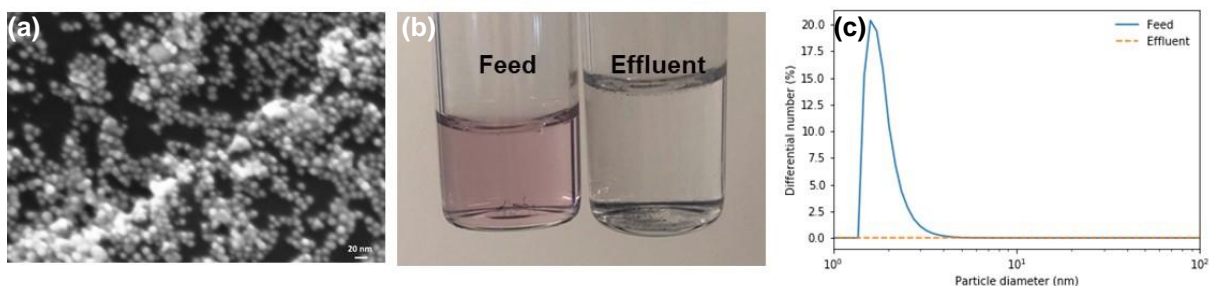
Figure 4.6 (a) SEM image of Au nanoparticles used in the CDI-UF test, showing them to be ~10 nm in diameter. (b) CDI-UF of 10 mM NaCl with Au nanoparticles and (c) particle size distribution of the feed solution and the effluent from the CDI-UF unit.

4.4 Conclusions

A nanoporous carbon scaffold, containing a fully interconnected set of 85 nm pores (NCS-85), was electrochemically coated with a conformal polyaniline (PANi) thin film (typically 3 – 20 nm in thickness), as confirmed primarily by FE-SEM. In this work, the PANi/NCS-85 material exhibited excellent electrochemical performance in the galvanostatic charge/discharge experiment in 3 M NaCl, giving a high capacitance of up to 335 F/g, a high energy density (32 – 47 Wh/kg), and also a high power density (235 – 4660 W/kg), all of which are very promising for energy storage applications.

The capacitive performance of the as-prepared PANi-6/NCS-85 was very stable after 1000 charge/discharge cycles (from -0.5 V to +0.5 V vs. Ag/AgCl), retaining 83% of the starting capacitance value. The retained capacitance of the PANi-6/NCS-85 after 1000 cycles is still 7

times that of the NCS-85. The degradation of the specific capacitance of the PANi/NCS films may be attributed to an irreversible chemical transformation of the PANi films, as shown by Raman spectroscopy analysis. An asymmetric cell based on a PANi-6/NCS-85 anode and an NCS-85 cathode exhibited a salt adsorption capacity of 2.6 mg/g (0.019 mg/m^2) at 2 V. The salt adsorption capacity of the CDI cells, composed of the NCS-85 and/or the PANi-6/NCS-85, is lower than reported for many other carbon CDI electrodes reported in the literature. This is due to the much lower specific surface area of the NCS-85 and the PANi-coated NCS-85 vs the microporous carbon electrodes used in the literature. However, the adsorption time reported here is much lower (2 - 10 s) compared to the literature (tens of minutes to hours), due to the larger, order and low tortuosity nanostructure of the NCS material.

The asymmetric cell was also tested simultaneously for ultrafiltration of 10 nm Au nanoparticles from the feed liquid. Although the NCS-85 pore size is ca. 85 nm, and that of the PANi-6/NCS-85 materials is ca. 70 nm, the pore necks are much smaller, being between 13 ± 2 and 11 ± 1.7 nm for these two materials. This offers an explanation as to why these materials are able to completely filter out the 10 nm Au nanoparticles in these experiments. The results have shown that the PANi/NCS composites are very promising materials for next generation water treatment.

4.5 Supplementary Information
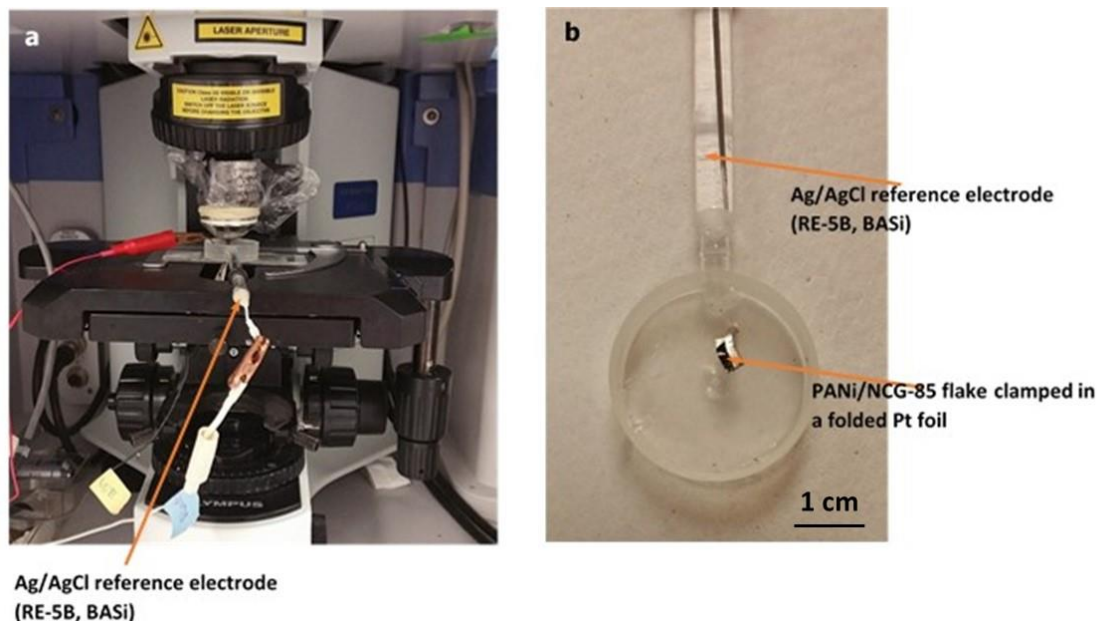
Figure S4.1 (a) Operando surface enhanced Raman spectroscopy setup based on an ARAMIS (Horiba) Raman microscope and a HDPE one-compartment spectroelectrochemical cell attached to a microscope glass. (b) Top-view of the spectroelectrochemical cell (4 mL).
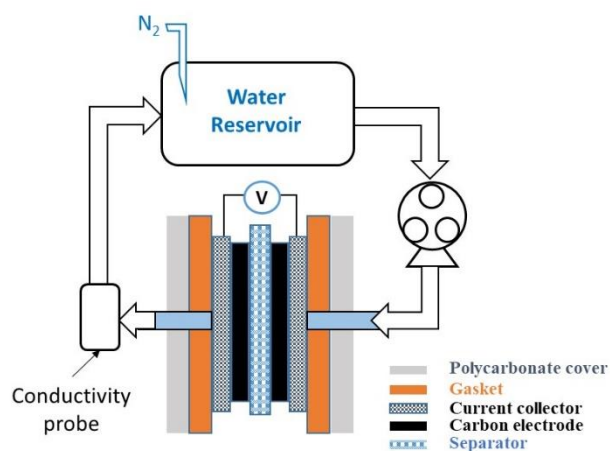
Figure S4.2 Schematic of the capacitive deionization (CDI) cell, which was also used for the combined CDI and ultrafiltration (UF) tests.
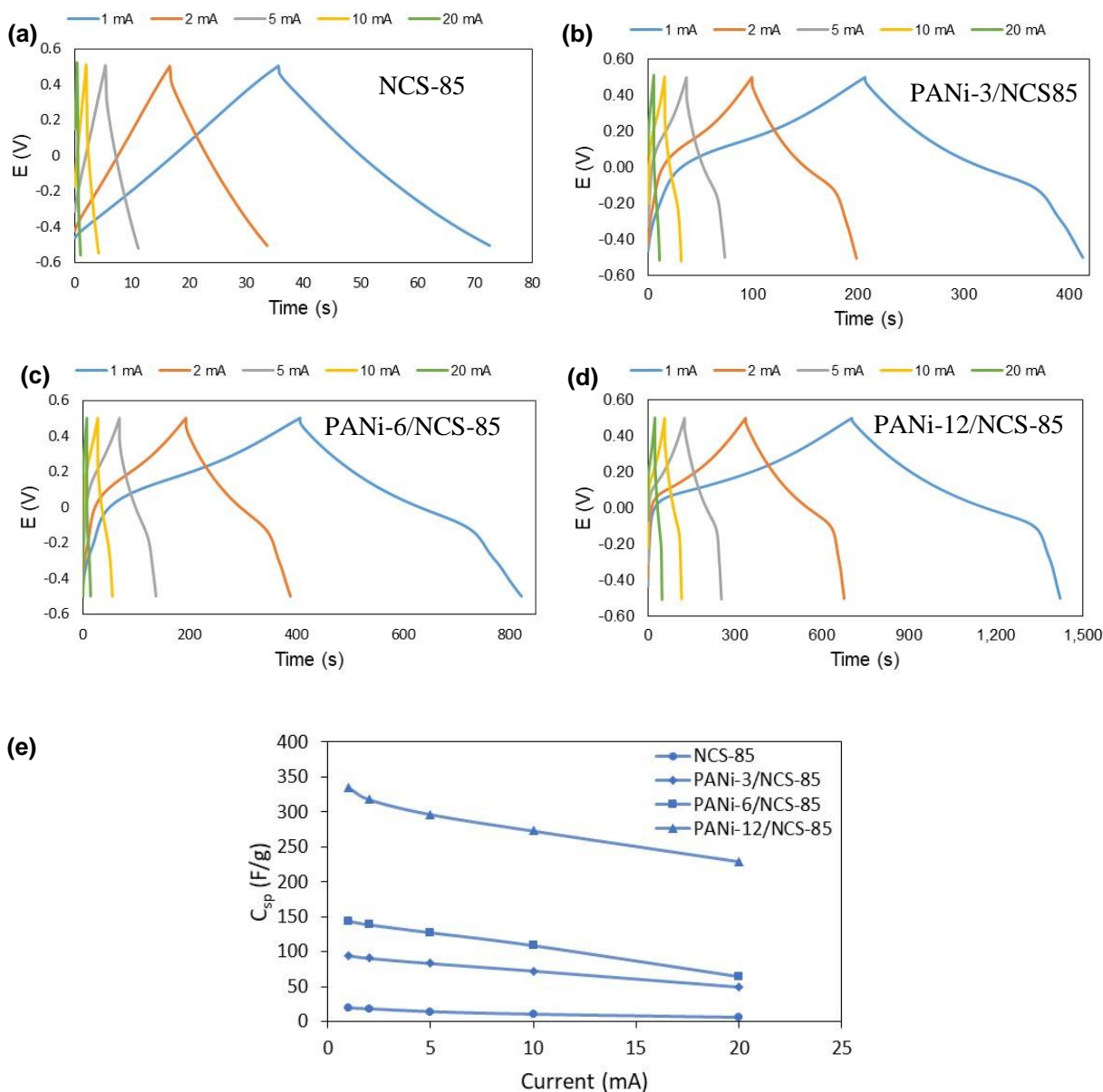
Figure S4.3 GCD profiles of (a) NCS-85, (b) PANi-3/NCS-85, (c) PANi-6/NCS-85 and (d) PANi-12/NCS-85-, obtained at various currents from 1 mA to 20 mA within a potential window between -0.5 V and 0.5 V vs. Ag/AgCl in 3 M NaCl. (e) The calculated C_{sp} as a function of the applied GCD current.

Table S4.1. C_{sp} **calculated from GCD curves of NCS-85 and PANi/NCS-85 composites at various currents and ESR values obtained in a three-electrode cell.**

		NCS-85	PANi-3/NCS-85	PANi-6/NCS-85	PANi-12/NCS-85
	1 mA	19.2	94.4	144	335
	2 mA	18.1	90.6	139	318
C_{sp}	5 mA	13.9	83.2	127	296
(F/g)	10 mA	10.2	72.2	109	273
	20 mA	5.58	49.3	63.8	229
ESR (Ω/cm^2)		19	11	6.5	6.0

Table S4.2. Energy density and power density of NCS-85 and PANi/NCS-85 composites at various currents.

	NCS-85		PANi-3/NCS-85		PANi-6/NCS-85		PANi-12/NCS-85	
Current	U	P	U	P	U	P	U	P
(mA)	(Wh/kg)	(W/kg)	(Wh/kg)	(W/kg)	(Wh/kg)	(W/kg)	(Wh/kg)	(W/kg)
1	2.7	258.4	13	228.0	20	173.3	47	233.3
2	2.5	534.5	13	455.0	19	353.9	44	468.2
5	1.9	1227	12	1134	18	927.5	41	1167
10	1.4	2394	10	2239	15	2000	38	2337
20	0.77	4651	6.8	4453	8.8	4754	32	4658
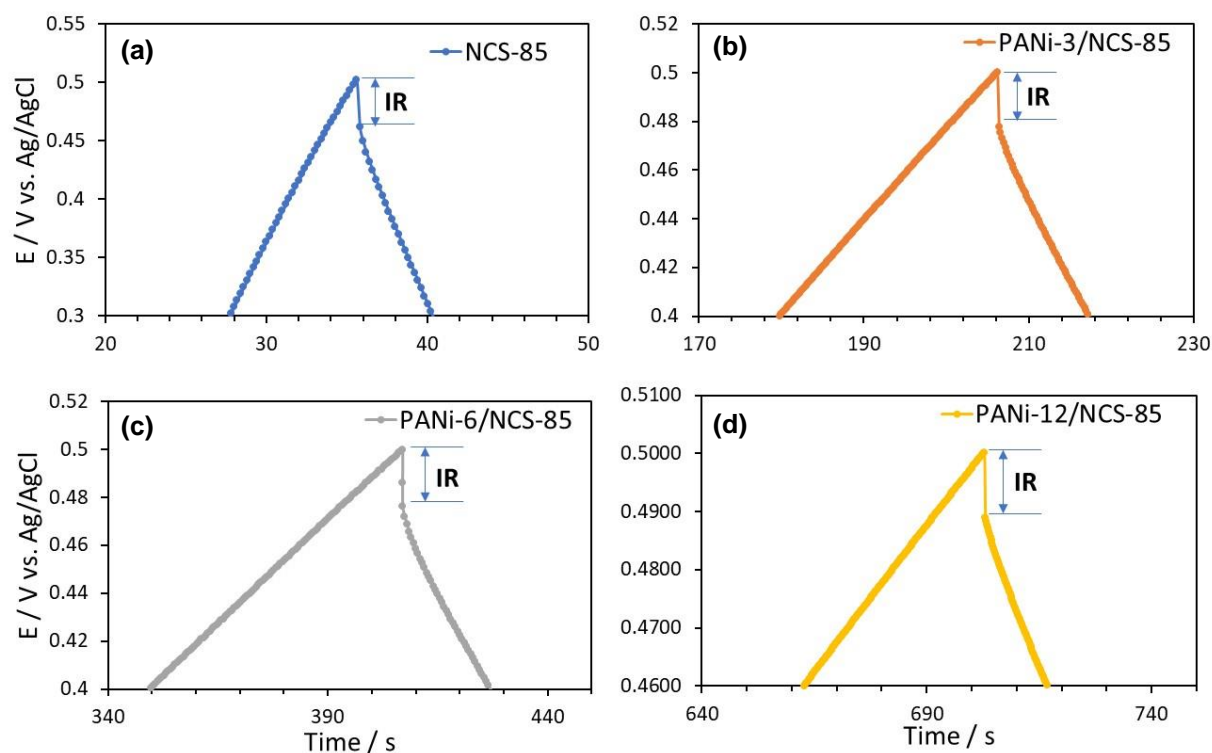
Figure S4.4 Zoomed in view of Fig. 4.2a, showing the IR drop for (a) NCS-85 and (b-d) for the PANi/NCS-85 composites at 1 mA in 3 M NaCl solution.
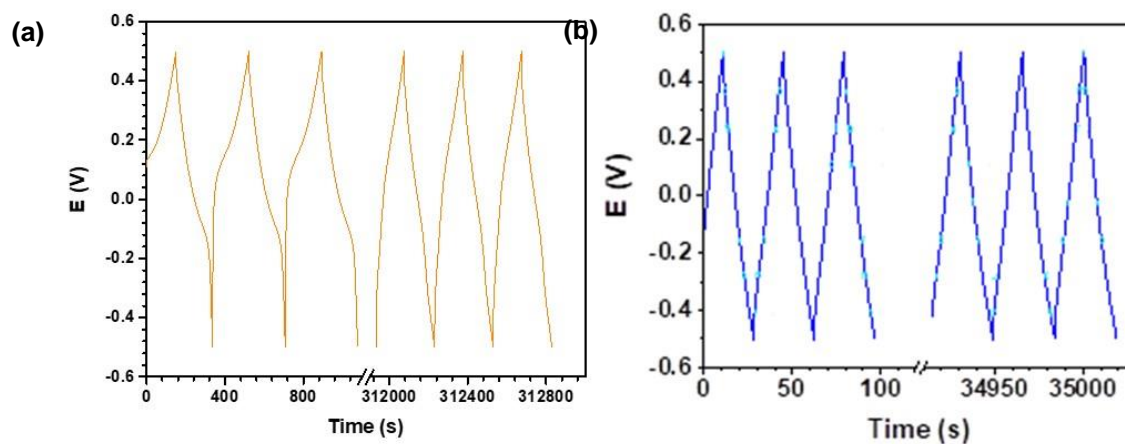
Figure S4.5 First three and last three GCD cycles for (a) PANi-6/NCS-85 and (b) NCS-85 in a three-electrode system in 3 M NaCl, charging at 2 mA and discharging at -2 mA, between -0.5 to + 0.5 V for 1000 cycles.
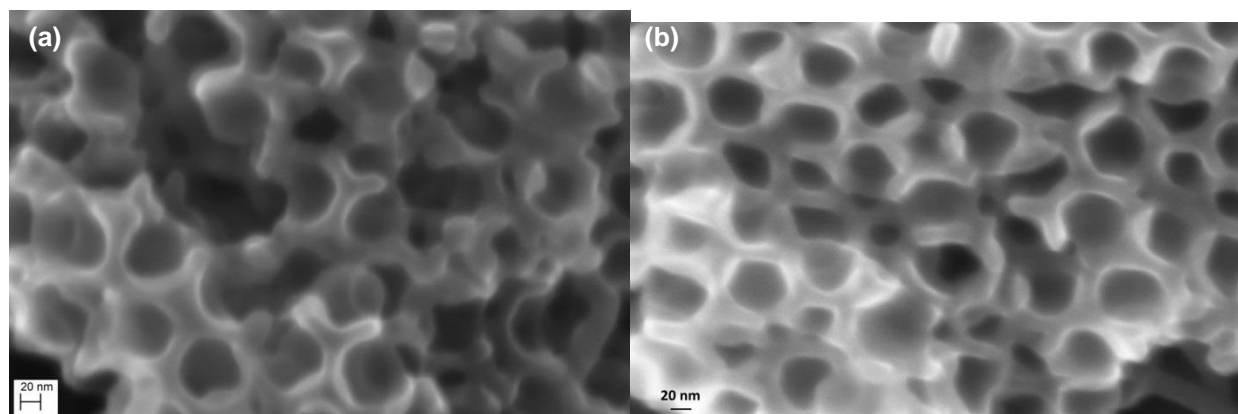
Figure S4.6 SEM images of (a) the surface and (b) the cross-section of PANi-6/NCS-85 after 1000 GCD cycles in 3 M NaCl at a constant current of 2 mA.
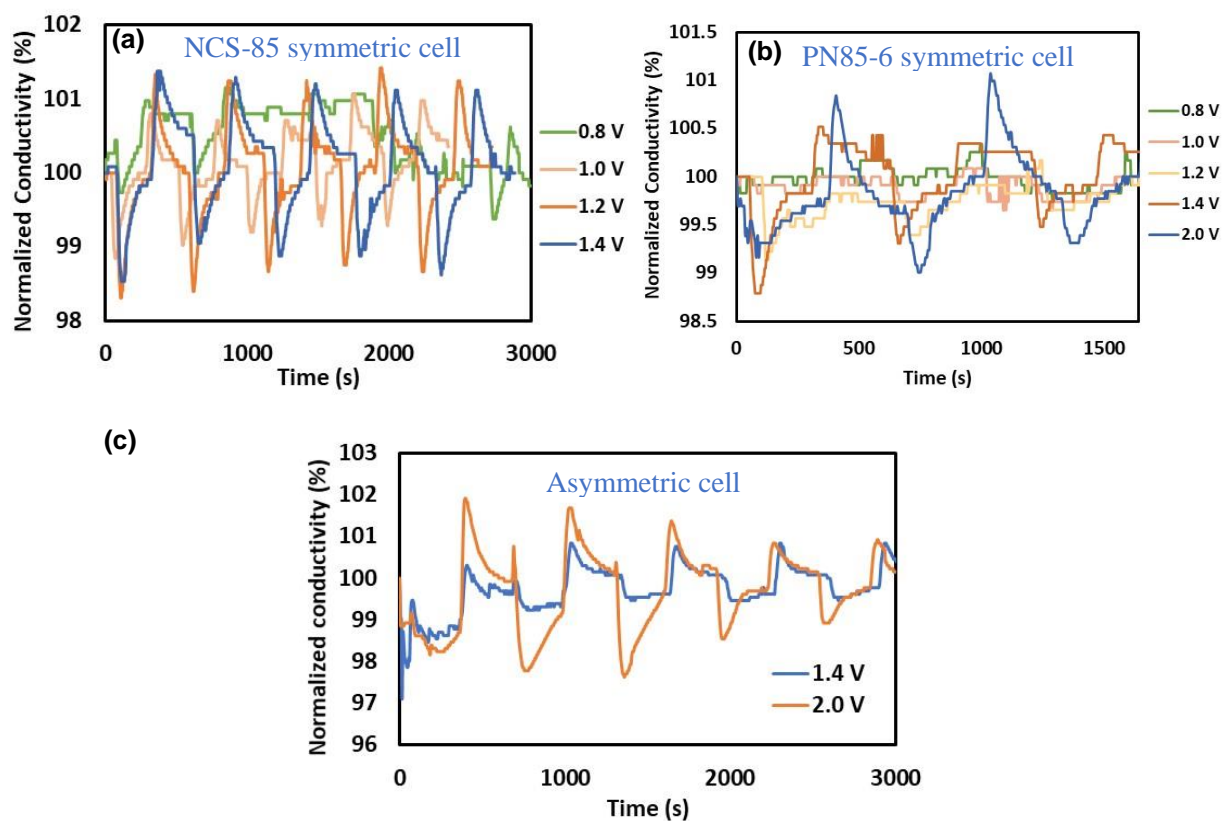
Figure S4.7 Normalized conductivity of the effluent during CDI operation using (a) NCS-85 electrodes, (b) PANi-6/NCS-85 electrodes and (c) asymmetric CDI cell composed of a PANi-6/NCS-85 anode and an NCS cathode under different constant voltages.

Table S4.3 Energy consumption for reducing the salinity by 1% during the CDI process using three cell configurations, including the NCS-85 and the PANi-6/NCS-85 symmetric cells, and an asymmetric cell composed of a PANi-6/NCS-12 anode and an NCS-85 cathode.

	U_{con} (kWh/m^3)		
Voltage (V)	NCS-85	PANi-6/NCS-85	Asymmetric
1.4	0.067	0.015	0.015
2.0	0.20	0.038	0.010

The energy consumption (U_{con}) of a symmetric NCS-85 cell, a symmetric PANi-6/NCS-85 cell and an asymmetric cell composed of a PANi-6/NCS-85 anode and an NCS-85 cathode in a flow-through cell, using 10 mM NaCl as the feed at 1.5 mL/min. The U_{con} (kWh/m^3) was calculated by integrating the current with time during the CDI charge process (Fig. 4.5a): $U_{con} = \frac{\int IV \mathrm{d}t}{3.6Ft}$, where I is the current during the CDI charging process (A), as shown in Fig. 4.5a, t is the charging time (s), V is the applied voltage (V), and F is the flow rate (m^3/s).

Chapter 5 Conclusions and Future Work

5.1 Conclusions

5.1.1 Conformal polyaniline (PANi) coating in the nanoporous carbon scaffold

(NCS) materials

In Chapter 3, the preparation of the NCS and the PANi/NCS composite materials has been demonstrated. This preparation includes the first time an electrochemical deposition of an ultrathin and conformal PANi film < 25 nm has been carried out on the entire internal surface of an NCS material (50 – 85 nm pore size). The thickness of the PANi coating was shown to be fully tunable by controlling the cyclic voltammetry (CV) conditions (i.e. potential limits, sweep rate) used during PANi deposition. The as-prepared PANi/NCS composites retained a three-dimensional nanoporous structure (5% decrease in the BET surface area and 1 – 50% smaller pore size), and showed optimal thermal stability (74% weight remaining after heating to 1000 ˚C), as demonstrated by the N_2 adsorption/desorption and the TGA results.

5.1.2 Improved electrochemical performance of the PANi/NCS composites

The electrical capacitance of the PANi/NCS composites, calculated from the CVs, are much larger as compared to the NCS material alone: a capacitance of 389 F/g was obtained for PANi-12/NCS-85, while NCS-85 exhibited a capacitance of 17 F/g measured at 1 mV/s in 3 M NaCl. This increase in value is due to the pseudo-capacitance contributed by the PANi film, and its redox reactions that were found to be quite rapid, suggesting a desirable redox reversibility of the PANi film.

The EIS-determined time constant was found to increase with increasing PANi thickness, from 3 s for bare NCS-85 to 45 s for PANi-12/NCS-85. This resulted in a decreased rate capability

due to the decreased pore diameter in the PANi/NCS composites. However, within the scan rate tested in this thesis work, such as 20 mV/s, the capacitance of the PANi/NCS composites are still significantly larger (ca. twelve-fold) than for the bare NCS materials.

5.1.3 Energy storage performance of the NCS and PANi/NCS materials

In Chapter 4, the energy storage performance of the NCS-85 and the PANi/NCS-85 composites have been demonstrated using galvanostatic charge/discharge (GCD) tests in a three-electrode system. The specific capacitance (C_{sp}) for the PANi/NCS-85 composites, calculated from the GCD data, is larger compared to that for NCS-85 over the currents tested (1 mA – 20 mA), i.e., 335 F/g and 229 F/g for PANi-12/NCS-85 at 1 mA and 20 mA, respectively, compared to 19 F/g and 6 F/g, respectively for the NCS-85 counterpart. The energy density increased from 2.7 Wh/kg for NCS-85 to 47 Wh/kg for the PANi-12/NCS-85 composite, without losing much power density (258 W/kg for the NCS-85, 233 W/kg for the PANi-12/NCS-85).

The cyclic stability of the NCS materials was found to be excellent, with no loss in their capacitance after 1000 GCD cycles at 2 mA in 3 M NaCl, while the PANi-6/NCS-85 composites retained 83% of their initial capacitance, which is also very stable. The capacitance loss of the PANi/NCS-85 composite is likely due to the irreversible oxidation or hydrolysis of the PANi film during the charging processes, as shown from the Raman spectroscopy data.

5.1.4 Combined capacitive deionization and ultrafiltration using NCS and PANi-NCS composites

In Chapter 4, the PANi-NCS composites were also examined for their performance in a CDI experiment.

The desalination performance of the PANi-6/NCS-85 and the NCS materials was demonstrated using a flow-through CDI cell in 10 mM NaCl solution. Three different cell configurations of two types, symmetric and asymmetric were used for testing. The two symmetric configurations had either NCS-85 serving as both electrodes, or PANi-6/NCS-85 as both electrodes. The asymmetric configuration had a PANi-6/NCS-85 anode and an NCS-85 cathode. The salt adsorption capacity at 2 V charging voltage for three different cell configurations was 1.4 mg/g (NCS-85 symmetric cell), 0.81 mg/g (PANi-6/NCS-85 symmetric cell) and 2.64 mg/g (asymmetric cell). The asymmetric cell showed the highest salt removal capacitance, salt removal rate, and charge efficiency among the three configurations tested.

The salt adsorption capacity of the CDI cells, composed of the NCS-85 and/or the PANi-6/NCS-85, is lower than reported for many other carbon CDI electrodes reported in the literature. This is due to the much lower specific surface area of the NCS-85 and the PANi-coated NCS-85 vs the microporous carbon electrodes used in the literature. However, the adsorption time reported here is much lower (2 - 10 s) compared to the literature (tens of minutes to hours), due to the larger, order and low tortuosity nanostructure of the NCS material.

The same flow-through cell was also used in a combined ultrafiltration and CDI experiment. Au nanoparticles (ca. 10 nm diameter) could be filtered out when using the asymmetric cell, while also removing solution ions in the flow-through CDI configuration. This is the first time that nanoparticles and salt ions were removed from a feed in one step by combining CDI and UF.

This thesis work has demonstrated the excellent capacitive properties of the novel NCS material and the PANi/NCS composites materials, thus making a highly useful contribution to the

fields of material science, energy storage, and water treatment. This work can thus be used as a starting point for future studies focused on one-step water/wastewater treatment technologies.

5.2 Suggested future work

There are some recommended extensions for this thesis work, as given below.

1. The formation of a conformal PANi coating inside the porous structure of carbon materials can enhance their electrochemical capacitance, while maintaining a desirable porous structure, if the deposition is done correctly. Determining the mechanism of the polymerization reaction inside the carbon pores and further optimization of the conditions for conformal film formation would allow conformal PANi deposition in other porous materials and the formation of conformal coatings of other interesting polymers (e.g., polypyrrole, PEDOT).

2. This thesis work involved the deposition of PANi inside NCS with pore sizes of 50 and 85 nm. It would also be interesting to attempt to polymerize aniline inside NCS with smaller pores (12 – 50 nm) to demonstrate if the same preparation method would work. As NCS with pore sizes of 12 – 50 nm have larger surface areas, coating with PANi would likely lead to larger specific capacitances (C_{sp}), leading to more promising supercapacitor and CDI applications.

3. The flow-by CDI cell was reported to have a higher salt removal capacity and rate compared to the flow-through configuration.[42] It is thus worth testing the CDI performance of a flow-by configuration using the NCS-85 and the PANi/NCS-85 composites, or the NCS and PANi/NCS with other pore sizes.

4. The combination of ultrafiltration and CDI was tested in this thesis work. However, there is a need to examine issues such as the stability, fouling, and the effect of the presence of particulates of mixed sizes and properties.

References

[1] M. Elimelech and W. A. Phillip, "The Future of Seawater Desalination: Energy, Technology, and the Environment," *Science (80-.).*, vol. 333, no. 6043, pp. 712–717, Aug. 2011.

[2] R. Zhang *et al.*, "Antifouling membranes for sustainable water purification: strategies and mechanisms," *Chem. Soc. Rev.*, vol. 45, no. 21, pp. 5888–5924, 2016.

[3] J. Eliasson, "The rising pressure of global water shortages," *Nature*, vol. 517, 2015.

[4] R. F. Service, "Desalination Freshens Up," *Science (80-.).*, vol. 313, no. 5790, pp. 1088–1090, 2006.

[5] E. Jones, M. Qadir, M. T. H. van Vliet, V. Smakhtin, and S. Kang, "The state of desalination and brine production: A global outlook," *Sci. Total Environ.*, vol. 657, pp. 1343–1356, Mar. 2019.

[6] S. J. Duranceau, R. J. Wilder, and S. S. Douglas, "Guidance and recommendations for posttreatment of desalinated water," *J. Am. Water Works Assoc.*, vol. 104, no. 9, pp. E510–E520, Sep. 2012.

[7] R. Semiat, "Energy Issues in Desalination Processes," *Environ. Sci. Technol.*, vol. 42, no. 22, pp. 8193–8201, Nov. 2008.

[8] M. M. Khin, A. S. Nair, V. J. Babu, R. Murugan, and S. Ramakrishna, "A review on nanomaterials for environmental remediation," *Energy Environ. Sci.*, vol. 5, no. 8, p. 8075, 2012.

[9] M. A. Anderson, A. L. Cudero, and J. Palma, "Capacitive deionization as an electrochemical means of saving energy and delivering clean water. Comparison to present desalination practices: Will it compete?," *Electrochim. Acta*, vol. 55, no. 12, pp.

3845–3856, Apr. 2010.

[10]   M. E. Suss, S. Porada, X. Sun, P. M. Biesheuvel, J. Yoon, and V. Presser, "Water

desalination via capacitive deionization: what is it and what can we expect from it?,"

Energy Environ. Sci., vol. 8, no. 8, pp. 2296–2319, 2015.

[11]   L. F. Greenlee, D. F. Lawler, B. D. Freeman, B. Marrot, and P. Moulin, "Reverse osmosis

desalination: Water sources, technology, and today's challenges," *Water Res.*, vol. 43, no.

9, pp. 2317–2348, May 2009.

[12]   J. Ma, L. Wang, F. Yu, and X. Dai, "Mesoporous amorphous FePO4

nanosphere@Graphene as a faradic electrode in capacitive deionization for high-capacity

and fast removal of NaCl from water," *Chem. Eng. J.*, vol. 370, pp. 938–943, Aug. 2019.

[13]   S. Porada, R. Zhao, A. Van Der Wal, V. Presser, and P. M. Biesheuvel, "Review on the

science and technology of water desalination by capacitive deionization," *Prog. Mater.*

Sci., vol. 58, no. 8, pp. 1388–1442, 2013.

[14]   R. Zhao, P. M. Biesheuvel, and A. van der Wal, "Energy consumption and constant

current operation in membrane capacitive deionization," *Energy Environ. Sci.*, vol. 5, no.

11, p. 9520, 2012.

[15]   M. E. Suss and V. Presser, "Water Desalination with Energy Storage Electrode

Materials," *Joule*, vol. 2, no. 1, pp. 25–35, 2018.

[16]   A. M. Johnson, A. W. Venolia, R. G. Wilbourne, and J. Newman, "The electrosorb

process for desalting water," Washington, 1970.

[17]   R. Zhao, S. Porada, P. M. Biesheuvel, and A. van der Wal, "Energy consumption in

membrane capacitive deionization for different water recoveries and flow rates, and

comparison with reverse osmosis," *Desalination*, vol. 330, pp. 35–41, Dec. 2013.

[18]   A. Y. Cetinkaya and L. Bilgili, "Life Cycle Comparison of Membrane Capacitive Deionization and Reverse Osmosis Membrane for Textile Wastewater Treatment," *Water, Air, Soil Pollut.*, vol. 230, no. 7, p. 149, Jul. 2019.

[19]   M. A. Anderson, A. L. Cudero, and J. Palma, "Capacitive deionization as an electrochemical means of saving energy and delivering clean water. Comparison to present desalination practices: Will it compete?," *Electrochim. Acta*, vol. 55, no. 12, pp. 3845–3856, Apr. 2010.

[20]   R. Zhao, S. Porada, P. M. Biesheuvel, and A. van der Wal, "Energy consumption in membrane capacitive deionization for different water recoveries and flow rates, and comparison with reverse osmosis," *Desalination*, vol. 330, pp. 35–41, Dec. 2013.

[21]   G. Wang, L. Zhang, and J. Zhang, "A review of electrode materials for electrochemical supercapacitors," *Chem. Soc. Rev.*, vol. 41, no. 2, pp. 797–828, 2012.

[22]   Y. Oren, "Capacitive deionization (CDI) for desalination and water treatment - past, present and future (a review)," *Desalination*, vol. 228, no. 1–3, pp. 10–29, 2008.

[23]   Y. Liu, C. Nie, X. Liu, X. Xu, Z. Sun, and L. Pan, "Review on carbon-based composite materials for capacitive deionization," *RSC Adv.*, vol. 5, no. 20, pp. 15205–15225, 2015.

[24]   P. Srimuk *et al.*, "Faradaic deionization of brackish and sea water via pseudocapacitive cation and anion intercalation into few-layered molybdenum disulfide," *J. Mater. Chem. A*, vol. 5, no. 30, pp. 15640–15649, 2017.

[25]   D. S. Achilleos and T. A. Hatton, "Selective Molecularly Mediated Pseudocapacitive Separation of Ionic Species in Solution," *ACS Appl. Mater. Interfaces*, vol. 8, no. 48, pp. 32743–32753, Dec. 2016.

[26]   X. Y. Gu, Y. Yang, Y. Hu, M. Hu, J. Huang, and C. Y. Wang, "Facile fabrication of

graphene-polypyrrole-Mn composites as high-performance electrodes for capacitive deionization," *J. Mater. Chem. A*, vol. 3, no. 11, pp. 5866–5874, 2015.

[27]   E. Frackowiak and F. Béguin, "Carbon materials for the electrochemical storage of energy in capacitors," *Carbon N. Y.*, vol. 39, no. 6, pp. 937–950, May 2001.

[28]   X. Su and T. A. Hatton, "Redox-electrodes for selective electrochemical separations," *Adv. Colloid Interface Sci.*, vol. 244, pp. 6–20, Jun. 2017.

[29]   H. Yin *et al.*, "Three-dimensional graphene/metal oxide nanoparticle hybrids for high-performance capacitive deionization of saline water," *Adv. Mater.*, vol. 25, no. 43, pp. 6270–6276, 2013.

[30]   A. Aldalbahi, M. Rahaman, P. Govindasami, M. Almoiqli, T. Altalhi, and A. Mezni, "Construction of a Novel Three-Dimensional PEDOT/RVC Electrode Structure for Capacitive Deionization: Testing and Performance," *Materials (Basel).*, vol. 10, no. 7, p. 847, Jul. 2017.

[31]   J. Yang, L. Zou, H. Song, and Z. Hao, "Development of novel MnO2/nanoporous carbon composite electrodes in capacitive deionization technology," *Desalination*, vol. 276, no. 1–3, pp. 199–206, 2011.

[32]   F. Zhou, T. Gao, M. Luo, and H. Li, "Preferential electrosorption of anions by C/Na0.7MnO2asymmetrical electrodes," *Sep. Purif. Technol.*, vol. 191, pp. 322–327, 2018.

[33]   S. Kim, J. Lee, C. Kim, and J. Yoon, "Na2FeP2O7 as a Novel Material for Hybrid Capacitive Deionization," *Electrochim. Acta*, vol. 203, pp. 265–271, Jun. 2016.

[34]   J. Lee, S. Kim, C. Kim, and J. Yoon, "Hybrid capacitive deionization to enhance the desalination performance of capacitive techniques," *Energy Environ. Sci.*, vol. 7, no. 11,

pp. 3683–3689, 2014.

[35]   A. G. El-Deen, J.-H. Choi, C. S. Kim, K. A. Khalil, A. A. Almajid, and N. A. M. Barakat, "TiO2 nanorod-intercalated reduced graphene oxide as high performance electrode material for membrane capacitive deionization," *Desalination*, vol. 361, pp. 53–64, Apr. 2015.

[36]   K. Laxman, M. T. Z. Myint, R. Khan, T. Pervez, and J. Dutta, "Improved desalination by zinc oxide nanorod induced electric field enhancement in capacitive deionization of brackish water," *Desalination*, vol. 359, pp. 64–70, Mar. 2015.

[37]   H. Wang, J. Lin, and Z. X. Shen, "Polyaniline (PANi) based electrode materials for energy storage and conversion," *J. Sci. Adv. Mater. Devices*, vol. 1, no. 3, pp. 225–255, Sep. 2016.

[38]   X. Gao, A. Omosebi, J. Landon, and K. Liu, "Surface charge enhanced carbon electrodes for stable and efficient capacitive deionization using inverted adsorption-desorption behavior," *Energy Environ. Sci.*, vol. 8, no. 3, pp. 897–909, 2015.

[39]   H. Li, L. Zou, L. Pan, and Z. Sun, "Novel graphene-like electrodes for capacitive deionization," *Environ. Sci. Technol.*, vol. 44, no. 22, pp. 8692–8697, 2010.

[40]   C. Huyskens, J. Helsen, and A. B. de Haan, "Capacitive deionization for water treatment: Screening of key performance parameters and comparison of performance for different ions," *Desalination*, vol. 328, pp. 8–16, Nov. 2013.

[41]   E. Avraham, M. Noked, Y. Bouhadana, A. Soffer, and D. Aurbach, "Limitations of Charge Efficiency in Capacitive Deionization," *J. Electrochem. Soc.*, vol. 156, no. 10, p. P157, 2009.

[42]   E. M. Remillard, A. N. Shocron, J. Rahill, M. E. Suss, and C. D. Vecitis, "A direct

comparison of flow-by and flow-through capacitive deionization," *Desalination*, vol. 444, pp. 169–177, Oct. 2018.

[43] C. Zhang, D. He, J. Ma, W. Tang, and T. D. Waite, "Comparison of faradaic reactions in flow-through and flow-by capacitive deionization (CDI) systems," *Electrochim. Acta*, vol. 299, pp. 727–735, Mar. 2019.

[44] P. M. Biesheuvel, R. Zhao, S. Porada, and A. van der Wal, "Theory of membrane capacitive deionization including the effect of the electrode pore space," *J. Colloid Interface Sci.*, vol. 360, no. 1, pp. 239–248, 2011.

[45] Y. Huang, F. Chen, L. Guo, and H. Y. Yang, "Ultrahigh performance of a novel electrochemical deionization system based on a NaTi 2 (PO 4) 3 /rGO nanocomposite," *J. Mater. Chem. A*, vol. 5, no. 34, pp. 18157–18165, 2017.

[46] X. Su *et al.*, "Asymmetric Faradaic systems for selective electrochemical separations," *Energy Environ. Sci.*, vol. 10, no. 5, pp. 1272–1283, 2017.

[47] S. Jeon *et al.*, "Desalination via a new membrane capacitive deionization process utilizing flow-electrodes," *Energy Environ. Sci.*, vol. 6, no. 5, p. 1471, 2013.

[48] E. Avraham, M. Noked, Y. Bouhadana, A. Soffer, and D. Aurbach, "Limitations of charge efficiency in capacitive deionization processes III: The behavior of surface oxidized activated carbon electrodes," *Electrochim. Acta*, vol. 56, no. 1, pp. 441–447, Dec. 2010.

[49] P. Xu, J. E. Drewes, D. Heil, and G. Wang, "Treatment of brackish produced water using carbon aerogel-based capacitive deionization technology," *Water Res.*, vol. 42, no. 10–11, pp. 2605–2617, 2008.

[50] L. Wang *et al.*, "Capacitive deionization of NaCl solutions using carbon nanotube sponge electrodes," *J. Mater. Chem.*, vol. 21, no. 45, pp. 18295–18299, 2011.

[51] H. Wang *et al.*, "In situ creating interconnected pores across 3D graphene architectures and their application as high performance electrodes for flow-through deionization capacitors," *J. Mater. Chem. A*, vol. 4, no. 13, pp. 4908–4919, 2016.

[52] L.-G. Chong, P.-A. Chen, J.-Y. Huang, H.-L. Huang, and H. P. Wang, "Capacitive deionization of a RO brackish water by AC/graphene composite electrodes," *Chemosphere*, vol. 191, pp. 296–301, Jan. 2018.

[53] D. Zhang, T. Yan, L. Shi, Z. Peng, X. Wen, and J. Zhang, "Enhanced capacitive deionization performance of graphene/carbon nanotube composites," *J. Mater. Chem.*, vol. 22, no. 29, p. 14696, 2012.

[54] J. Zhang, J. Fang, J. Han, T. Yan, L. Shi, and D. Zhang, "N, P, S co-doped hollow carbon polyhedra derived from MOF-based core–shell nanocomposites for capacitive deionization," *J. Mater. Chem. A*, vol. 6, no. 31, pp. 15245–15252, 2018.

[55] Y. H. Liu, H. C. Hsi, K. C. Li, and C. H. Hou, "Electrodeposited manganese dioxide/activated carbon composite as a high-performance electrode material for capacitive deionization," *ACS Sustain. Chem. Eng.*, vol. 4, no. 9, pp. 4762–4770, 2016.

[56] S. Choi, B. Chang, S. Kim, J. Lee, J. Yoon, and J. W. Choi, "Battery Electrode Materials with Omnivalent Cation Storage for Fast and Charge-Efficient Ion Removal of Asymmetric Capacitive Deionization," *Adv. Funct. Mater.*, vol. 28, no. 35, p. 1802665, Aug. 2018.

[57] H. P. Cong, X. C. Ren, P. Wang, and S. H. Yu, "Flexible graphene-polyaniline composite paper for high-performance supercapacitor," *Energy Environ. Sci.*, vol. 6, no. 4, pp. 1185–1191, 2013.

[58] B. Dong, B. L. He, C. L. Xu, and H. L. Li, "Preparation and electrochemical

characterization of polyaniline/multi-walled carbon nanotubes composites for supercapacitor," *Mater. Sci. Eng. B Solid-State Mater. Adv. Technol.*, vol. 143, no. 1–3, pp. 7–13, 2007.

[59]   L. Z. Fan, Y. S. Hu, J. Maier, P. Adelhelm, B. Smarsly, and M. Antonietti, "High electroactivity of polyaniline in supercapacitors by using a hierarchically porous carbon monolith as a support," *Adv. Funct. Mater.*, vol. 17, no. 16, pp. 3083–3087, 2007.

[60]   Z. F. Li, H. Zhang, Q. Liu, L. Sun, L. Stanciu, and J. Xie, "Fabrication of high-surface-area graphene/polyaniline nanocomposites and their application in supercapacitors," *ACS Appl. Mater. Interfaces*, vol. 5, no. 7, pp. 2685–2691, 2013.

[61]   H. Wang, J. Liu, Z. Chen, S. Chen, T. Chien, and J. Lin, "Electrochimica Acta Synergistic capacitive behavior between polyaniline and carbon black," *Electrochim. Acta*, vol. 230, pp. 236–244, 2017.

[62]   Q. Zhang, A. Zhou, J. Wang, J. Wu, and H. Bai, "Degradation-induced capacitance: a new insight into the superior capacitive performance of polyaniline/graphene composites," *Energy Environ. Sci.*, vol. 10, no. 11, pp. 2372–2382, 2017.

[63]   W. Duan, A. Ronen, S. Walker, and D. Jassby, "Polyaniline-Coated Carbon Nanotube Ultrafiltration Membranes: Enhanced Anodic Stability for in Situ Cleaning and Electro-Oxidation Processes," *ACS Appl. Mater. Interfaces*, vol. 8, no. 34, pp. 22574–22584, 2016.

[64]   V. S. Jamadade, D. S. Dhawale, and C. D. Lokhande, "Studies on electrosynthesized leucoemeraldine, emeraldine and pernigraniline forms of polyaniline films and their supercapacitive behavior," *Synth. Met.*, vol. 160, no. 9–10, pp. 955–960, 2010.

[65]   M. J. García-Fernández, M. M. Pastor-Blas, F. Epron, and A. Sepúlveda-Escribano,

"Proposed mechanisms for the removal of nitrate from water by platinum catalysts supported on polyaniline and polypyrrole," *Appl. Catal. B Environ.*, vol. 225, pp. 162–171, Jun. 2018.

[66] J. Kim, S. Park, and N. F. Scherer, "Ultrafast dynamics of polarons in conductive polyaniline: Comparison of primary and secondary doped forms," *J. Phys. Chem. B*, vol. 112, no. 49, pp. 15576–15587, 2008.

[67] C. Oueiny, S. Berlioz, and F. X. Perrin, "Carbon nanotube-polyaniline composites," *Prog. Polym. Sci.*, vol. 39, no. 4, pp. 707–748, 2014.

[68] L. L. Zhang, S. Li, J. Zhang, P. Guo, J. Zheng, and X. S. Zhao, "Enhancement of electrochemical performance of macroporous carbon by surface coating of polyaniline," *Chem. Mater.*, vol. 22, no. 3, pp. 1195–1202, 2010.

[69] S.-J. Choi and S.-M. Park, "Electrochemistry of Conductive Polymers. XXVI. Effects of Electrolytes and Growth Methods on Polyaniline Morphology," *J. Electrochem. Soc.*, vol. 149, no. 2, p. E26, 2002.

[70] Y. Y. Smolin, K. L. Van Aken, M. Boota, M. Soroush, Y. Gogotsi, and K. K. S. Lau, "Engineering Ultrathin Polyaniline in Micro/Mesoporous Carbon Supercapacitor Electrodes Using Oxidative Chemical Vapor Deposition," *Adv. Mater. Interfaces*, vol. 4, no. 8, 2017.

[71] J. Wu, Q. Zhang, J. Wang, X. Huang, and H. Bai, "A self-assembly route to porous polyaniline/reduced graphene oxide composite materials with molecular-level uniformity for high-performance supercapacitors," *Energy Environ. Sci.*, vol. 11, no. 5, pp. 1280–1286, 2018.

[72] H. Zhang, J. Wang, Z. Wang, F. Zhang, and S. Wang, "Electrodeposition of polyaniline

nanostructures: A lamellar structure," *Synth. Met.*, vol. 159, no. 3–4, pp. 277–281, 2009.

[73]   S. Mu and Y. Yang, "Spectral characteristics of polyaniline nanostructures synthesized by using cyclic voltammetry at different scan rates," *J. Phys. Chem. B*, vol. 112, no. 37, pp. 11558–11563, 2008.

[74]   H. N. Dinh, "Electrochemical and structural studies of polyaniline film growth and degradation at different substrate surfaces," University of Calgary, 1998.

[75]   H. Wang *et al.*, "Synergistic capacitive behavior between polyaniline and carbon black," *Electrochimica Acta*, vol. 230. pp. 236–244, 2017.

[76]   G. Ye *et al.*, "Efficient treatment of brine wastewater through a flow-through technology integrating desalination and photocatalysis," *Water Res.*, vol. 157, pp. 134–144, Jun. 2019.

[77]   X. Li *et al.*, "Self-supported nanoporous carbon scaffold membranes," 2019.

[78]   V. I. Birss, X. Li, D. Banham, and D. Y. Kwok, "Porous Carbon Films," 2017.

[79]   E. M. Geniès, M. Lapkowski, and J. F. Penneau, "Cyclic voltammetry of polyaniline: interpretation of the middle peak," *J. Electroanal. Chem.*, vol. 249, no. 1–2, pp. 97–107, 1988.

[80]   J. P. Redfern, "Thermogravimetric Analysis," vol. 1, no. 906.

[81]   M. Thommes *et al.*, "Physisorption of gases, with special reference to the evaluation of surface area and pore size distribution (IUPAC Technical Report)," *Pure Appl. Chem.*, vol. 87, no. 9–10, pp. 1051–1069, Oct. 2015.

[82]   H. K. V Lotsch, *Confocal Raman Microscopy*. .

[83]   N. Elgrishi, K. J. Rountree, B. D. McCarthy, E. S. Rountree, T. T. Eisenhart, and J. L. Dempsey, "A Practical Beginner's Guide to Cyclic Voltammetry," *J. Chem. Educ.*, vol. 95, no. 2, pp. 197–206, 2018.

[84] J. H. Jang and S. M. Oh, "Complex Capacitance Analysis of Porous Carbon Electrodes for Electric Double-Layer Capacitors," *J. Electrochem. Soc.*, vol. 151, no. 4, p. A571, 2004.

[85] S. Yoon, J. H. Jang, B. H. Ka, and S. M. Oh, "Complex capacitance analysis on rate capability of electric-double layer capacitor (EDLC) electrodes of different thickness," *Electrochim. Acta*, vol. 50, no. 11, pp. 2255–2262, 2005.

[86] P. L. Taberna, P. Simon, and J. F. Fauvarque, "Electrochemical Characteristics and Impedance Spectroscopy Studies of Carbon-Carbon Supercapacitors," *J. Electrochem. Soc.*, vol. 150, no. 3, p. A292, 2003.

[87] M. D. Stoller and R. S. Ruoff, "Best practice methods for determining an electrode material's performance for ultracapacitors," *Energy Environ. Sci.*, vol. 3, no. 9, p. 1294, 2010.

[88] Y. Xu *et al.*, "Holey graphene frameworks for highly efficient capacitive energy storage," *Nat. Commun.*, vol. 5, 2014.

[89] J. Lee, S. Mahendra, and P. J. J. Alvarez, "Nanomaterials in the construction industry: A review of their applications and environmental health and safety considerations," *ACS Nano*, vol. 4, no. 7. pp. 3580–3590, 2010.

[90] W. Gu and G. Yushin, "Review of nanostructured carbon materials for electrochemical capacitor applications: Advantages and limitations of activated carbon, carbide-derived carbon, zeolite-templated carbon, carbon aerogels, carbon nanotubes, onion-like carbon, and graphene," *Wiley Interdiscip. Rev. Energy Environ.*, vol. 3, no. 5, pp. 424–473, 2014.

[91] E. Llobet, "Gas sensors using carbon nanomaterials: A review," *Sensors and Actuators, B: Chemical*, vol. 179. pp. 32–45, 2013.

[92] D. Y. Kwok *et al.*, "Wettability of colloid-imprinted carbons by contact angle kinetics and

water vapor sorption measurements," *Carbon N. Y.*, vol. 87, pp. 44–60, 2015.

[93] X. Li *et al.*, "Surface Characteristics of Microporous and Mesoporous Carbons Functionalized with Pentafluorophenyl Groups," *ACS Appl. Mater. Interfaces*, vol. 10, no. 2, pp. 2130–2142, 2018.

[94] X. Li *et al.*, "Improving the corrosion resistance of proton exchange membrane fuel cell carbon supports by pentafluorophenyl surface functionalization," *J. Power Sources*, vol. 378, pp. 732–741, Feb. 2018.

[95] J. Hu, X. U. Zou, A. Stein, and P. Bühlmann, "Ion-Selective Electrodes with Colloid-Imprinted Mesoporous Carbon as Solid Contact," *Anal. Chem.*, vol. 86, no. 14, pp. 7111–7118, Jul. 2014.

[96] Z. Li and M. Jaroniec, "Colloid-imprinted carbons as stationary phases for reversed-phase liquid chromatography," *Anal. Chem.*, vol. 76, no. 18, pp. 5479–5485, 2004.

[97] B. Fang, M. Kim, S. Hwang, and J. S. Yu, "Colloid-imprinted carbon with tailored nanostructure as an unique anode electrocatalyst support for formic acid oxidation," *Carbon N. Y.*, vol. 46, no. 6, pp. 876–883, 2008.

[98] H. R. Anderson *et al.*, "Black Carbon as an Additional Indicator of the Adverse Health Effects of Airborne Particles Compared with PM 10 and PM 2.5," *Environ. Health Perspect.*, vol. 119, no. 12, pp. 1691–1699, 2011.

[99] T. C. Wei and H. W. Hillhouse, "Mass transport and electrode accessibility through periodic self-assembled nanoporous silica thin films," *Langmuir*, vol. 23, no. 10, pp. 5689–5699, 2007.

[100] Y.-H. Cho *et al.*, "Ordered macroporous platinum electrode and enhanced mass transfer in fuel cells using inverse opal structure," *Nat. Commun.*, vol. 4, no. 1, 2013.

[101] S. M. Mahurin, J. S. Lee, X. Wang, and S. Dai, "Ammonia-activated mesoporous carbon membranes for gas separations," *J. Memb. Sci.*, vol. 368, no. 1–2, pp. 41–47, 2011.

[102] M. P. Siegal, D. L. Overmyer, R. J. Kottenstette, D. R. Tallant, and W. G. Yelton, "Nanoporous-carbon films for microsensor preconcentrators," *Appl. Phys. Lett.*, vol. 80, no. 21, pp. 3940–3942, 2002.

[103] L. Al-Mashat *et al.*, "Graphene/Polyaniline Nanocomposite for Hydrogen Sensing," *J. Phys. Chem. C*, vol. 114, no. 39, pp. 16168–16173, Oct. 2010.

[104] V. Gupta and N. Miura, "Electrochemically Deposited Polyaniline Nanowire's Network," *Electrochem. Solid-State Lett.*, vol. 8, no. 12, pp. 630–632, 2005.

[105] K. Shen *et al.*, "Toward interconnected hierarchical porous structure via chemical depositing organic nano-polyaniline on inorganic carbon scaffold for supercapacitor," *Synth. Met.*, vol. 199, pp. 205–213, Jan. 2015.

[106] H. Goktas, Z. Demircioglu, K. Sel, T. Gunes, and I. Kaya, "The optical properties of plasma polymerized polyaniline thin films," *Thin Solid Films*, vol. 548, pp. 81–85, Dec. 2013.

[107] H. N. Dinh, J. Ding, S. J. Xia, and V. I. Birss, "Multi-technique study of the anodic degradation of polyaniline films," *J. Electroanal. Chem.*, vol. 459, no. 1, pp. 45–56, 1998.

[108] J. H. Yoon *et al.*, "High performance flexible pH sensor based on polyaniline nanopillar array electrode," *J. Colloid Interface Sci.*, vol. 490, pp. 53–58, Mar. 2017.

[109] B. J. Johnson and S.-M. Park, "Electrochemistry of Conductive Polymers XX. Early Stages of Aniline Polymerization Studied by Spectroelectrochemical and Rotating Ring Disk Electrode Techniques," *J. Electrochem. Soc.*, vol. 143, no. 4, pp. 1277–1282, 1996.

[110] H. N. Dinh, P. Van, and V. I. Birss, "The Effect of Film Thickness and Growth Method on

Polyaniline Film Properties," vol. 146, no. 9, pp. 3324–3334, 1999.

[111] R. Mažeikienė, G. Niaura, and A. Malinauskas, "Raman spectroelectrochemical study of polyaniline at UV, blue, and green laser line excitation in solutions of different pH," *Synth. Met.*, vol. 243, pp. 97–106, Sep. 2018.

[112] R. Mažeikiená, G. Niaura, and A. Malinauskas, "In situ time-resolved Raman spectroelectrochemical study of aniline polymerization at platinum and gold electrodes," *Chemija*, vol. 29, no. 2, pp. 81–88, 2018.

[113] M. Trchová, Z. Morávková, M. Bláha, and J. Stejskal, "Raman spectroscopy of polyaniline and oligoaniline thin films," *Electrochim. Acta*, vol. 122, pp. 28–38, 2014.

[114] R. Mažeikienė, G. Niaura, and A. Malinauskas, "Raman spectroelectrochemical study on the kinetics of electrochemical degradation of polyaniline," *Polym. Degrad. Stab.*, vol. 93, no. 10, pp. 1742–1746, Oct. 2008.

[115] W. Feng, X. D. Bai, Y. Q. Lian, J. Liang, X. G. Wang, and K. Yoshino, "Well-aligned polyaniline/carbon-nanotube composite films grown by in-situ aniline polymerization," *Carbon N. Y.*, vol. 41, no. 8, pp. 1551–1557, 2003.

[116] C. Guo, L. Zhou, and J. Lv, "Effects of expandable graphite and modified ammonium polyphosphate on the flame-retardant and mechanical properties of wood flour-polypropylene composites," *Polym. Polym. Compos.*, vol. 21, no. 7, pp. 449–456, 2013.

[117] L. V. Lukachova *et al.*, "Electroactivity of chemically synthesized polyaniline in neutral and alkaline aqueous solutions: Role of self-doping and external doping," *J. Electroanal. Chem.*, vol. 544, no. SUPPL., pp. 59–63, 2003.

[118] S. Tian *et al.*, "Electroactivity of polyaniline multilayer films in neutral solution and their electrocatalyzed oxidation of β-nicotinamide adenine dinucleotide," *Adv. Funct. Mater.*,

vol. 13, no. 6, pp. 473–479, 2003.

[119] P. G. Youssef, R. K. AL-Dadah, and S. M. Mahmoud, "Comparative Analysis of Desalination Technologies," *Energy Procedia*, vol. 61, pp. 2604–2607, 2014.

[120] M. E. Suss, S. Porada, X. Sun, P. M. Biesheuvel, J. Yoon, and V. Presser, "Water desalination via capacitive deionization: what is it and what can we expect from it?," *Energy Environ. Sci.*, vol. 8, no. 8, pp. 2296–2319, 2015.

[121] F. Béguin, V. Presser, A. Balducci, and E. Frackowiak, "Carbons and electrolytes for advanced supercapacitors," *Adv. Mater.*, vol. 26, no. 14, pp. 2219–2251, 2014.

[122] W. Shi *et al.*, "Ultrahigh Performance of Novel Capacitive Deionization Electrodes based on A Three-Dimensional Graphene Architecture with Nanopores," *Sci. Rep.*, vol. 6, no. November 2015, p. 18966, 2016.

[123] K. Wang, Y. Liu, Z. Ding, Y. Li, T. Lu, and L. Pan, "Metal-organic-frameworks-derived NaTi 2 (PO 4) 3 /carbon composites for efficient hybrid capacitive deionization," *J. Mater. Chem. A*, vol. 7, no. 19, pp. 12126–12133, 2019.

[124] Y. Wu *et al.*, "A 3D ordered hierarchically porous non-carbon electrode for highly effective and efficient capacitive deionization supporting information," *J. Mater. Chem. A*, 2019.

[125] C. Yan, Y. W. Kanaththage, R. Short, C. T. Gibson, and L. Zou, "Graphene/Polyaniline nanocomposite as electrode material for membrane capacitive deionization," *Desalination*, vol. 344, pp. 274–279, 2014.

[126] C. Yan, L. Zou, and R. Short, "Single-walled carbon nanotubes and polyaniline composites for capacitive deionization," *Desalination*, vol. 290, pp. 125–129, 2012.

[127] J. Liu, M. Lu, J. Yang, J. Cheng, and W. Cai, "Capacitive desalination of ZnO/activated

carbon asymmetric capacitor and mechanism analysis," *Electrochim. Acta*, vol. 151, pp. 312–318, 2015.

[128] L. Guo *et al.*, "Prussian blue anode for high performance electrochemical deionization promoted by faradic mechanism," *Nanoscale*, 2017.

[129] H. K. Shon, S. Phuntsho, D. S. Chaudhary, S. Vigneswaran, and J. Cho, "Nanofiltration for water and wastewater treatment – a mini review," *Drink. Water Eng. Sci.*, vol. 6, no. 1, pp. 47–53, Jun. 2013.

[130] N. Hilal, H. Al-Zoubi, N. A. Darwish, A. W. Mohammad, and M. Abu Arabi, "A comprehensive review of nanofiltration membranes: Treatment, pretreatment, modelling, and atomic force microscopy," *Desalination*, vol. 170, no. 3, pp. 281–308, 2004.

[131] X. Li, C. Ai, R. Mayall, and V. I. Birss, "FILTRATION USING NANOPOROUS CARBON MEMBRANES," 62/715,085, 2018.

[132] C. Ai, I. V. Chernyshova, E. L. Gawron, S. Ponnurangam, and V. I. Birss, "Electrochemical formation of highly ordered, self-supported polyaniline/carbon composite scaffolds with fully controlled nanopore sizes."

[133] H. Wei, H. Gu, J. Guo, S. Wei, J. Liu, and Z. Guo, "Silica Doped Nanopolyaniline with Endured Electrochemical Energy Storage and the Magnetic Field Effects," *J. Phys. Chem. C*, vol. 117, no. 25, pp. 13000–13010, Jun. 2013.

[134] X. Gao, A. Omosebi, J. Landon, and K. Liu, "Surface charge enhanced carbon electrodes for stable and efficient capacitive deionization using inverted adsorption-desorption behavior," *Energy Environ. Sci.*, vol. 8, pp. 897–909, 2015.

[135] X. Wen, D. Zhang, L. Shi, T. Yan, H. Wang, and J. Zhang, "Three-dimensional hierarchical porous carbon with a bimodal pore arrangement for capacitive deionization,"

J. Mater. Chem., vol. 22, no. 45, p. 23835, 2012.

[136] S. Zhao, F. Wu, L. Yang, L. Gao, and A. F. Burke, "A measurement method for determination of dc internal resistance of batteries and supercapacitors," *Electrochem. commun.*, vol. 12, no. 2, pp. 242–245, Feb. 2010.

[137] H. Wang *et al.*, "Synergistic capacitive behavior between polyaniline and carbon black," *Electrochim. Acta*, vol. 230, pp. 236–244, Mar. 2017.

[138] Z. Morávková, M. Trchová, M. Exnerová, and J. Stejskal, "The carbonization of thin polyaniline films," *Thin Solid Films*, vol. 520, no. 19, pp. 6088–6094, Jul. 2012.

[139] I. Šeděnková, M. Trchová, and J. Stejskal, "Thermal degradation of polyaniline films prepared in solutions of strong and weak acids and in water - FTIR and Raman spectroscopic studies," *Polym. Degrad. Stab.*, vol. 93, no. 12, pp. 2147–2157, Dec. 2008.

[140] G. Ćirić-Marjanović, M. Trchová, and J. Stejskal, "The chemical oxidative polymerization of aniline in water: Raman spectroscopy," *J. Raman Spectrosc.*, vol. 39, no. 10, pp. 1375–1387, Oct. 2008.

[141] M. Trchová, P. Matějka, J. Brodinová, A. Kalendová, J. Prokeš, and J. Stejskal, "Structural and conductivity changes during the pyrolysis of polyaniline base," *Polym. Degrad. Stab.*, vol. 91, no. 1, pp. 114–121, Jan. 2006.

[142] N.-L. Liu, S.-H. Sun, and C.-H. Hou, "Studying the electrosorption performance of activated carbon electrodes in batch-mode and single-pass capacitive deionization," *Sep. Purif. Technol.*, vol. 215, pp. 403–409, May 2019.

[143] C. Yan, L. Zou, and R. Short, "Polyaniline-modified activated carbon electrodes for capacitive deionisation," *Desalination*, vol. 333, no. 1, pp. 101–106, 2014.

[144] T. Wu, G. Wang, Q. Dong, B. Qian, Y. Meng, and J. Qiu, "Asymmetric capacitive

deionization utilizing nitric acid treated activated carbon fiber as the cathode,"

Electrochim. Acta, vol. 176, pp. 426–433, 2015.

[145] Y. Wimalasiri and L. Zou, "Carbon nanotube/graphene composite for enhanced capacitive deionization performance," *Carbon N. Y.*, vol. 59, pp. 464–471, Aug. 2013.

[146] M. A. Anderson, A. L. Cudero, and J. Palma, "Capacitive deionization as an electrochemical means of saving energy and delivering clean water. Comparison to present desalination practices: Will it compete?," *Electrochim. Acta*, vol. 55, no. 12, pp. 3845–3856, 2010.

APPENDIX A: COPYRIGHT FORMS

A.1. Letter of Permission

To Whom It May Concern

This letter is to let you know that I am permitting Ms. Chengying Ai to use the manuscripts co-authored by me in her Master's thesis.

Sincerely,

Dr. Erin Gawron

Postdoctoral fellow, Chemical & Petroleum Engineering

University of Calgary

A.2. Letter of Permission

To Whom It May Concern

This letter is to let you know that I am permitting Ms. Chengying Ai to use the manuscripts co-authored by me in her Master's thesis.

Sincerely,

Dr. Irina Chernyshova

Columbia University

A.3. Copyright form

Title: Review on the science and technology of water desalination by capacitive deionization

Author: S. Porada,R. Zhao,A. van der Wal,V. Presser,P.M. Biesheuvel

Publication: Progress in Materials Science

Publisher: Elsevier

Date: October 2013

Copyright © 2013 Elsevier Ltd.

A.4. Copyright form

Order Details

- **Order detail ID:** 72013822
- **ISSN:** 1754-5706
- **Publication Type:** e-Journal
- **Volume:**
- **Issue:**
- **Start page:**
- **Publisher:** RSC Publishing
- **Author/Editor:** Royal Society of Chemistry (Great Britain)
- **Permission Status:** ✅ **Granted**

- **Permission type:** Republish or display content
- **Type of use:** Thesis/Dissertation
-
  Order License Id: 4672620813939

- Hide details
  -

Requestor type	Academic institution
Format	Electronic
Portion	image/photo
Number of images/photos requested	1
The requesting person/organization	Chengying Ai/University of Calgary
Title or numeric reference of the portion(s)	Fig. 3 Comparison of three operational modes of MCDI: constant voltage (CV, left column); constant current during adsorption (CC) with zero voltage during desorption (ZVD, middle column); and CC with reverse current during desorption (RCD, right column). Shown are the results for effluent salt concentration (top row), cell voltage (middle row), and current (bottom row), as a function of time, for one cycle. Inlet salt concentration: csalt,in ¼ 20 mM. In the CV-mode we have adsorption at Vcell ¼ 1.2 V and desorption at Vcell ¼ 0 V (both steps have a duration of 300 s); in CC-ZVD we have salt adsorption at +1 A until Vcell ¼ 1.6 V, while during desorption Vcell ¼ 0 V for 500 s; in CC-RCD desorption is controlled by a current of?1A until the voltage is back

	at 0 V. Solid blue lines: theoretical simulations, dashed red lines: experimental data.
Title of the article or chapter the portion is from	Energy consumption and constant current operation in membrane capacitive deionization
Editor of portion(s)	N/A
Author of portion(s)	Zhao, R., Biesheuvel, P. M., van der Wal, A.
Volume of serial or monograph	5
Issue, if republishing an article from a serial	11
Page range of portion	9520–9527
Publication date of portion	2012
Rights for	Main product
Duration of use	Life of current edition
Creation of copies for the disabled	no
With minor editing privileges	yes
For distribution to	Canada
In the following language(s)	Original language of publication
With incidental promotional use	no
Lifetime unit quantity of new product	Up to 499
Title	Polyaniline-coated Nanoporous Carbon Scaffold for Energy Storage and Water Deionization Applications
Institution name	University of Calgary
Expected presentation date	Sep 2019

A.5. Copyright form

Order Details

Order detail ID:72013812

- **ISSN:**1754-5706
- **Publication Type:**e-Journal
- **Volume:**
- **Issue:**
- **Start page:**
- **Publisher:**RSC Publishing
- **Author/Editor:**Royal Society of Chemistry (Great Britain)
- **Permission Status:** ✅ **Granted**

- **Permission type:**Republish or display content
- **Type of use:**Thesis/Dissertation
-
  Order License Id: 4672620225131

- Hide details
  ○

Requestor type	Academic institution
Format	Electronic
Portion	image/photo
Number of images/photos requested	1
The requesting person/organization	Chengying Ai/University of Calgary
Title or numeric reference of the portion(s)	Fig.1 Schematic diagram of desalination via HCDI. The HCDI system consists of anNMO electrode, anion exchange membrane, and porous carbon electrode. When a cell voltage is applied between the NMO and carbon electrodes, sodium ions are held by the chemical reaction in the NMO electrode, whereas chloride ions are held in the electric double layers formed at the surface of the porous carbon electrode.
Title of the article or chapter the portion is from	Hybrid capacitive deionization to enhance the desalination performance of capacitive techniques
Editor of portion(s)	N/A
Author of portion(s)	Jaehan Lee, Seoni Kim, Choonsoo Kim and Jeyong Yoon
Volume of serial or monograph	7

126

Issue, if republishing an article from a serial	11
Page range of portion	3683-3689
Publication date of portion	2014
Rights for	Main product
Duration of use	Life of current edition
Creation of copies for the disabled	no
With minor editing privileges	yes
For distribution to	Canada
In the following language(s)	Original language of publication
With incidental promotional use	no
Lifetime unit quantity of new product	Up to 499
Title	Polyaniline-coated Nanoporous Carbon Scaffold for Energy Storage and Water Deionization Applications
Institution name	University of Calgary
Expected presentation date	